UNIVERSITY OF CALIFORNIA
RIVERSIDE

NMR Studies on Organic and Biological Solids

A Dissertation submitted in partial satisfaction
of the requirements for the degree of

Doctor of Philosophy

in

Chemistry

by

Chen Yang

March 2015

Dissertation Committee:

Dr. Leonard J. Mueller, Chairperson
Dr. Christopher J. Bardeen
Dr. Jingsong Zhang

The Dissertation of Chen Yang is approved:

Committee Chairperson

University of California, Riverside

ACKNOWLEDGMENTS

I am glad that solid-state NMR is my research focus. The technique is beautiful, powerful, and very attractive. I would like to first thank Len for accepting me as his graduate student. Len has brought me into the field of solid-state NMR. I like the research, and I benefit a lot from him not only on spin dynamics, NMR experimental setup, protein structures, but also on the general way of conducting a research. Thank you Len, for making me a responsible researcher, and for the many opportunities you've offered me.

I would also like to thank Chris, for letting me involved in the photoreaction intermediate project. It has been indeed a great learning and exploring experience. The project has broadened my vision, and I appreciate the opportunity for being able to, at least partially, determine a crystal structure.

In this project, Lingyan (Julia), has shared both excitements and frustrations with me. She is talented, and gives great advices. I wouldn't be able to make any progress without the many discussions with her. Bo has been very generous in giving me access to his computational resource, and has offered important opinions on computational setups. Fook has helped me with concerns in interpreting XRD results, and Steve has helped submitting computational jobs onto the server. I also appreciate the chat with Charlotte. She has great insight on crystallography, and has kindly offered some invaluable advices. And of course Rabih is deeply appreciated, for the precious sample he made.

The collaboration with Sang Ho from the Opella group has been another very important experience. He taught me nmrPipe, and shared his membrane protein handling experience with me. I really appreciate the time working with him.

On protein expression and purification, I am indebted to Yachong. He has been very patient and understanding in teaching me the protocols for handling tryptophan synthase. If he wasn't there the time I joined the group, it would be a forbidden task for me to figure out all the steps. Michael has always been a genius on the enzyme mechanism of tryptophan synthase. I feel very lucky to have him in many of our group meetings. Eduardo and Dimitri have also been great resources whenever we encounter confusion or trouble in dealing with proteins. It's always convenient to have Robert around when FPLC is encountered. Robert has been very reliable on that. And also thanks to him for leading me to my first mountain bike riding experience. I did horrible, but it was really fun. Ryan has been a great labmate to have also. He has excellent personality and I enjoyed working with him. By the way, he is an awesome athlete at the same time. Panpan (Guoxiang) has been very careful and helpful both in handling proteins and on spectrometer. And Dan has been helping us on Helium fill and trouble shooting. With Dan around, laughter flows. Thanks to Dan for keeping the spectrometers healthy and bring us happiness. Thanks to Jochem, for our collaboration, and for stopping by our lab. Also thanks to Beth, without her tent in the Grand Canyon, the thundershower might have been too exciting an experience. And thanks to Tommy, especially for his initial help when I just came to the group.

Lingchao has always been encouraging. He carries optimism wherever he goes. He is a talented person, and I've learnt a lot from him actually. He has being an invaluable

friend to have. Jinfeng and Tian have also offered me advices on broad aspects, which I am still benefiting from. I really appreciate the time spent with them. And many thanks to Yuanhang Huang, Fei Bu, and Yiding Liu, you guys are always awesome, especially during my fifth year here in Riverside. The friendship with you has been a great fortune for me. I would like to thank Yang Li (Chemistry), Fenglin Wang, Zhiyong Wang, Jinjin Yao, Bo Zhao, Haiyu Zhang, Yang Li (Chemical Engineering), Wenting Hou, Zhiyuan Huang, and Yiming Cheng. It has been my great luck to have you being friends in Riverside these years. You have helped me in different aspect throughout the years, and my words are not enough to express my gratitude. Also Cheng Pan and Zilong Jiang has provided me their living room to stay the first three days I came to Riverside, which I share never forget, thank you so much.

My family has been the greatest support. My mom and dad have always been there for me no matter what. They have been providing me the most sincere advice or provide their best help in any situation. Mom has always been reminding me to eat healthy, and suspecting me of starving myself. Dad has always been worried about me for many good reasons. Grandpa, grandma, my uncle and my cousins have been frequently keeping me updated of what's going at at home. There are no words adequate enough to show my gratitude for all their care for me. I would like to express my special thanks to my wife, Yuanqi, who has made my time here an unexpected journey, and in an excellent way of course. She has been extraordinarily supportive, sharing joy and sorrow with me. The presence of her in my life has made everything colorful.

The National Institutes of Health and the National Science Foundation are deeply appreciated as the funding sources.

The text of this dissertation, in part or in full, is a reprint of the material as they appear in the following publications:

Ch2: Struppe, J. O.; Yang, C.; Wang, Y.; Hernandez, R. V; Shamansky, L. M.; Mueller, L. J. *J. Magn. Reson.* **2013**, *236*, 89.

Ch3: Caulkins, B. G.; Bastin, B.; Yang, C.; Neubauer, T. J.; Young, R. P.; Hilario, E.; Huang, Y.-M. M.; Chang, C.-E. a; Fan, L.; Dunn, M. F.; Marsella, M. J.; Mueller, L. J. *J. Am. Chem. Soc.* **2014**, *136*, 12824.

Caulkins, B. G.; Yang, C.; Hilario, E.; Fan, L.; Dunn, M. F.; Mueller, L. J. *Biochim. Biophys. Acta - Proteins Proteomics* **2015**. DOI: 10.1016/j.bbapap.2015.02.003

Ch4: Park, S. H.; Yang, C.; Opella, S. J.; Mueller, L. J. *J. Magn. Reson.* **2013**, *237C*, 164.

ABSTRACT OF THE DISSERTATION

NMR Studies on Organic and Biological Solids

by

Chen Yang

Doctor of Philosophy, Graduate Program in Chemistry
University of California, Riverside, March 2015
Dr. Leonard J. Mueller, Chairperson

Solid-state NMR (SSNMR) studies on biomolecules and organic molecular crystals are presented here. The biological part of the work is focused on improving resolution and sensitivity of SSNMR techniques for larger protein systems, while the studies on organic molecular crystals extend the application of SSNMR to determining the crystal structure of a photoreaction intermediate. First, a long-observation-window band-selective homonuclear decoupling scheme is introduced. The homonuclear decoupling technique decouples *J*-couplings during direct ^{13}C acquisition between backbone C^{α} and C' nuclei in U-^{13}C-labeled proteins. The method can be directly incorporated into existing correlation methods that detect C' resonances. Correlation spectroscopy examples are shown on the GB1 and the α-subunit of tryptophan synthase. Then, chemical shifts measured at the active site within the β subunit of tryptophan synthase are shown, with indications of potential protonation states explained. After that, the setup of the SSNMR correlation methods are presented. ^{1}H decoupling performance is interpreted using a spin echo experiment with

varied decoupling power and magic angle spinning speeds with acquisition on ^{13}C. After the ^{1}H decoupling performance is mapped out, the distance measurements are performed using a perdeuterated Pf1 bacteriophage sample with exchangeable sites protonated. Effects of deuteration and radio frequency power on cross polarization are later discussed on GB1 samples at 50 kHz MAS. This part concludes the preparation of correlation methods to future applications on TS. In the second part of the thesis, NMR crystallography is used to determine the structure of the solid-state photoreaction intermediate of 9-tertbutyl anthracene. The work uses chemical shifts and chemical shift anisotropy parameters measured for microcrystalline solids to validate predicted structures from powder X-ray diffraction and computational data. The resulting structure for the photoreaction intermediate pointed to a possible mechanism for the elongation of 9-tertbutyl anthracene nanorods upon illumination. The studies within this work opens up new possibilities for the scope of the SSNMR technique.

TABLE OF CONTENTS

Page

LIST OF FIGURES

LIST OF TABLES

Chapter 1

Introduction

1.1 Background

Solid-state NMR (SSNMR) is an important technique for studying structural details at the atomic scale. For biological and organic samples, the measurements are usually performed on ^{13}C, ^{15}N or ^{1}H nuclei.[1,2] The chemical shifts measured during NMR experiments relate to local chemical environments, like protonation states of an enzyme active site,[3,4] the secondary or tertiary structure of a protein,[5–8] and the presence of hydrogen bonding within molecular crystals.[9,10] In liquid-state NMR, frequent tumbling of molecules produces very narrow linewidth, granting high resolution.[11] However, in SSNMR, linebroadenings are removed by magic angle spinning (MAS) in combination with Radio Frequency (RF) pulses. The coherent averaging effect can truncate terms like dipolar couplings, chemical shift anisotropy, and orientation distribution among microcrystals.[12] The narrow lines thus achieved in SSNMR are not limited by the size of the molecule, making the technique potentially powerful in handling large biological macromolecules. Moreover, samples do not need to be soluble for SSNMR. This has made SSNMR especially useful in dealing with membrane proteins. These proteins usually have low solubility in aqueous solution, inappropriate for liquid-state NMR, and are in the noncrystalline membrane bound form at native states, preventing diffraction studies. Multiple previous work has shown the great potential of SSNMR in this area.[13–16] Having samples in solid form also enables SSNMR experiments on microcrystals, providing

information on crystal structure complementary to diffraction based techniques, like X-ray Diffraction (XRD). SSNMR can predict unit cell composition,[17,18] hydrogen bonding,[19,20] protonation states[3,4], and examine computational predictions.[9] Recent advancements in computational chemistry have enabled the method to produce more and more reliable calculated chemical shieldings. These developments have assisted SSNMR in its broader application on crystallography.[4,17,21–23]

Although SSNMR is potentially widely applicable in a lot of topics associated in biochemistry or crystallography, the small differences in the population between spin states, as defined by Boltzmann statistics, has made NMR a relatively insensitive technique.[24] At thermal equilibrium, according to the Boltzmann distribution, the probability of finding a spin at energy E_i is expressed as:

$$p_i = A \exp(-E_i/kT) \tag{1.1}$$

For spin-1/2 nuclei, the energy difference between the two eigenstates is given by:

$$\Delta E = \frac{h\gamma B_0}{2\pi} \tag{1.2}$$

This results in the ratio of population in the lower energy state to population in the higher energy state being:

$$N_{low}/N_{high} = \exp(h\gamma B_0/2\pi kT) \tag{1.3}$$

Even for ^{1}H in a magnetic field of 18.8 T at a temperature of 200 K, the population difference between the two states would only be 1.9×10^{-4}. A lot effort in the field has been investing into the NMR spectroscopy, including the development of higher magnetic field, cryoprobes, dynamic nuclear polarization, etc. Hardware advancs are pushing the limit of both B_0 and T, and opening us possibilities of utilizing the high γ from electron

spins. In addition to instrumental developments, improvements are also progressing in sample preparation and RF pulse sequences. The natural abundance of the most common isotopes for biological and organic samples are ^{1}H (99.98%), ^{13}C (1.11%), and ^{15}N (0.37%). Apart from ^{1}H, ^{13}C and ^{15}N appear sparsely in natural abundance samples. However, the abundant ^{12}C (98.93%) has zero spin, being non-responsive for NMR detection, and the spin-1 ^{14}N (99.63%) has a low γ and large quadrupole coupling constant, causing difficulties in real applications. Enrichment of ^{15}N or ^{13}C has become necessary for the requirement of sensitivity. For biological macromolecules, ^{13}C can be introduced by using a growth medium containing ^{13}C-labeled glucose or its derivatives (glycerol, acetate, pyruvate, succinate) as the sole carbon sources, and ammonium chloride, (or nitrate, sulfate) as the sole nitrogen source.[1] And when needed, specific substrates or amino acid labeling can also be performed with various enrichment protocols.[5,25,26] For organic samples, ^{13}C or ^{15}N can be introduced with available labeled reactants. And if the molecules are small, a natural abundance sample can be used with extensive experimental time. Also, deuteration are better understood these years, making the more sensitive ^{1}H detection in SSNMR realistic and powerful at high MAS rates. Besides labeling strategies, in SSNMR, in order to perform isotropic chemical shift measurements, MAS and the RF pulses can combine, removing the dipolar interaction and chemical shift anisotropy. And sometimes, both types of information can be selectively recovered with carefully designed RF pulse components at the corresponding MAS rates.[27–32] Methods have developed throughout the years, broadening the class of experiments that SSNMR can perform, and improving the resolution and sensitivity of available instruments.

This dissertation is focused on the improvement of resolution and sensitivity of SSNMR for the study of details at the atomic scale for biological and organic substances. For biological sample, the streptococcal immunoglobulin binding domain β1 of protein G (GB1) was chosen as the model protein. The experiments developed on GB1 (8 kDa) set the ground work for future studies to solve the structure of the large (144 kDa) tryptophan synthase (TS). In dealing with organic molecules, 9-anthracene derivative photoreactive molecules were studied. The major result on this part was the application of SSNMR to determine the structure of the photoreaction intermediate of 9-tertbutyl-anthracene ester (**9TBAE**).

First, a general overview of the quantum mechanical theory involved for SSNMR will be described. Then NMR Crystallography will be explained. In Chapter 2, a homonuclear decoupling scheme will be introduced for ^{13}C acquisition of carbonyl carbons in a uniformly-^{13}C-labeled protein backbone. Then Chapter 3 will show the sensitivity contrast created by the labeled coenzyme exchanged into the natural abundance tryptophan synthase. This work resulted in chemical shift determination of important positions within the enzyme β unit active site, indicating protonation states of the enzyme intermediates. In Chapter 4, exploration of SSNMR experiments at very fast MAS rates will be summarized. And then in Chapter 5, the NMR crystallography work on 9TBAE will be presented. Chapter 6 contains the concluding remarks.

1.2 Quantum Mechanical Overview of SSNMR

The quantum mechanics involved in SSNMR is briefly reviewed in this section. The discussion is specific to spin-1/2 nuclei, since in biological or organic applications,

spin-1/2 nuclei, like ^{13}C, ^{15}N, ^{1}H and ^{31}P are the most common. In this work, only ^{13}C, ^{15}N and ^{1}H are considered. More comprehensive quantum mechanical descriptions of SSNMR can be found in multiple books and review papers.[12,24,33,34] The description here only serves as a quick reference and overview of the quantum mechanical nomenclature and terms related to this thesis.

1.2.1 The Density Operator

In the Dirac notation,[35] the Schrödinger equation[36,37] can be expressed as:

$$i\hbar\frac{d}{dt}|\psi(t)\rangle = \boldsymbol{H}(t)|\psi(t)\rangle \tag{1.4}$$

where the $|\psi(t)\rangle$ is a state vector, ***H(t)*** is the Hamiltonian, and $\hbar$ is the Planck constant. Since only time dependence is considered, there is no need to use the partial derivative on the left side of the above equation. The equation describes the evolution of the state vector under the Hamiltonian of ***H(t)***. The mean value of an observable ***A*** at time *t* can be described as:

$$\langle \boldsymbol{A}\rangle(t) = \langle\psi(t)|\boldsymbol{A}|\psi(t)\rangle \tag{1.5}$$

If an orthonormal basis set is known, the state vector can be expended as:

$$|\psi(t)\rangle = \sum_n c_n(t)|u_n\rangle \tag{1.6}$$

with $\{|u_n\rangle\}$ being the orthonormal basis. When only spin in a static magnetic field is considered, in the case of a single spin-1/2 nuclei, the basis set will be composed of two states, and in the case of the ensemble of *m* spin-1/2 nuclei, $n = 2m$. With the knowledge of the basis set, the state vector and the observable can be projected on to the basis.[38] Equation (1.5) can be further expressed as:

$$\langle \boldsymbol{A} \rangle(t) = \sum_{p,n} \langle \psi(t) | u_p \rangle \langle u_p | \boldsymbol{A} | u_n \rangle \langle u_n | \psi(t) \rangle$$

$$= \sum_{p,n} \langle u_n | \psi(t) \rangle \langle \psi(t) | u_p \rangle \langle u_p | \boldsymbol{A} | u_n \rangle$$

$$= \mathrm{Tr}\{ |\psi(t)\rangle\langle\psi(t)| \boldsymbol{A} \} \quad \textbf{(1.7)}$$

The projector form of $|\psi(t)\rangle\langle\psi(t)|$ can thus be defined as the density operator $\boldsymbol{\rho}(t)$ with:

$$\boldsymbol{\rho}(t) = |\psi(t)\rangle\langle\psi(t)| \quad \textbf{(1.8)}$$

And we have:

$$\langle \boldsymbol{A} \rangle(t) = \mathrm{Tr}\{\boldsymbol{\rho}(t)\boldsymbol{A}\} = \mathrm{Tr}\{\boldsymbol{A}\boldsymbol{\rho}(t)\} \quad \textbf{(1.9)}$$

The density operator introduced in equation (1.8) is easier to handle than the state vector in the application of NMR, since our interest is more focused on the observable, and coherences between the states are frequently involved. In this way, the time dependence can be deduced from equation (1.4):

$$\frac{d}{dt}\boldsymbol{\rho}(t) = \left(\frac{d}{dt}|\psi(t)\rangle\right)\langle\psi(t)| + |\psi(t)\rangle\left(\frac{d}{dt}\langle\psi(t)|\right)$$

$$= \frac{1}{i\hbar}[\boldsymbol{H}(t), \boldsymbol{\rho}(t)] \quad \textbf{(1.10)}$$

To avoid the Planck constant showing up in the denominator all the time, equation (1.10) is usually simplified as:

$$\frac{d}{dt}\boldsymbol{\rho}(t) = -i[\boldsymbol{H}(t), \boldsymbol{\rho}(t)] \quad \textbf{(1.11)}$$

with $\boldsymbol{H}(t) = \boldsymbol{H}(t)/\hbar$ in the following contents.

The above discussion is based on the quantum mechanics of a pure state. For a statistical mixture of states, suppose p_k gives the probability that the system is in state $|\psi_k\rangle$. The probabilities satisfy the requirement:

$$\sum_k p_k = 1 \tag{1.12}$$

The density operator for each pure state can be expressed as:

$$\boldsymbol{\rho}_k = |\psi_k\rangle\langle\psi_k| \tag{1.13}$$

The expectation value for observable $\boldsymbol{A}$ at time t can be deduced as:

$$\begin{aligned}\langle \boldsymbol{A}\rangle(t) &= \sum_k p_k \mathrm{Tr}\{\boldsymbol{\rho}_k \boldsymbol{A}\} \\ &= \mathrm{Tr}\left\{\left(\sum_k p_k \boldsymbol{\rho}_k\right)\mathbf{A}\right\} \\ &= \mathrm{Tr}\{\boldsymbol{\rho A}\} = \mathrm{Tr}\{\boldsymbol{A\rho}\}\end{aligned} \tag{1.14}$$

At thermal equilibrium, in a static field B_0 parallel to z-axis, from equation (1.1) and (1.13) we have the density matrix for the statistical mixture of similar spin-1/2 as:

$$\boldsymbol{\rho} = Z^{-1}\begin{pmatrix} e^{-\hbar\omega_0/2kT} & 0 \\ 0 & e^{+\hbar\omega_0/2kT}\end{pmatrix} \tag{1.15}$$

where the partition function $Z = e^{-\hbar\omega_0/2kT} + e^{+\hbar\omega_0/2kT}$. We are usually in a domain of high temperature ($|\frac{\hbar\omega_0}{2kT}| \ll 1$). This lead to the density matrix being approximated as:

$$\begin{aligned}\boldsymbol{\rho} &= \begin{pmatrix} 1-\hbar\omega_0/2kT & 0 \\ 0 & 1+\hbar\omega_0/2kT\end{pmatrix} \\ &= \mathbb{I} - \hbar\omega_0/kT\begin{pmatrix} 1/2 & 0 \\ 0 & -1/2\end{pmatrix} \\ &= \mathbb{I} - \beta \boldsymbol{I_z}\end{aligned} \tag{1.16}$$

In the relation above, $\mathbb{I}$ is the identity matrix. And the secular part of a Hamiltonian corresponding to a sample in a large static magnet would usually be the $\beta \boldsymbol{I_z}$ term. RF pulses can manipulate the $\beta \boldsymbol{I_z}$ term to create coherences between energy levels (I_x, I_y, $I_x S_y$, etc.). Then during the acquisition of an NMR experiment, we have:

$$\langle \boldsymbol{I}_+ \rangle(t) = \mathrm{Tr}\{\boldsymbol{I}_+ \boldsymbol{\rho}(t)\} \tag{1.17}$$

According to the equation (1.11), if the Hamiltonian $\boldsymbol{H}$ is time-independent, one will have:

$$\boldsymbol{\rho}(t) = \exp(-i\boldsymbol{H}t)\, \boldsymbol{\rho}(0) \exp(i\boldsymbol{H}t) \tag{1.18}$$

However, if the Hamiltonian $\boldsymbol{H}$ is time dependent, the above equation is the approximation of the combination of a series time-independent segments, which still maintain the unitary expression quite well.[12]

At last the expectation value in equation (1.17) can be expressed as:

$$\langle \boldsymbol{I}_+ \rangle(t) = \mathrm{Tr}\{\boldsymbol{I}_+ \exp(-i\boldsymbol{H}t)\, \boldsymbol{\rho}(0) \exp(i\boldsymbol{H}t)\} \tag{1.19}$$

We can reorganize equation (1.19) to give:

$$\langle \boldsymbol{I}_+ \rangle(t) = \mathrm{Tr}\{\exp(i\boldsymbol{H}t) \boldsymbol{I}_+ \exp(-i\boldsymbol{H}t)\, \boldsymbol{\rho}(0)\} \tag{1.20}$$

If the Hamiltonian carries frequency information in the form of $\boldsymbol{H} = \omega \boldsymbol{I_z}$, there is the correlation:[24]

$$\exp(i\omega \boldsymbol{I_z} t)\, \boldsymbol{I}_+ \exp(-i\omega \boldsymbol{I_z} t) = \exp(-i\omega t)\, \boldsymbol{I}_+ \tag{1.21}$$

One would be able to extract the information on Hamiltonian $\boldsymbol{H}$ by detecting ω in the above equation from free induction decays:

$$\langle \boldsymbol{I}_+ \rangle(t) = \mathrm{Tr}\{\exp(-i\omega t)\, \boldsymbol{I}_+ \boldsymbol{\rho}(0)\} \tag{1.22}$$

The $\boldsymbol{\rho}(0)$ term appearing in the above equations usually means the initial density operator of the spin system right after the first 90° RF pulse. However, the value of $\boldsymbol{\rho}(t)$

appearing in equation (1.17) and (1.18) would largely depend on the Hamiltonians during evolution and detection. Different information can be encoded into the Hamiltonian $\boldsymbol{H}$ depending on the sample, the RF pulse sequences, and MAS. These effects will be described in the following two sections.

1.2.2 The Hamiltonian

For SSNMR of organic or biological samples, in most cases we would need the Hamiltonian for diamagnetic nonconducting substances:[12]

$$\boldsymbol{H} = \boldsymbol{H_Z} + \boldsymbol{H_{RF}} + \boldsymbol{H_{CS}} + \boldsymbol{H_D} + \boldsymbol{H_J} \tag{1.23}$$

where $\boldsymbol{H_z}$ is the Zeeman Hamiltonian, $\boldsymbol{H_{RF}}$ is the quantum mechanical representation of the RF pulses, $\boldsymbol{H_{cs}}$ is the tensor form of chemical shift, $\boldsymbol{H_D}$ is the dipole-dipole interaction term, and $\boldsymbol{H_J}$ is the scalar coupling term.

The Zeeman Hamiltonian refers to the separation of energy levels induced by the static magnetic field $\vec{B}_{st}$ along the (0,0,B_z) axis. Again, the Planck constant ħ is taken out of the Hamiltonians for simplicity:

$$\boldsymbol{H_z} = -\sum_i \gamma_i \boldsymbol{I_{iz}} B_z = \sum_i \omega_{i0} \boldsymbol{I_{iz}} \tag{1.24}$$

where γ_i is the gyromagnetic ratio of the i^{th} nucleus, and $\omega_{i0} = \gamma_i B_z$.

The RF field Hamiltonian is expressed below, in this case parallel to the x-axis as an example:

$$\boldsymbol{H_{RF}} = -B_1(t)\cos(\omega t + \varphi(t)) \sum_i \gamma_i \boldsymbol{I_{ix}} \tag{1.25}$$

In the above equation $B_1(t)$ is determined by the amplitude of the RF pulse, and $\omega/2\pi$ the frequency.

The Hamiltonian for chemical shift caused by local electron shieldings is in the form:

$$\boldsymbol{H_{CS}} = \sum_i \gamma_i \vec{I}_i \cdot \boldsymbol{\sigma} \cdot \vec{B}_z \tag{1.26}$$

The dipolar Hamiltonian is given as:

$$\hbar \boldsymbol{H_D} = \sum_{i<k} \left(-\frac{4\pi\gamma_i\gamma_k\hbar^2}{\mu_0 r_{ik}^3} \right) \left(\frac{3\left(\vec{I}_i \cdot \vec{r}_{ik}\right)\left(\vec{I}_k \cdot \vec{r}_{ki}\right)}{\vec{r}_{ik}{}^2} - \vec{I}_i \cdot \vec{I}_k \right) \tag{1.27}$$

The principle axis of a dipolar spin pair is along the $\vec{r}_{ik}$ direction. Taking this direction as the z-axis, the dipolar Hamiltonian for a specific spin pair would be in the form:

$$\hbar \boldsymbol{H_{ikD}} = \left(-\frac{4\pi\gamma_i\gamma_k\hbar^2}{\mu_0 r_{ik}^3} \right) \left(2\boldsymbol{I_{iz}I_{kz}} - \boldsymbol{I_{ix}I_{kx}} - \boldsymbol{I_{iy}I_{ky}} \right) \tag{1.28}$$

$$= \left(-\frac{\gamma_i\gamma_k\hbar^2}{r_{ik}^3} \right) \vec{I}_i \cdot \begin{pmatrix} -1 & 0 & 0 \\ 0 & -1 & 0 \\ 0 & 0 & 2 \end{pmatrix} \cdot \vec{I}_k \tag{1.29}$$

The indirect spin-spin coupling term (*J*-coupling) is expressed as:

$$\boldsymbol{H_J} = \sum_{i<k} \vec{I}_i \cdot \boldsymbol{J_{ik}} \cdot \vec{I}_k \tag{1.30}$$

Many interactions are involved for an ensemble of spins within a diamagnetic sample sitting in a static magnetic field. However, not all the above mentioned Hamiltonians are wanted during an NMR experiment. Actually the most useful chemical shift information indicated in the equation (1.26) is still far from obvious in the above form.

A procedure called 'averaging' is necessary to truncate the unnecessary terms within the total Hamiltonian in equation (1.23). The averaging can be achieved by inducing a time-dependence into these unwanted terms, so they average to zero, leaving only the useful terms surviving for detection.

1.2.3 Coherent Averaging

The averaging effects make the appropriate Hamiltonians preserve fast common motions. This can be described in the rotating frame. However, before applying the rotating spin frame, since the principal axis system (PAS) of a property can orient differently with respect to the observer, proper rotation operations have to be applied to take into account the Euler angles between them.[39,40] For simplicity, all discussion will be carried out in the lab frame, where the observables are defined. The unitary rotation operator $\boldsymbol{R_A}(\varphi_1, \varphi_2, \varphi_3)$ denotes the active rotation of Euler angles φ_1, φ_2, and φ_3.[39] In a MAS SSNMR experiment, the representation of a Hamiltonian in a lab frame would need the rotation of $\boldsymbol{R_A}(0, \theta, \omega_r t)$ for the rotor during MAS, then $\boldsymbol{R_A}(\alpha, \beta, \gamma)$ to transform to the PAS of the specific term. The Hamiltonian terms for chemical shift anisotropy (CSA) (equation (1.26)), dipolar coupling (equation (1.29)), and *J*-coupling (equation (1.30)) are all in the form of $\boldsymbol{H_\lambda^{Lab}} = C_\lambda \, \overrightarrow{v1}_\lambda^{Lab} \cdot \boldsymbol{T_\lambda^{Lab}} \cdot \overrightarrow{v2}_\lambda^{Lab}$, where C_λ is a constant, $\overrightarrow{v1}$ and $\overrightarrow{v2}$ are the vectors containing the observable operators, $\boldsymbol{T_\lambda}$ is the tensor form of the corresponding property (CSA, Dipolar coupling, or the *J*-coupling), and the '*Lab*' superscript indicate the laboratory frame. We have:

$$\boldsymbol{T_\lambda^{Lab}} = \boldsymbol{R_A}(\alpha, \beta, \gamma)\boldsymbol{R_A}(0, \theta, \omega_r t)\boldsymbol{T_\lambda^{PAS}}\boldsymbol{R_A^{-1}}(0, \theta, \omega_r t)\boldsymbol{R_A^{-1}}(\alpha, \beta, \gamma) \qquad \textbf{(1.31)}$$

In the above equation, the three Euler angles α, β, and γ define the direction of the PAS with respect to the rotor. Angle θ is the magic angle ($\arccos(1/\sqrt{3})$), and ω_r is the spinning rate. The averaging effect induced by the magic angle θ and the spinning frequency ω_r would add time dependence to the orientation dependent terms, we truncate these terms from the original Hamiltonian. On the other hand, the Zeeman term (equation (1.24)) contains only the information reflecting the gyromagnetic ratio of the corresponding spin and the strength of the magnet, but no information about the sample. However, the Zeeman term add fast global precession of the spins at the Larmor frequency. The time dependencies introduced into our Hamiltonian can be explained in the rotating frame. The Hamiltonian in the rotating frame is in the form:

$$\boldsymbol{H^R = H^R_{RF} + H^R_{CS} + H^R_D + H^R_J} \tag{1.32}$$

with the evolution operator:

$$\boldsymbol{U_Z} = \exp(-i\boldsymbol{H_Z}t) \tag{1.33}$$

where $\boldsymbol{H_Z}$ is the Zeeman Hamiltonian. The truncations induced by the rotating frame at the Larmor frequency will be described below, with considerations also about the relative orientations of PAS. The discussion will be presented first for the CSA Hamiltonian, then for the dipolar Hamiltonian, and then for the *J*-coupling Hamiltonian.

1.2.3.1 Chemical Shift Anisotropy

The CSA tensor in its PAS frame has the form:

$$\boldsymbol{\sigma} = \begin{pmatrix} \sigma_{iso} - \delta(1+\eta)/2 & 0 & 0 \\ 0 & \sigma_{iso} - \delta(1-\eta)/2 & 0 \\ 0 & 0 & \sigma_{iso} + \delta \end{pmatrix} \tag{1.34}$$

where in Haeberlen's convention, σ_{iso} is the isotropic chemical shift: $\sigma_{iso} = (\sigma_{xx} + \sigma_{yy} + \sigma_{zz})/3$; δ is the anisotropy parameter: $\delta = \sigma_{zz} - \sigma_{iso}$, and η the asymmetric parameter: $\eta = (\sigma_{yy} - \sigma_{xx})/\delta$.

By applying equation (1.31) on the tensor form (1.34), one can get all nine elements of the CSA tensor in the lab frame. However, since $\vec{B}_z = (0, 0, B_z)$, only three terms would survive. For a system with only one spin, we have:

$$\boldsymbol{H_{CS}} = \gamma B_z \boldsymbol{I_x} \sigma_{xz}^{Lab} + \gamma B_z \boldsymbol{I_y} \sigma_{yz}^{Lab} + \gamma B_z \boldsymbol{I_z} \sigma_{zz}^{Lab} \quad \textbf{(1.35)}$$

Then the rotating frame at Larmor frequency ω_0 can be applied as:

$$\boldsymbol{H_{CS}^{R}} = \boldsymbol{U_Z H_{CS} U_Z^{-1}} \quad \textbf{(1.36)}$$

According to equation (1.21), the first two terms in equation (1.35) would result in an extra $\exp(-i\omega_0 t)$ phase term. However, the third term commutes with $\boldsymbol{U_Z}$, leading to $\boldsymbol{U_z I_z U_z^{-1}} = \boldsymbol{I_z}$. Thus the secular term useful for NMR detection would only be:

$$\boldsymbol{H_{CS}^{R,secular}} = \gamma B_z \boldsymbol{I_z} \sigma_{zz}^{Lab} \quad \textbf{(1.37)}$$

with the explicit form of σ_{zz}^{Lab} discussed in previous works.[39,41] Most of the terms within σ_{zz}^{Lab} are time dependent induced by MAS, with the exception of the isotropic chemical shift.

1.2.3.2 Dipolar Coupling

The dipolar tensor for each spin pair would have the respective coupling constant $-\frac{\gamma_i \gamma_k \hbar}{r_{ik}^3}$ determined by the distance between the spin pair, and the gyromagnetic ratios of the two partner spins. The spacial orientation part is the same for all dipolar interactions in their respective PAS coordinate:

$$\boldsymbol{D^{PAS}} = \begin{pmatrix} -1 & 0 & 0 \\ 0 & -1 & 0 \\ 0 & 0 & 2 \end{pmatrix} \quad \textbf{(1.38)}$$

Equation (1.31) can be applied on the above tensor to achieve the dipolar tensor representation in the lab frame. The Hamiltonian would require all nine elements for interpretation, since neither spin vector of a spin pair is truncated in this case. However, applying the rotating frame at Larmor frequency using the evolution operator (1.33), one can again achieve terms modulated with very fast time dependent phase oscillations. This can result in the secular term for dipolar coupling between heteronuclear spins being in the form:

$$\boldsymbol{H_D^{R,Secular}} = C\left(\cos(2\alpha + 2\omega_r t)\, sin^2(\beta) - \sqrt{2}\cos(\alpha + \omega_r t)\sin(2\beta)\right)\boldsymbol{I_z S_z} \quad \textbf{(1.39)}$$

The form of homonuclear dipolar interactions would be represented as:

$$\boldsymbol{H_D^{R,Secular}} = C\left(\frac{1}{2}\cos(2\alpha + 2\omega_r t)\, sin^2(\beta) - \frac{\sqrt{2}}{2}\cos(\alpha + \omega_r t)\sin(2\beta)\right)(2\boldsymbol{I_z S_z} - \boldsymbol{I_x S_x} - \boldsymbol{I_y S_y}) \quad \textbf{(1.40)}$$

Where C is the constant $-\frac{4\pi\gamma_i\gamma_k\hbar}{\mu_0 r_{ik}^3}$, and ω_r is the MAS rate.

1.2.3.3 J-Coupling

In principle, the *J*-coupling tensor would be very similar to the case of CSA tensor. One can still define isotropic *J*-coupling, and then anisotropy and asymmetry parameters correspondingly. However, *J*-couplings for non-metals are small in size (<150 Hz)[42], and the phase modulation induced by MAS and by observing in the rotating frame at Larmor

frequency will always be large in comparison. This results in the *J*-coupling behave only as a scalar secular term:

$$\boldsymbol{H_J^{R,Secular}} = \sum_{\boldsymbol{i,k}} J_{ik} \boldsymbol{I_{iz} I_{kz}} \tag{1.41}$$

The RF field can be treated using a similar method: by rotating the Hamiltonian and the use of the rotating frame. Nevertheless, the sequences of RF pulses are dependent on the design of the experiment, and would be different in each case. Sometimes it's even more convenient to apply the rotating frame to an RF pulse. There are a lot good discussions on the topic,[29,43–45] which is beyond the scope of this thesis.

1.3 NMR Crystallography

NMR Crystallography often refers to the use of SSNMR techniques on powder samples in combination with computational calculations to provide structural details at the atomic level. The method usually provides information complementary to X-ray (or neutron) diffraction studies. While X-ray (or neutron) diffraction can provide very precise crystallographic parameters, SSNMR is more sensitive to local chemical environment, including hydrogen bonding, protonation states, torsional angles, etc.[1,4,18] In recent years, NMR crystallography has seen rapid development in determining the structures of biological macromolecules. For these molecules, the secondary and tertiary structure of a macromolecule, rather than its unit cell dimension or space group identity, is often more closely related to the function of the biological entity.[3,46,47] Also, as mentioned previously, for those molecules not easy to crystallize, SSNMR might be the only experimental technique to study the structure.[14] The development of multidimensional correlation

techniques can result in higher resolution and sensitivity, lead to improved assignments of chemical shifts. This will facilitate the application of SSNMR to even larger biological macromolecules. For microcrystals of smaller molecules, SSNMR can also be used when diffraction studies are especially difficult, like for photoreactive molecules.[48]

1.4 References

(1) Renault, M.; Cukkemane, A.; Baldus, M. *Angew. Chemie - Int. Ed.* **2010**, *49*, 8346.

(2) Brown, S. P. *Solid State Nucl. Magn. Reson.* **2012**, *41*, 1.

(3) Caulkins, B. G.; Bastin, B.; Yang, C.; Neubauer, T. J.; Young, R. P.; Hilario, E.; Huang, Y.-M. M.; Chang, C.-E. a; Fan, L.; Dunn, M. F.; Marsella, M. J.; Mueller, L. J. *J. Am. Chem. Soc.* **2014**, *136*, 12824.

(4) Lai, J.; Niks, D.; Wang, Y.; Domratcheva, T.; Barends, T. R. M.; Schwarz, F.; Olsen, R. a; Elliott, D. W.; Fatmi, M. Q.; Chang, C. a; Schlichting, I.; Dunn, M. F.; Mueller, L. J. *J. Am. Chem. Soc.* **2011**, *133*, 4.

(5) Franks, W. T.; Zhou, D. H.; Wylie, B. J.; Money, B. G.; Graesser, D. T.; Frericks, H. L.; Sahota, G.; Rienstra, C. M. *J. Am. Chem. Soc.* **2005**, *127*, 12291.

(6) Pauli, J.; Baldus, M.; van Rossum, B.; de Groot, H.; Oschkinat, H. *Chembiochem* **2001**, *2*, 272.

(7) Higman, V. a; Flinders, J.; Hiller, M.; Jehle, S.; Markovic, S.; Fiedler, S.; van Rossum, B.-J.; Oschkinat, H. *J. Biomol. NMR* **2009**, *44*, 245.

(8) Barbet-Massin, E.; Pell, A. J.; Retel, J. S.; Andreas, L. B.; Jaudzems, K.; Franks, W. T.; Nieuwkoop, A. J.; Hiller, M.; Higman, V.; Guerry, P.; Bertarello, A.; Knight, M. J.; Felletti, M.; Le Marchand, T.; Kotelovica, S.; Akopjana, I.; Tars, K.; Stoppini, M.; Bellotti, V.; Bolognesi, M.; Ricagno, S.; Chou, J. J.; Griffin, R. G.; Oschkinat, H.; Lesage, A.; Emsley, L.; Herrmann, T.; Pintacuda, G. *J. Am. Chem. Soc.* **2014**.

(9) Salager, E.; Stein, R. S.; Pickard, C. J.; Elena, B.; Emsley, L. *Phys. Chem. Chem. Phys.* **2009**, *11*, 2610.

(10) Harper, J. K.; Grant, D. M.; Zhang, Y.; Lee, P. L.; Von Dreele, R. *J. Am. Chem. Soc.* **2006**, *128*, 1547.

(11) Claridge, T. D. W. *High-Resolution NMR Techniques in Organic Chemistry*; Elsevier, 2009.

(12) Haeberlen, U. *High Resolution NMR in Solids Selective Averaging: Supplement 1 Advances in Magnetic Resonance*; Academic Press, 1976; p. 204.

(13) Park, S. H.; Marassi, F. M.; Black, D.; Opella, S. J. *Biophys. J.* **2010**, *99*, 1465.

(14) Park, S. H.; Das, B. B.; Casagrande, F.; Tian, Y.; Nothnagel, H. J.; Chu, M.; Kiefer, H.; Maier, K.; De Angelis, A. a; Marassi, F. M.; Opella, S. J. *Nature* **2012**, *491*, 779.

(15) Petkova, A. T.; Baldus, M.; Belenky, M.; Hong, M.; Griffin, R. G.; Herzfeld, J. *J. Magn. Reson.* **2003**, *160*, 1.

(16) Hu, F.; Luo, W.; Hong, M. *Science* **2010**, *330*, 505.

(17) Bonhomme, C.; Gervais, C.; Babonneau, F.; Coelho, C.; Pourpoint, F.; Azaïs, T.; Ashbrook, S. E.; Griffin, J. M.; Yates, J. R.; Mauri, F.; Pickard, C. J. First-principles calculation of NMR parameters using the gauge including projector augmented wave method: A chemists point of view. *Chemical Reviews*, 2012.

(18) Martineau, C. NMR crystallography: Applications to inorganic materials. *Solid State Nuclear Magnetic Resonance*, 2014, *63-64C*, 1–12.

(19) Li, P.; Chu, Y.; Wang, L.; Wenslow, R. M.; Yu, K.; Zhang, H.; Deng, Z. *CrystEngComm* **2014**, *16*, 3141.

(20) Dudenko, D. V; Williams, P. A.; Hughes, C. E.; Antzutkin, O. N.; Velaga, S. P.; Brown, S. P.; Harris, K. D. M. *J. Phys. Chem. C* **2013**, 12258.

(21) Yates, J.; Pickard, C.; Mauri, F. *Phys. Rev. B* **2007**, *76*, 024401.

(22) Dudenko, D. V.; Yates, J. R.; Harris, K. D. M.; Brown, S. P. *CrystEngComm* **2013**, *15*, 8797.

(23) Johnston, J. C.; Iuliucci, R. J.; Facelli, J. C.; Fitzgerald, G.; Mueller, K. T. *J. Chem. Phys.* **2009**, *131*, 144503.

(24) Goldman, M.; Webb, G. A. *Magn. Reson. Chem.* **1989**, *27*, 1.

(25) Mozzarelli, a; Peracchi, a; Rossi, G. L.; Ahmed, S. a; Miles, E. W. *J. Biol. Chem.* **1989**, *264*, 15774.

(26) Vuister, G. W.; Kim, S.-J.; Wu, C.; Bax, A. *J. Am. Chem. Soc.* **1994**, *116*, 9206.

(27) Bennett, a. E.; Griffin, R. G.; Ok, J. H.; Vega, S. *J. Chem. Phys.* **1992**, *96*, 8624.

(28) Takegoshi, K.; Nakamura, S.; Terao, T. *Chem. Phys. Lett.* **2001**, *344*, 631.

(29) Baldus, M.; Petkova, A. T.; Herzfeld, J.; Griffin, R. G. *Mol. Phys.* **1998**, *95*, 1197.

(30) Carravetta, M.; Eden, M.; Zhao, X.; Brinkmann, A.; Levitt, M. H. *Chem. Phys. Lett.* **2000**, 205.

(31) Rossum, B. J. Van; Forster, H.; Groot, H. J. M. De. *J. Magn. Reson.* **1997**, *519*, 516.

(32) Hu, B.; Wang, Q.; Lafon, O.; Trébosc, J.; Deng, F.; Amoureux, J. P. *J. Magn. Reson.* **2009**, *198*, 41.

(33) Shekar, S. C.; Ramamoorthy, A. **2001**, *342*, 127.

(34) Waugh, J. S. *Magn. Reson. Med.* **1988**, *7*, 253.

(35) Dirac, P. A. M. A new notation for quantum mechanics. *Mathematical Proceedings of the Cambridge Philosophical Society*, 1939, *35*, 416.

(36) Schrödinger, E. *Phys. Rev.* **1926**, *28*, 1049.

(37) Schrödinger, E. *Math. Proc. Cambridge Phil. Soc.* **1935**, *31*, 555.

(38) Cohen-Tannoudji, C. *Quantum Mechanics*; Hermann, Paris, France, 1977.

(39) Mueller, L. J. *Concepts Magn. Reson. Part A Bridg. Educ. Res.* **2011**.

(40) Bouten, M. On the rotation operators in quantum mechanics. *Physica*, 1969, *42*, 572–580.

(41) Herzfeld, J.; Berger, A. E. *J. Chem. Phys.* **1980**, *73*, 6021.

(42) Sattler, M.; Schleucher, J.; Griesinger, C. *Prog. Nucl. Magn. Reson. Spectrosc.* **1999**, *34*, 93.

(43) Mananga, E. S.; Reid, A. E.; Charpentier, T. *Solid State Nucl. Magn. Reson.* **2012**, *41*, 32.

(44) Sorensen, O. W.; Eich, G. W.; Levitt, M. H.; Bodenhausen, G.; Ernst, R. R. *Prog. NMR Spectrosc.* **1983**, *16*, 163.

(45) Hartmann, S.; Hahn, E. *Phys. Rev.* **1962**, *128*, 2042.

(46) Franks, W. T.; Zhou, D. H.; Wylie, B. J.; Money, B. G.; Graesser, D. T.; Frericks, H. L.; Sahota, G.; Rienstra, C. M. *J. Am. Chem. Soc.* **2005**, *127*, 12291.

(47) Thiriot, D. S.; Nevzorov, A. a; Zagyanskiy, L.; Wu, C. H.; Opella, S. J. *J. Mol. Biol.* **2004**, *341*, 869.

(48) Al-Kaysi, R. O.; Müller, A. M.; Bardeen, C. J. *J. Am. Chem. Soc.* **2006**, *128*, 15938.

Chapter 2

Long Observation Window Band Selective Homonuclear Decoupling (LOW-BASHD): Increased Sensitivity and Resolution in Solid-State NMR Spectroscopy of Proteins

2.1 Introduction

Sensitivity and resolution are important issues for applying solid-state NMR techniques on biological systems. The advancement of hardware design, pulse sequence methodologies, and sample preparation has been progressing rapidly. And it is common for solid-state NMR spectroscopy to resolve *J*-couplings between ^{13}C nuclei in uniformly ^{13}C enriched proteins nowadays.[1,2] Although, in cases for uniformly ^{13}C (and with or without ^{15}N) enriched biological macromolecules, at least twice the number of ^{13}C peaks can be observed as compared to the number of ^{13}C sites because of peak splitting by one-bond ^{13}C-^{13}C *J*-couplings. The splitting also lead to intensities distributed among multiplet for each chemically distinguishable carbon site, thus lowering the sensitivity. The removal of *J*-couplings between ^{13}C's can result in cleaner spectra (less crowded peaks), and increased sensitivity (due to the condensation of distributed intensities into one peak).

J-couplings are through bond indirect dipole-dipole interactions between nuclei spins. These interactions are independent of applied field, or chemical environment. For directly bonded carbons in a protein, typical *J*-coupling strength is 30-75 Hz.[1] For a protein backbone, the C^{α}-C', C^{α}-N, C'-N, and C^{α}-C^{β} *J*-coupling strengths are around 55 Hz, 11 Hz, 15 Hz, and 35 Hz respectively.[3] Here C' denotes the carbonyl carbons. There is little

variation of *J*-coupling strengths from protein to protein, and the removal of the information does not affect our knowledge of a protein structure.

While MAS can average out (or remove) most CSA effects, and partially the dipolar coupling effects, the effective *J*-coupling constant are scalar terms, and do not vary by spatial rotations induced by MAS. The removal of *J*-couplings can be achieved by RF pulse sequencing techniques in a multidimensional NMR correlation spectrum of uniformly-^{13}C, ^{15}N enriched biological microcrystal sample.[4]

For homonuclear *J*-couplings in the indirect dimensions, a number of highly-effective methods are already developed, such as selective pulses,[5–8] multiple quantum coherences,[9,10] and constant-time techniques.[2,11–13] In the direct acquisition dimension, the removal of *J*-coupling interactions is equally desired. And the need inspired the development of spin-state-selective based techniques,[14–19] and band selective homonuclear decoupling (BASHD). The spin-state-selective experiments record a pure in-phase and a pure antiphase spectrum separately by using the S^{3}E (Spin State Selective Excitation) filter right before acquisition.[19] For each separated ^{13}C-^{13}C spin pairs, the recombination of the two experiments by addition or subtraction will cancel out one component of each doublet. The resulted two spectra, from addition and subtraction, again can be recombined to take advantage of the doubled number of scans, and resulted in the removal of the homonuclear *J*-coupling induced splitting and the condensed intensities. The theoretical sensitivity gain for the methods is limited to $\sqrt{2}$ due to the addition of noise at the same time when combining the separately recorded spectra. Also polarizations have to evolve under *J*-couplings for several milliseconds before the actual acquisition. For quickly relaxing

systems, this leads to the sensitivity being lower then the theoretical $\sqrt{2}$ value. While the spin-state-selective methods rely on the S^3E filter before acquisition, the BASHD directly implements *J*-decoupling during acquisition.[20–23] ^{13}C, ^{13}C *J*-couplings are removed by frequently interweaved RF irradiations and detection windows. The sensitivity gain of BASHD is determined by window durations of detection and irradiation, and the optimum improvement for sensitivity is of factor 1.2.

Here an alternative, high-sensitivity method is developed for band-selective homonuclear decoupling of backbone alpha-carbon (C^{α}) and carbonyl (C') nuclear spins during direct ^{13}C acquisition. The technique is based upon a novel long-observation-window band-selective homonuclear decoupling (LOW BASHD) scheme. LOW-BASHD detection avoids the detrimental effect of low detection duty cycle on sensitivity inherent in rapid, stroboscopic BASHD techniques and requires no additional delay periods be incorporated into the sequence. The method provides both increased sensitivity and resolution, with signal-to-noise ratio (S/N) up to 1.8 for C' detection. LOW-BASHD detection can be incorporated into standard NMR experiments that detect on ^{13}C, as illustrated below for CACO and NCA correlation spectroscopy applied to the β1 immunoglobulin binding domain of protein G (GB1) and 3D CBCACO correlation spectroscopy applied to the α-subunit of tryptophan synthase (α -TS).

2.2 Experimental Section

NMR spectroscopy experiments were performed at 9.4 T (400.37 MHz ^1H, 100.69 MHz ^{13}C, 40.57 MHz ^{15}N) on a Bruker AVIII spectrometer equipped with an ^1H–^{13}C-^{15}N

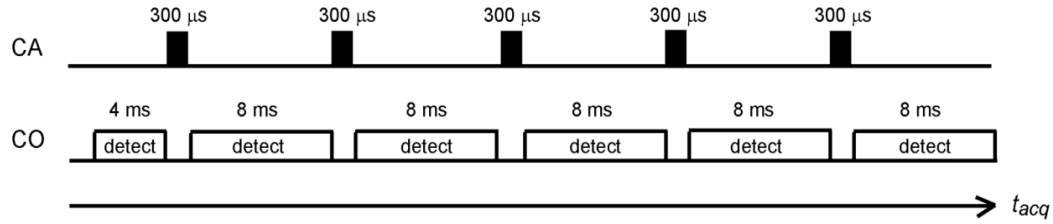

Figure 2.1. Detection scheme for long-observation window band-selective homonuclear decoupling (LOW BASHD) in which evolution under the *J*-coupling interaction between detect and partner spins (shown here as C' and C^{α}, respectively) is refocused at multiples of the decoupling period (τ_{dec}) by the application of short, selective π pulses on the decoupled partner.

triple resonance 2.5mm MAS probe. All experiments were performed at a MAS rate of 20 kHz. Cross-polarization from ^{1}H to 13C (or ^{15}N for NCA correlation experiments) was accomplished at a ^{1}H spin-lock field of 73 kHz (tangent ramped ± 10 kHz) and ^{13}C (^{15}N) spin-lock of 53 kHz; 85 kHz XiX ^{1}H decoupling[24] (τ_{pulse} = 92.5 μs) was used during direct acquisition. In all experiments, a digitally-oversampled FID (sampling dwell 0.025 μs) was acquired and subsequently digitally filtered to produce a time-domain signal before Fourier transformation. LOW-BASHD detection was implemented using the detection scheme shown in Fig. 2.1 with experiment-specific parameters given below.

1D CP-MAS experiments were performed on U-^{13}C,^{15}N-labeled glycine with and without LOW BASHD. A digitally-filtered time-domain signal consisting of 128 complex-valued time-domain points spaced at 400 μs (spectral width 2.5 kHz, t_{acq} = 51.2 ms) was acquired with the spectral window centered at 175 ppm. LOW-BASHD detection was implemented using τ_{dec} = 8 ms and 200 μs Gaussian π-pulses, cosine modulated at 13.5 kHz.

For multidimensional protein solid-state NMR experiments, the temperature of the bearing gas was cooled to 263 K, resulting in an effective sample temperature of ~5 °C due to frictional heating. Hard π/2 and π pulses at 83 kHz for ^{13}C were used throughout, along with 140 kHz XiX ^{1}H decoupling during indirect evolution, constant time intervals, and refocusing periods, and 85 kHz XiX decoupling during z-filters[25] and direct detection. Chemical shifts were referenced on the DSS scale using adamantane as an external secondary chemical shift standard at 40.48 ppm (downfield peak).

2D CTUC COSY CACO correlation experiments were performed using the pulse sequence reported previously.[11] The mixing times for the CTUC COSY were set to τ_1 = 4.0 ms and τ_2 = 4.5 ms. In the indirect dimension, 318 complex points with a dwell of 25 μs (spectral width 40 kHz, total acquisition time 7.95 ms) were acquired. In the direct dimension, 128 complex points with a dwell of 400 μs were acquired (spectral width 2.5 kHz, total acquisition time 51.2 ms) with and without LOW-BASHD decoupling (τ_{dec} =8 ms and τ_{pulse} = 200 μs; Gaussian π-pulse, cosine modulated at 13 kHz). 8 scans per transient were averaged with a relaxation delay of 4 s for a total experiment time of 5 h, 48 min.

2D NCA correlation experiments were performed using SPECIFIC CP transfer[26] from ^{15}N to ^{13}C at a ^{15}N field of 7.25 kHz and ^{13}C spin-lock field of 12.75 kHz (tangent ramped ±2 kHz). In the indirect dimension, 64 complex points with a dwell of 250 μs (spectral width 4 kHz, total acquisition time 16 ms) were acquired, with the spectral window centered at 120 ppm. In the direct dimension, 128 complex points with a dwell of 300 μs were acquired (spectral width 3.333 kHz, total acquisition time 38.4 ms) with and without LOW-BASHD decoupling (τ_{dec} = 8 ms and τ_{pulse} = 200 μs; Gaussian π-pulse, cosine

modulated at 12 kHz), as described above. 64 scans per transient with a relaxation delay of 4 s were averaged for a total experiment time of 9 h, 20min.

3D constant-time J-MAS CBCACO correlation experiments were performed using the pulse sequence in a previous work.[1] A selective 225 μs r-SNOB pulse was used for the aliphatic-selective π pulse in t_1 and the *J*-transfer delays were set to τ_1 = 7.0 ms, τ_2 = 5.0 ms, and τ_4 = 5.0 ms. As described previously,[2,11] setting τ_1 = 7.0 ms selects against residues with an aliphatic C^{γ}, making this experiment semi-selective for alanine, cysteine, serine, asparagine, and aspartic acid residues; aromatic residues are also substantially suppressed due to the bandwidth of the selective pulse. During t_1 and t_2, the carrier frequency for carbon was placed near the center of the aliphatic carbon resonances (39 ppm), while

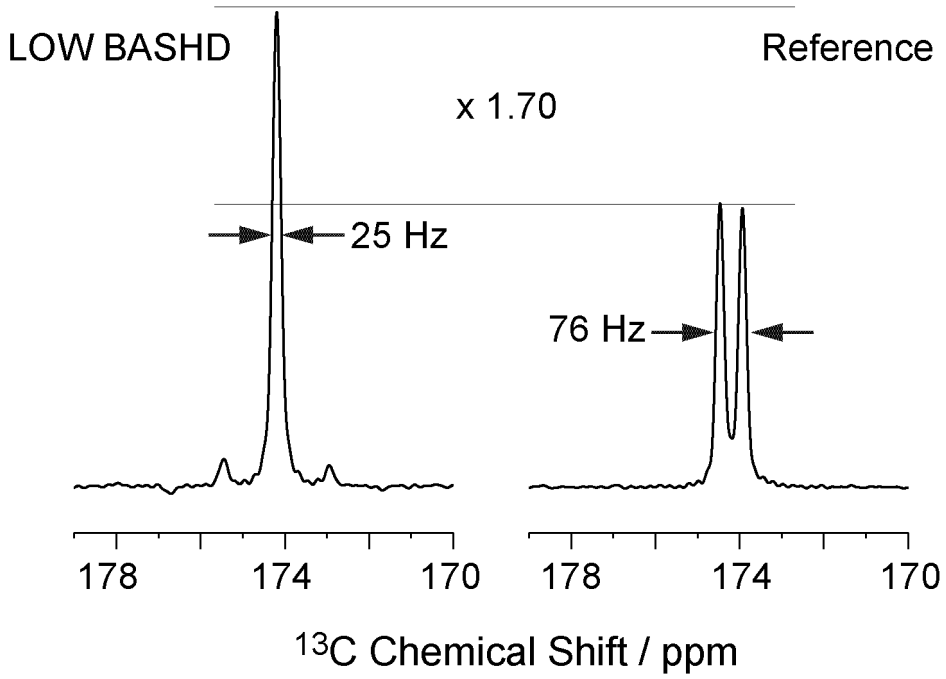

Figure 2.2. CP-MAS spectrum of U-^{13}C,^{15}N-glycine acquired with standard (right) and LOW-BASHD (left) detection. Partial evolution under the J-coupling interaction during the long refocusing periods leads to the decoupling sidebands observed in the LOW-BASHD spectrum.

during t_3 it was moved to 177 ppm for $^{13}C'$ detection. In both indirect dimensions, 64 complex points with a dwell of 150 μs (spectral width 6666 kHz, total acquisition time 9.6 ms) were acquired. In the direct dimension, 64 complex points with a dwell of 400 μs were acquired (spectral width 2.5 kHz, total acquisition time 25.65 ms) with and without LOW-BASHD decoupling (τ_{dec} = 8 ms and τ_{pulse} = 200 μs; Gaussian π-pulse, cosine modulated at 12 kHz). 8 scans per transient were averaged with a relaxation delay of 3 s for a total experiment time of 4 days, 21 h, 5 min.

2.3 Results and Discussion

The goal of band-selective homonuclear decoupling is to observe one partner of a *J*-coupled pair while refocusing the scalar-coupling interaction between them. BASHD experiments in uniformly ^{13}C labeled proteins can take advantage of the ~120 ppm separation between C' and C^{α} spins and the relatively consistent value of $^{1}J_{C^{\alpha}C'}$ of 55 Hz to achieve band-selective homonuclear decoupling using long-observation windows. The general scheme for LOW-BASHD detection is shown in Fig. 1, where long detection windows (~4–8 ms) are punctuated by short (~200 μs) pulse breaks, during which selective refocusing pulses are applied to one partner of a *J*-coupled pair; this is illustrated in Fig. 1 for the case of C' detection with decoupling of C^{α}, but would be equally applicable to C^{α} detection with decoupling pulses on C'. The application of the selective π pulses refocuses the *J*-coupling interaction at integer multiples of the decoupling period, τ_{dec}. The length of the detection and pulse windows are optimized to circumvent line shape distortion or lowered effective detection duty cycle.

Fig. 2.2 shows the application of LOW BASHD during C' detection for U-^{13}C,^{15}N-glycine; for comparison, a reference spectrum without LOW BASHD is shown. In the LOW-BASHD detected spectrum, the *J*-coupling to C^{α} has been removed, with a corresponding increase in intensity by a factor of 1.70. Decoupling sidebands flanking the C' resonance have been introduced, but are less than 5% the intensity of the main resonance. These sidebands result from partial evolution under the *J*-coupling interaction during the relatively long *J*-refocusing periods. The spacing and intensity of the decoupling sidebands

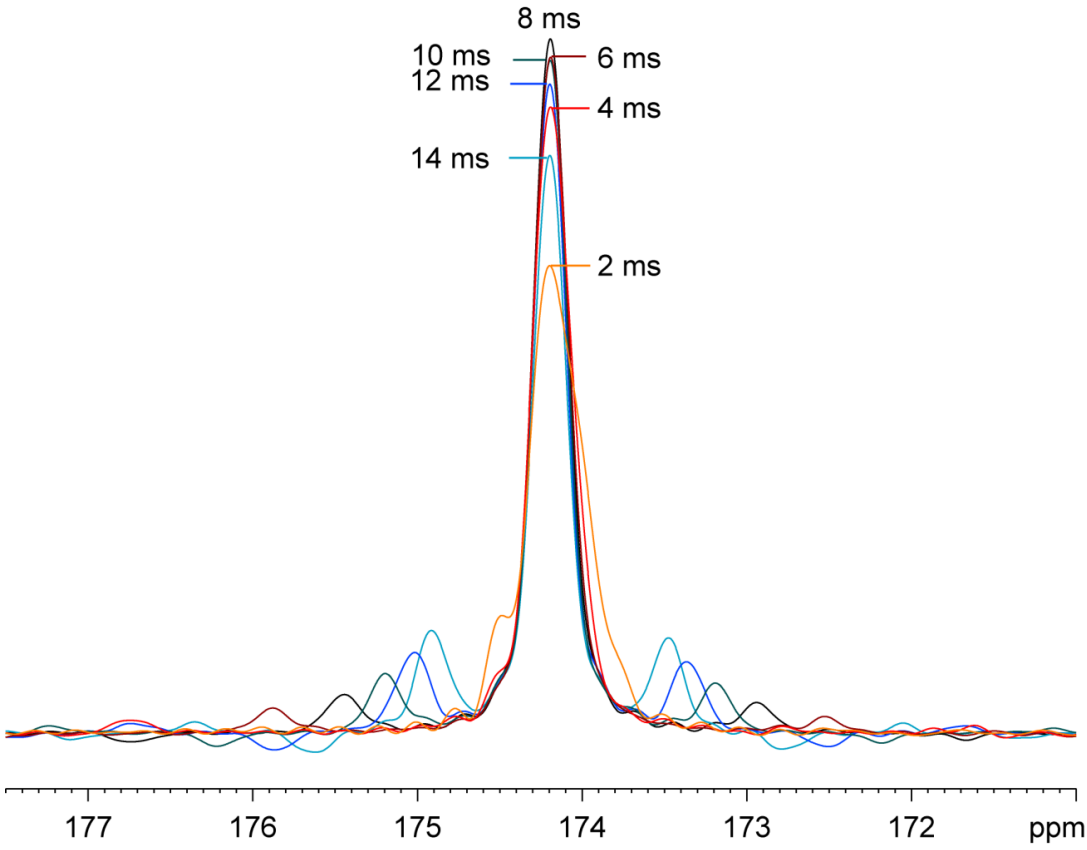

Figure 2.3. LOW-BASHD detected CP-MAS spectrum of U-^{13}C,^{15}N-glycine acquired with varying refocusing periods, τ_{dec}. As the refocusing periods become shorter, the decoupling sidebands become less intense and push further out. At the same time, the more frequent application of refocusing pulses leads to intensity loss due to lower duty-cycle detection and the accumulation of off-resonance pulse effects. The optimum balance between these two effects is found at τ_{dec} = 8 ms.

are modulated by the decoupling cycle time (τ_{dec}), with more rapid application of decoupling pulses resulting in less intense, more widely-spaced sidebands. Rapid pulsing, however, leads to an overall lower duty cycle for detection (the receiver must be turned off during the application of the decoupling pulses), as well as the accumulation of off-resonance pulse effects[27] within the spectral window of the observe spins. Both of these lower the intensity of the main resonance. Fig. 2.3 shows the experimental optimization of the spectrum versus decoupling period; 8 ms was chosen above to maximize the main peak intensity. This long period between decoupling pulses means that only 6 pulses are necessary to achieve efficient homonuclear decoupling over the 50 ms acquisition time of the FID. Note that to help compensate for first-order, off-resonance pulse effects, a cosine-

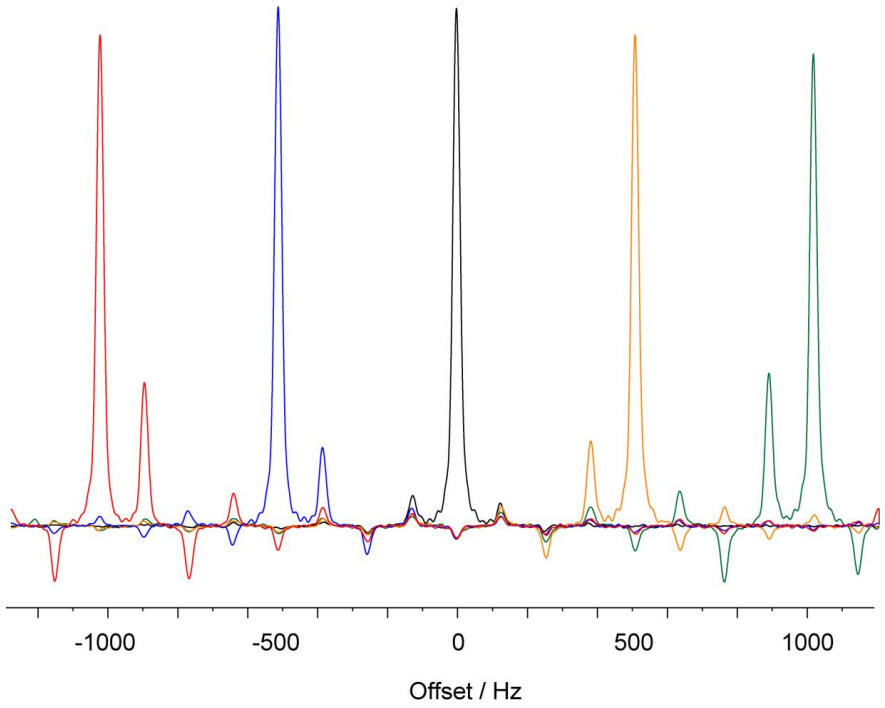

Figure 2.4. CP-MAS spectrum of U-^{13}C,^{15}N-glycine acquired with "cut-and-stitch" LOW BASHD detection for varying frequency offsets.

modulated refocusing pulse is used, which composed of two lobes of effective excitation at +/− the modulation frequency, with one lobe centered on the desired decoupling region.

Because the receiver must be gated off during the time that the pulses are applied, there will be brief periods under LOW BASHD during which the FID cannot be observed. There are two options for dealing with this complication while recording the FID. The first is to suspend the digitizer (and its clock) during the decoupling pulses; the second is to leave the digitizer running with the receiver gated off. The former ‘‘cut-and-stitch’’ method effectively excises the gaps in the FID and this was the method used to acquire the spectrum in Fig. 2.2. However, the cut-and-stitch procedure suffers frequency-dependent line shape distortions (Fig. 2.4) due to signal discontinuities that appear at the stitch points and

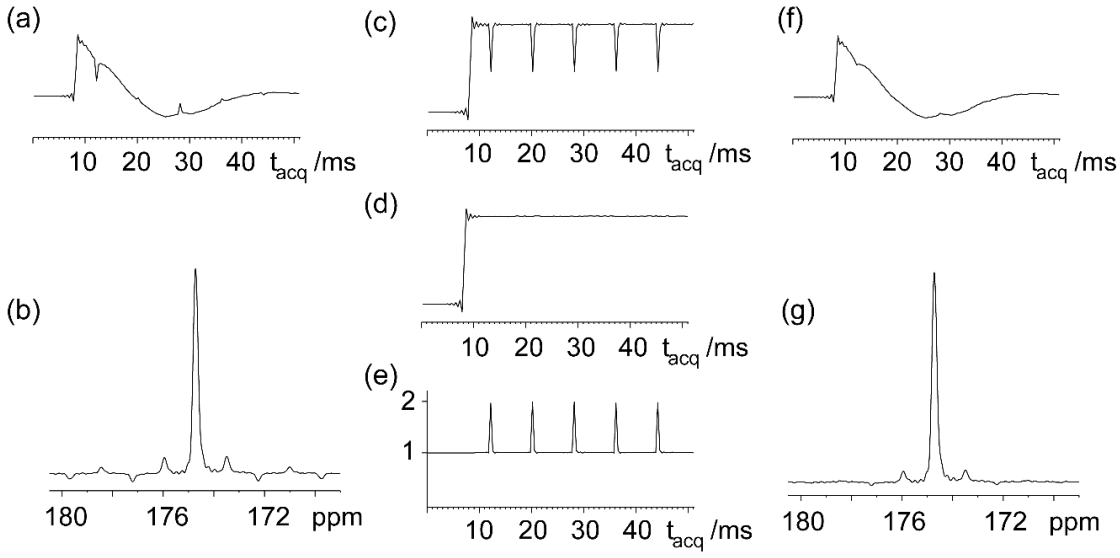

Figure 2.5. The LOW-BASHD filter. (a) The FID and (b) corresponding spectrum of U-^{13}C,^{15}N-glycine acquired under LOW-BASHD detection using the crevasse method. (c) The time-domain signal for a constant DC voltage input (the DC offset of the receiver) digitized under LOW-BASHD and (d) standard detection. (e) The LOW-BASHD filter is the quotient of (d) and (c) (with the initial group delay period set to 1) and multiplies (a) to give the frequency-domain-deconvoluted (f) FID and (g) spectrum.

become progressively larger with frequency offset; there is also a slight frequency scaling of the spectrum. The second ‘‘crevasse’’ method digitizes the zeroed output of the receiver, leading to periodic holes in the digitized FID (Fig. 2.5) that give rise to a series of frequency-domain ‘‘sampling’’ sidebands as shown in Fig. 2.5b. The effect of the pulse breaks on the FID are relatively minor because the digital filtration already applied to the oversampled data convolutes a time-domain filter function[28] to produce a signal that does not have sufficient time to fully decay to zero during the gap periods. Here the data were acquired with a sampling dwell of 400 μs (spectral window of 2500 Hz), corresponding to a relatively broad associated time-domain filter function. At shorter dwell times (larger spectral window, narrower time-domain convolution partner), the signal does indeed fall to zero during the decoupling-pulse periods. In the Fig. 2.6, when data were acquired with a sampling dwell of 16 μs (spectral window of 62.5 kHz), the dwell time corresponds to a relatively narrow associated time-domain filter function. This setup allowed the signal to fall to zero during the decoupling pulse period, and served as an extreme case of the demonstration.

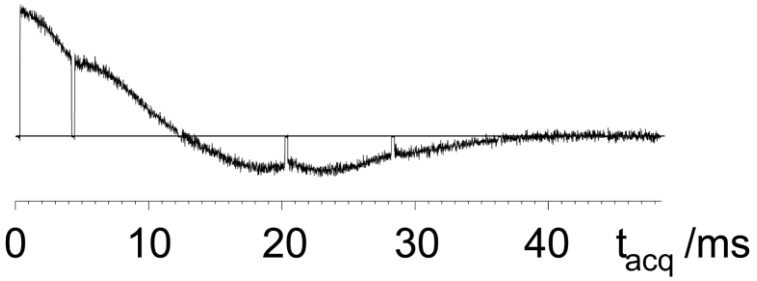

Figure 2.6. Periodic holes in the digitized FID caused by the turned off receiver during decoupling pulses. The data were acquired with very short sampling dwell time (16 μs), allowing the singal to fall to zero during the decoupling pulse periods.

While the sampling sideband intensities (Fig. 2.5g) are small enough to be negligible in some cases, it is still desirable in most situations to remove them. There are several ways that this can be accomplished, including linear prediction and interpolation across the gaps in the time domain signal, and deconvolution in the frequency domain by the application of a suitable time-domain filter.[29,30] We choose the latter method as the more general: once an appropriate LOW-BASHD filter is found, it can be used to process any directly detected signal acquired with the same sampling parameters (digitizer dwell time, frequency-domain filter, and LOW-BASHD sampling schedule). Although the LOW-BASHD filter is in principle calculable, it can also be determined experimentally. Fig. 2.5 shows the time-domain signal for a constant amplitude input (in this case, the DC offset of the receiver) digitized using standard (d) and LOW-BASHD (c) sampling. The LOW-BASHD filter is their respective quotient (with the values during the initial group delay period[31] set to 1) shown in Fig. 2.5e and applied to the FID (Fig. 2.5a) to give the LOW-BASHD corrected FID in Fig. 2.5f, with the corresponding homonuclear decoupled spectrum shown in Fig. 2.5g. The same filter function can be applied to spectral lines at any offset frequency within the spectral window. Because the offset dependence is small, as demonstrated in Fig.2.7. The filter function generated, as shown in Fig 2.5, is used below for pre-processing the directly detected dimension in 2D and 3D correlation spectroscopy experiments acquired under LOW BASHD.

A major advantage of LOW-BASHD detection is that it can be incorporated into any experiment that detects on ^{13}C. Fig. 2.8 shows four examples: the through-bond, CTUC COSY CACO correlation spectrum[11] of GB1, the through-space, SPECIFIC CP[26] NCO

and NCA correlation spectrum of GB1, and the through-bond, constant-time *J*-MAS CBCACO 3D correlation spectrum[1] of α-TS. The through-bond CACO correlation spectrum of GB1 shows S/N enhancements in the range of 1.67–1.82 for LOW-BASHD compared to standard detection, with a corresponding improvement of 3 in resolution as the ~55 Hz coupling to C^{α} is removed. Similar gains are found in the NCO correlation spectrum of GB1. LOW-BASHD detection on C^{α}, used to acquire the NCA correlation spectrum of GB1 shown in Fig. 2.8b, increases sensitivity only at glycine residues, but still offers improved resolution as the near 1:2:1 intensity triplets (which result from couplings

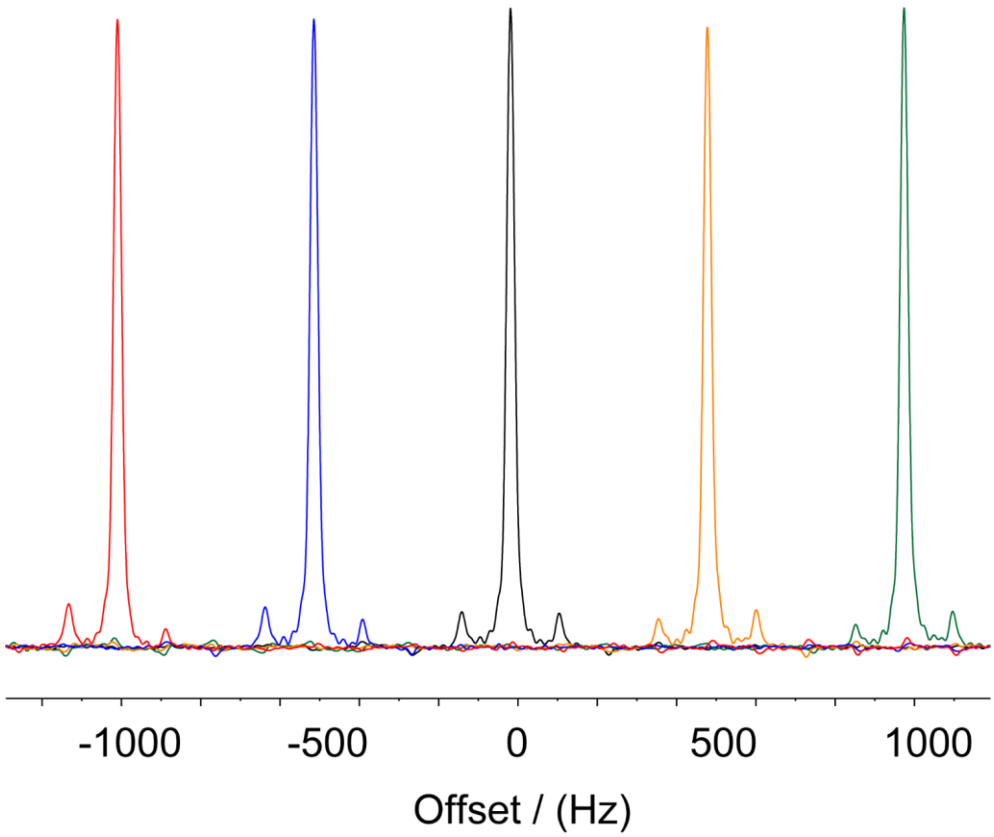

Figure 2.7. CP-MAS spectrum of U-^{13}C,^{15}N-glycine acquired with the "crevasse" method of LOW-BASHD detection for varying frequency offsets. The signal was multiplied by the LOW-BASHD filter before being Fourier transformed. The spectral window was centered at 175 ppm.

to both C’ and C^{β}) are condensed to narrower 2:2 doublets. LOW BASHD is designed to remove only the coupling between C^{α} and C’; coupling between C^{α} and C^{β} can be removed by fast stroboscopic BASHD techniques,[20] but only with reduced S/N. Finally, Fig. 2.8c shows the alanine region of the 3D CBCACO through-bond correlation spectrum of the

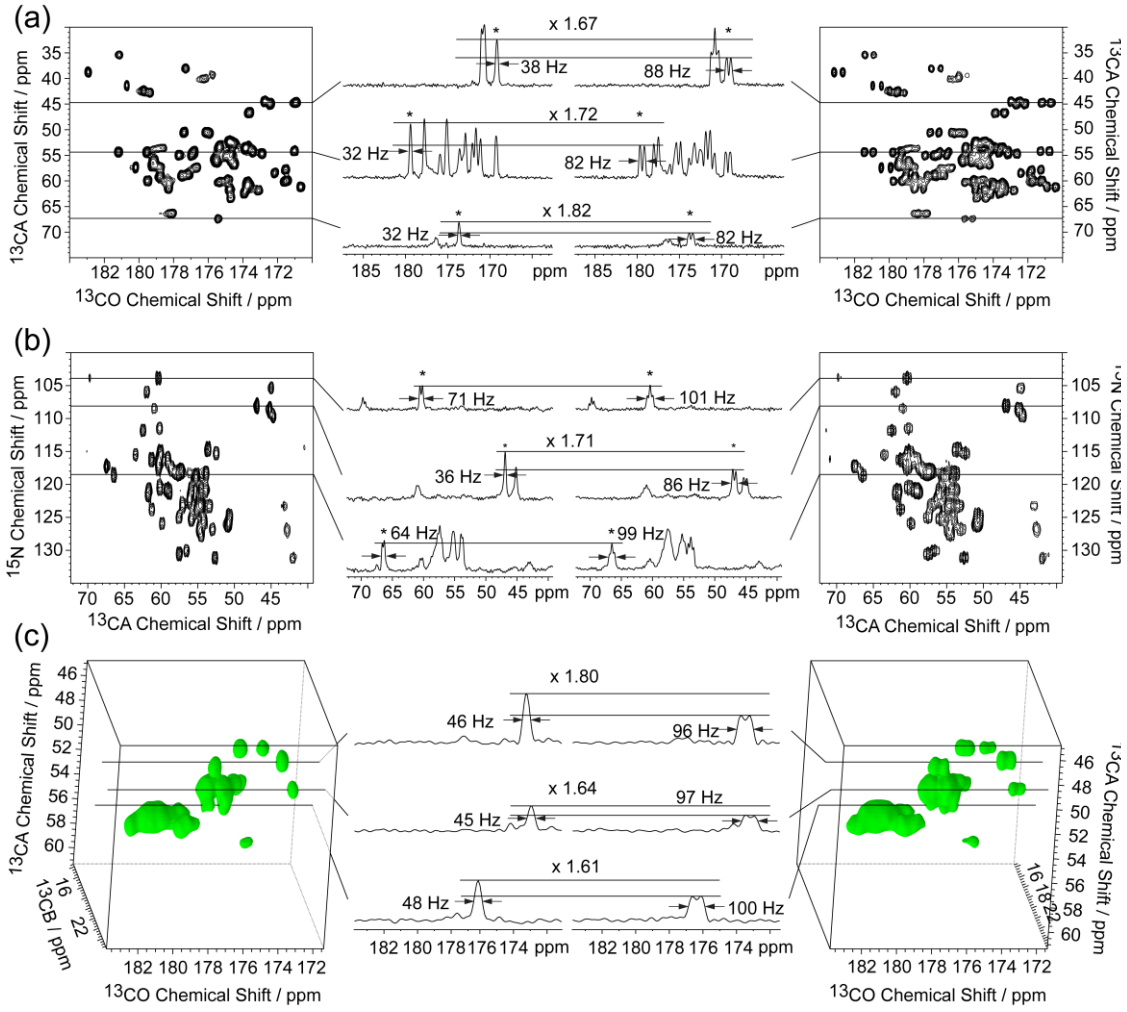

Figure 2.8. Comparisons of LOW-BASHD (left) and standard (right) detection for multidimensional solid-state NMR correlation spectroscopy. (a) The CTUC CACO correlation spectrum of GB1 shows increased sensitivity and resolution for LOW-BASHD detection on C′, while (b) the NCA correlation spectrum of GB1 shows increased sensitivity at glycine residues and improved resolution at all residues using LOW-BASHD detection on C^{α}. (c) The alanine region of the constant-time, J-MAS 3D CBCACO correlation spectrum of α-TS shows increased sensitivity and resolution for LOW-BASHD detection on C′.

28.5 kDa α-TS. There are 40 alanine resonances in this region, many of which are now resolved. Here again, S/N enhancements in the range of 1.61–1.81 are observed and, even with a more modest acquisition time of 26 ms in the direct dimension, improvements in resolution of a factor or 2 are seen.

LOW-BASHD detection offers higher gains in sensitivity than appended in-phase/anti-phase (IPAP)[1,17,19,32] and related spin-state-selective (S^3) techniques[15] in which two independent spectra (pure or mixed combinations of in-phase and anti-phase components) are acquired. While these techniques are extremely robust, and in our hands give essentially the full theoretical improvement in S/N of $\sqrt{2}$, there is a distinct benefit to techniques such as LOW BASHD that collapse the multiplet structure directly during observation rather than combining independent multiplet components along with their associated noise from two frequency ranges: a necessary step to get the maximum S/N increase in IPAP/S^3 experiments. Indeed, compared to IPAP at its theoretical maximum enhancement, we see an additional 20–40% increase in S/N for the LOW-BASHD detected experiments.

2.4 Conclusion

Sensitivity and resolution remain the two fundamental obstacles to extending solid-state nuclear magnetic resonance to even larger protein systems; LOW-BASHD detection can improve both at a very modest cost in experimental complexity. In LOW BASHD, a single selective refocusing pulse every 8 ms is sufficient to effectively decouple C^{α} and C' nuclei, allowing for long observation windows and high sensitivity during homonuclear decoupling. While detection using the crevasse method requires a separate LOW- BASHD

filter be determined for each combination of LOW-BASHD sampling schedule and digital filter setting, these need only be measured once and can be derived experimentally quickly with very high signal-to-noise ratios. Finally, we note that although demonstrated here for solid-state NMR, LOW-BASHD detection would be equally applicable to ^{13}C-detected NMR spectroscopy of proteins in solution.[33]

2.5 References

(1) Ye, T.; Chen, L.; Niks, D.; Kaiser, J. M.; Lai, J.; Rienstra, C. M.; Dunn, M. F.; Mueller, L. J. *Phys. Chem. Chem. Phys.* **2009**, *11*, 6875.

(2) Chen, L.; Kaiser, J. M.; Polenova, T.; Yang, J.; Rienstra, C. M.; Mueller, L. J. *J. Am. Chem. Soc.* **2007**, *129*, 10650.

(3) Sattler, M.; Schleucher, J.; Griesinger, C. *Prog. Nucl. Magn. Reson. Spectrosc.* **1999**, *34*, 93.

(4) Goldman, M.; Webb, G. A. *Magn. Reson. Chem.* **1989**, *27*, 1.

(5) Igumenova, T. I.; McDermott, A. E. *J. Magn. Reson.* **2005**, *175*, 11.

(6) Shi, L.; Peng, X.; Ahmed, M. A. M.; Edwards, D.; Brown, L. S.; Ladizhansky, V. *J. Biomol. NMR* **2008**, *41*, 9.

(7) Li, Y.; Wylie, B. J.; Rienstra, C. M. *J. Magn. Reson.* **2006**, *179*, 206.

(8) Straus, S. K.; Bremi, T.; Ernst, R. R. *Chem. Phys. Lett.* **1996**, *262*, 709.

(9) Bermel, W.; Bertini, I.; Felli, I. C.; Kümmerle, R.; Pierattelli, R. *J. Am. Chem. Soc.* **2003**, *125*, 16423.

(10) De Paëpe, G.; Giraud, N.; Lesage, a; Hodgkinson, P.; Böckmann, a; Emsley, L. *J. Am. Chem. Soc.* **2003**, *125*, 13938.

(11) Chen, L.; Olsen, R. a; Elliott, D. W.; Boettcher, J. M.; Zhou, D. H.; Rienstra, C. M.; Mueller, L. J. *J. Am. Chem. Soc.* **2006**, *128*, 9992.

(12) Chen, L.; Kaiser, J. M.; Lai, J.; Polenova, T.; Yang, J.; Rienstra, C. M.; Mueller, L. J. *Magn. Reson. Chem.* **2007**, *45*.

(13) Zhong, L.; Bamm, V. V.; Ahmed, M. A. M.; Harauz, G.; Ladizhansky, V. *Biochim. Biophys. Acta - Biomembr.* **2007**, *1768*, 3193.

(14) Verel, R.; Manolikas, T.; Siemer, A. B.; Meier, B. H. *J. Magn. Reson.* **2007**, *184*, 322.

(15) Laage, S.; Lesage, A.; Emsley, L.; Bertini, I.; Felli, I. C.; Pierattelli, R.; Pintacuda, G. *J. Am. Chem. Soc.* **2009**, *131*, 10816.

(16) Kehlet, C.; Nielsen, J. *J. Phys. …* **2011**, 543.

(17) Duma, L.; Hediger, S.; Brutscher, B.; Bo, A.; Lyon, D.; Biologie, I. De; Ebel, S. J.; Cea, C.; De, I.; Cnrs, U. M. R. **2003**, 11816.

(18) Nielsen, N. C.; Thogersen, H.; Sorensen, O. W. *J.Am.Chem.Soc.* **1995**, *117*, 11365.

(19) Duma, L.; Hediger, S.; Lesage, A.; Emsley, L. *J. Magn. Reson.* **2003**, *164*, 187.

(20) Chevelkov, V.; Chen, Z.; Bermel, W.; Reif, B. *J. Magn. Reson.* **2005**, *172*, 56.

(21) Jesson, J. P.; Meakin, P.; Kneissel, G. *J. Am. Chem. Soc.* **1973**, *95*, 618.

(22) Hammarstroem, A.; Otting, G. *J. Am. Chem. Soc.* **1994**, *116*, 8847.

(23) Vögeli, B.; Kovacs, H.; Pervushin, K. *J. Biomol. NMR* **2005**, *31*, 1.

(24) Detken, A.; Hardy, E. H.; Ernst, M.; Meier, B. H. *Chem. Phys. Lett.* **2002**, *356*, 298.

(25) Sorensen, W.; Rance, M.; Ernst, R. R. **1984**, *534*.

(26) Baldus, M.; Petkova, A. T.; Herzfeld, J.; Griffin, R. G. *Mol. Phys.* **1998**, *95*, 1197.

(27) Emsley, L.; Bodenhausen, G. Phase shifts induced by transient Bloch-Siegert effects in NMR. *Chemical Physics Letters*, 1990, *168*, 297–303.

(28) Bracewell, R. N. *The Fourier Transform and Its Applications*; McGraw Hill: Boston, 2000.

(29) Morris, G. A.; Barjat, H.; Home, T. J. Reference deconvolution methods. *Progress in Nuclear Magnetic Resonance Spectroscopy*, 1997, *31*, 197–257.

(30) Morris, G. A. *J. Magn. Reson.* **1988**, *80*, 547.

(31) Moskau, D. *Concepts Magn. Reson.* **2002**, *15*, 164.

(32) Franks, W. T.; Zhou, D. H.; Wylie, B. J.; Money, B. G.; Graesser, D. T.; Frericks, H. L.; Sahota, G.; Rienstra, C. M. *J. Am. Chem. Soc.* **2005**, *127*, 12291.

(33) Bermel, W.; Bertini, I.; Duma, L.; Felli, I. C.; Emsley, L.; Pierattelli, R.; Vasos, P. R. *Angew. Chemie - Int. Ed.* **2005**, *44*, 3089.

Chapter 3

Protonation States of Tryptophan Synthase Intermediates

3.1 Introduction

Tryptophan Synthase (TS) catalyzes the last two steps of the synthesis of L-tryptophan.[1–6] The enzyme is constituted by two αβ-dimeric units. In the α-subunit, indole and D-glyceraldehyde 3-phosphate (G3P) are produced from 3-indole-D-glycerol 3'-phosphate (IGP). The existence of a 25 Å long tunnel between α-subunit and β-subunit facilitates the transfer of indole from the α-subunit into the β-subunit.[2] At the β-site, catalysis based on pyridoxal-5'-phosphate (PLP) first make happen the β-elimination reaction of the substrate L-Serine, resulting in the α-aminoacrylate intermediate, E(A-A). Then the channeled indole from the α-site reacts with E(A-A), and produces L-Tryptophan in the end.

This work has been focused on the reactions at the β-site, where the PLP coenzyme plays an important role in catalyzing the process.[7,8] PLP is the bioactive form of vitamin B_6, and have been involved in multiple amino acid transformations.[9–11] In tryptophan synthase, the PLP-dependent β-site reaction is divided into two stages.[12] In the first stage, the reaction started with PLP being covalently bound to a lysine sidechain ε-nitrogen near the active site. This intermediate is named as internal aldimine, E(Ain). Then when L-serine substrate is introduced into the active site within β-subunit, gem-diamine, E(GD_1), would form, within which nitrogen of L-serine is bound to the C_4' of PLP. After the attachment of L-serine, the coenzyme complex detached the lysine from protein, and is converted to the quasi-stable E(A-A), via external aldimine, E(Aex_1), and L-Ser

quinonoidal, E(Q_1), intermediates. Then, the presence of indole, transferred from the tunnel, at the active site of β-subunit launched the stage II of the reaction, where the indole attacks on the C^{β} of E(A-A), forming the L-Trp quinonoid species E(Q_2). The intermediate is further converted to three other intermediates, the second L-Trp quinonoid E(Q_3), the L-Trp external aldimine E(Aex_2), and the L-Trp gem-diamine E(GD_2), producing L-Tryptophan. And with L-Tryptophan detached, the enzyme loops back to the E(Ain), ready for the next catalytic cycle. The process involves multiple enzyme intermediates. Some of them can be stabilized by certain IGP analogs at the α-site, and also indole analogs at the β-site for quinonoid species.[1,2,13,14] The stabilized enzyme intermediate species can first be depicted using single crystal X-ray Diffraction (XRD) studies. And with single crystal XRD structures achieved for these structures, NMR Crystallography further indicates the protonation states within the enzyme active site of the β-subunit.[1,13] The approach produced precise description of the protonation states of TS. The knowledge can help us better interprete catalytic behavior of PLP dependent enzymes.[15–17]

The first step for using SSNMR to study the enzyme crystal structure would have been chemical shift assignments. However, in this case, the size of the enzyme, 144 kDa, has kept us from getting resolution adequate enough for the assignment task.[18,19] Alternatively, the protonation states of the enzyme intermediates were studied using labeling sites selectively introduced into the natural abundance enzyme. In this way, interesting chemical shifts can be extracted, indicating potential protonation states of the enzyme intermediates.

Here we present work using three ^{13}C and one ^{15}N labeling sites carried by the PLP coenzyme and introduced into Tryptophan Synthase. The IGP analog F9 (N-(4'-trifluoromethoxybenzenesulfonyl)-2-aminoethyl phosphate) was used at the α-site, making the α-subunit in its closed conformation, granting activity at the β-site.[2,20,13] Protonation states of E(Ain) and 2-AP quinonoid ($E(Q)_{2AP}$) intermediates are discussed based on the chemical shifts measured on selectively labeled PLP. The chemical shifts are sensitive to the surrounding protonation states. With chemical shifts from multiple locations observed, our knowledge for the reactions at the β-site of TS is steadily accumulating.

3.2 Experimental Section

3.2.1 Preparation of TS/2,2',3-$^{13}C_3$; ^{15}N-PLP:

Tryptophan synthase $\alpha_2\beta_2$ subunits were dissociated and reconstituted with labeled PLP as previously described[19,21–25] with attention called to the following details. Addition of potassium thiocyanate (KSCN) to a final concentration of 1 M to the enzyme solution was followed by a five minute wait at room temperature until reaction initiation. Hydroxylamine was then added to a final concentration of 10 mM, followed by five more

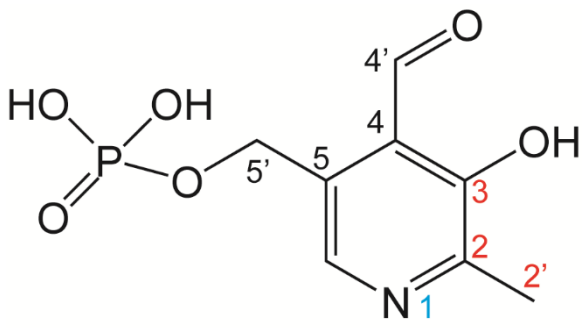

Figure 3.1. The formula of pyridoxal-5'-phosphate (PLP), with ^{15}N enriched, and 2,2',3 ^{13}C enriched.

minutes at room temperature, completing oxime formation. Dissociation was completed with dialysis against Cs-bicine, pH 7.8, containing 1 M KSCN for four hours at 4 °C. This was followed by two more dialyses against plain 50 mM Cs-bicine, pH 7.8, at 4 °C. UV-vis tests on the apoenzyme showed no activity in the presence of substrates. The holoenzyme was resolved by addition of 2,2',3-$^{13}C_3$,^{15}N-PLP (Fig. 3.1) to the dialyzed protein so the final PLP concentration was three times greater than the protein concentration. This solution was incubated in a water bath at 35 °C for 10 minutes. Reassociation of the subunits was completed with addition of L-serine to a final concentration of 15 mM and allowed to sit for 10 more minutes in the warm water bath. The enzyme solution was cooled in an ice bath for 30 minutes, then dialyzed twice against 50 mM Cs-bicine, pH 7.8, at 4 °C. UV/vis activity tests performed on the reconstituted holoenzyme showed fully active enzyme with 70% recovery of the initial concentration, and incorporation of the 2,2',3-$^{13}C_3$;^{15}N-PLP into the enzyme was verified with both ^{13}C and ^{15}N SSNMR.

3.2.2 Preparation of microcrystals of TS enzyme intermediate species

TS was expressed and purified as previously described.[1] Crystallization of TS was accomplished by adding crystallization buffer to protein stock solution in a 1:1 ratio. The crystallization buffer is composed of 14% polyethylene glycol (PEG) 8000 (w/V), 3mM Spermine, and 0.04 mM PLP, and is prepared fresh each time using the pH 7.8 50 mM Cs-bicine buffer. Upon adding the crystallization butter into the TS stock solution, microcrystals of TS should form immediately. Then brief tabletop centrifugation can help collect the microcrystals. F9 was introduced in by soaking the microcrystals in ‘wash

solution'. The wash solution was prepared by diluting the crystallization buffer to a PEG concentration of 10% (from 14%) using the 50 mM Cs-bicine buffer. Then F9 was added in to make a concentration of 3 mM. After F9 being dissolved, the protein microcrystals were submerged in the wash solution for 10 minutes or longer. Then again supernatant can be removed after tabletop centrifugation. The remaining microcrystals are ready for rotor loading, and should be in the form of E(Ain). The E(A-A) was prepared from E(Ain) by adding L-Serine solution (with 8% PEG) to the E(Ain) microcrystals (directly into the rotor in most of the cases). 2-amino phenol (2-AP) is an indole analog which helps produce stable quinonoid intermediate. The 2-AP E(Q) was prepared by adding 2-AP acetonitrile solution to the E(A-A) microcrystals.

3.2.3 UV/vis Spectroscopy

All UV/vis measurements were collected with a Hewlett-Packed 8450A diode-array spectrometer. The absorption values were taken at room temperature. The extinction coefficient of PLP in the 50 mM Cs-Bicine at pH 7.8 was calibrated using purchased PLP from Fisher Bioreagent. Serial dilution was prepared with the 50 mM Cs-bicine buffer. The extinction coefficient so measured was used to determine the concentration of ^{13}C and ^{15}N enriched PLP sample, and the amount to add into the apoenzyme solution. Activity tests for determining protein concentrations were measured using 2-AP and L-serine. The spectrometer is first blanked with 900 µL Cs-bicine buffer. Then 100 µL of the reconstituted TS solution was added to the cuvette for confirmation of E(Ain). 2µL 1M L-Serine solution was further added to form E(A-A). In the end 1 µL of 2-AP saturated in acetonitrile was added in the cuvette for verification by the formation of 2-AP quinonoid.

The extinction coefficient for different TS intermediates in pH 7.8 50 mM Cs-bicine buffer were calibrated from the TS protein concentration determined by the Lowry Method. The calibrated extinction coefficient was 5.3 $mM^{-1}cm^{-1}$ for E(Ain) at 412 nm, 5.2 $mM^{-1}cm^{-1}$ for E(A-A) at 352 nm, and 48 $mM^{-1}cm^{-1}$ for 2-AP quinonoid at 468 nm.

3.2.4 Solid-State NMR Measurements

The solid-state NMR experiments were performed on a Bruker AVIII spectrometer equipped with an ^{1}H-^{13}C-^{15}N triple resonance 4 mm MAS probe spinning at a MAS rate of 8 kHz and with the bearing gas cooled to -15 °C, giving an effective sample temperature of 5 °C. Cross-polarization (CP)[26] was accomplished at an ^{1}H spin-lock field of 45 kHz, an ^{15}N (or ^{13}N) spin-lock field of 37 kHz (ramped ±2 kHz), and a contact time of 2 ms; 85 kHz Spinal64 ^{1}H decoupling was used throughout.[27] The relaxation delay was 4s. ^{15}N spectrum of E(Ain) consists of the sum of 57344 transients, with a total acquisition time of 2 days 16h 27min. 15N spectrum of 2-AP quinonoid consists of the sum of 40960 transients. And the total acquisition time was 1 day 22h 2 min. ^{15}N chemical shifts were referenced indirectly to NH_3(l) via an external solid-state sample of $^{15}NH_4Cl$ ($\delta[NH_3(l)]$ = 39.3 ppm) calibrated under MAS conditions.[28] ^{13}C spectrum of E(Ain) consists of the sum of 10240 transients, for a total acquisition time of 11h 30 min. ^{13}C spectrum of 2-AP quinonoid consists of the sum of 8192 transients. And the total acquisition time was 9h 12min. ^{13}C chemical shifts were referenced indirectly to neat TMS using an external sample of adamantane in which the downfield ^{13}C peak was set to 38.48 ppm.[29] The LOW-BASHD experiments[30] were also performed on the ^{13}C measurements, with decoupling π-pulses optimized on a U-^{13}C,^{15}N Tyrosine sample. The cosine modulated gaussian π pulse of 250

μs at 12 kHz offset was chosen for measurements on the TS/2,2',3-$^{13}C_3$,^{15}N-PLP sample. Details of LOW BASHD were discussed earlier in chapter 2.

3.3 Results and Discussion

The TS $\alpha_2\beta_2$ bienzyme complex relies on PLP to bring together indole and L-serine to form L-tryptophan. The labeling sites directly introduced on the PLP ring appeared to be important spots for indication of the surrounding protonation states. To make sure that the reconstitution of apoenzyme with the labeled PLP was successful, UV/vis activity tests were performed on the reconstituted bienzyme complex. The test result is shown in Fig. 3.2. The absorption at 412 nm confirmed the recombined TS was readily being in the form E(Ain), and is able to form E(A-A) when L-serine is added, with absorption maxima shifted

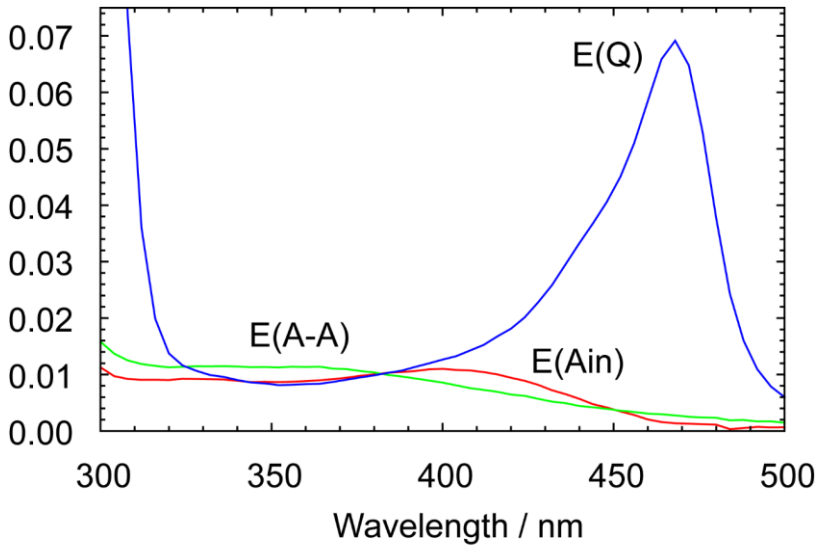

Figure 3.2. UV/vis overlaid spectra of the reconstituted TS underwent the β-site catalytic cycle. The E(Ain) was shown in red. After the addition of L-serine, the absorption maxima was shifted to 352 nm, indicating the formation of E(A-A), as shown in green. Then the addition of 2-AP resulted in the 468 nm absorption, representing E(Q), as shown in blue. The behavior is the same as of native TS holoenzyme.

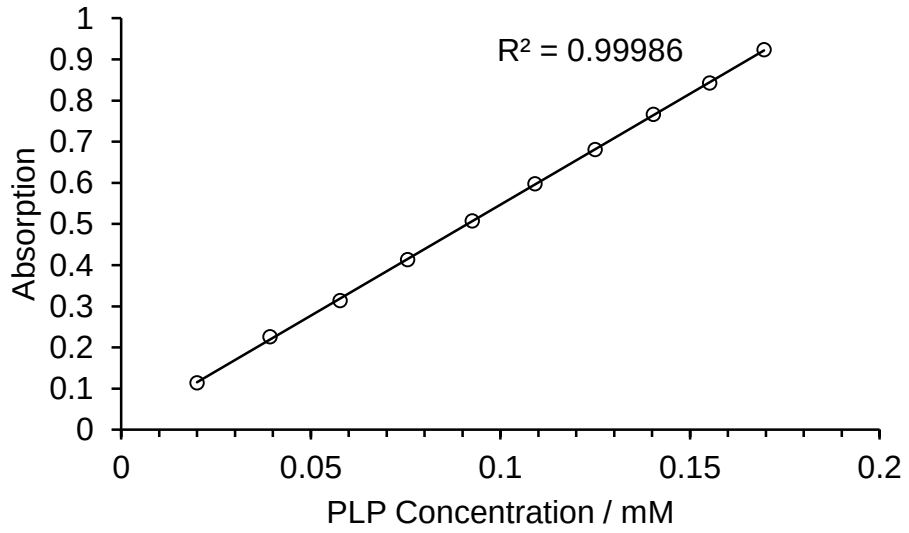

Figure 3.3. The correlation of PLP concentration and absorption at 390 nm using UV/vis spectroscopy. PLP was dissolved in pH 7.8 50 mM Cs-bicine buffer. The measured extinction coefficient is 5.39 $mM^{-1}cm^{-1}$, derived from the slope of the calibration curve.

to 352 nm. The further addition of 2-AP lead to the formation of 2-AP quinonoid $E(Q)_{2AP}$, resulting in the intense absorption at 468 nm. In sum, the reconstituted TS enzyme followed the same behavior as the original holoenzyme. Titration of PLP against the apoenzyme TS also showed that a full conversion from apoenzyme to PLP bound holoenzyme requires PLP of at least three times the molar concentration of the apoenzyme. The amount of PLP was estimated by again the absorption maxima at 468 nm, with the presence of L-serine and 2-AP. The maximum conversion of apoenzyme to reconstituted enzyme was considered achieved when no further intensity was gained at the 468 nm absorption upon addition of more aliquot of PLP. The precise concentration of PLP is determined by using the extinction coefficient 5.39 $mM^{-1}cm^{-1}$ measured on the purchased PLP sample dissolved

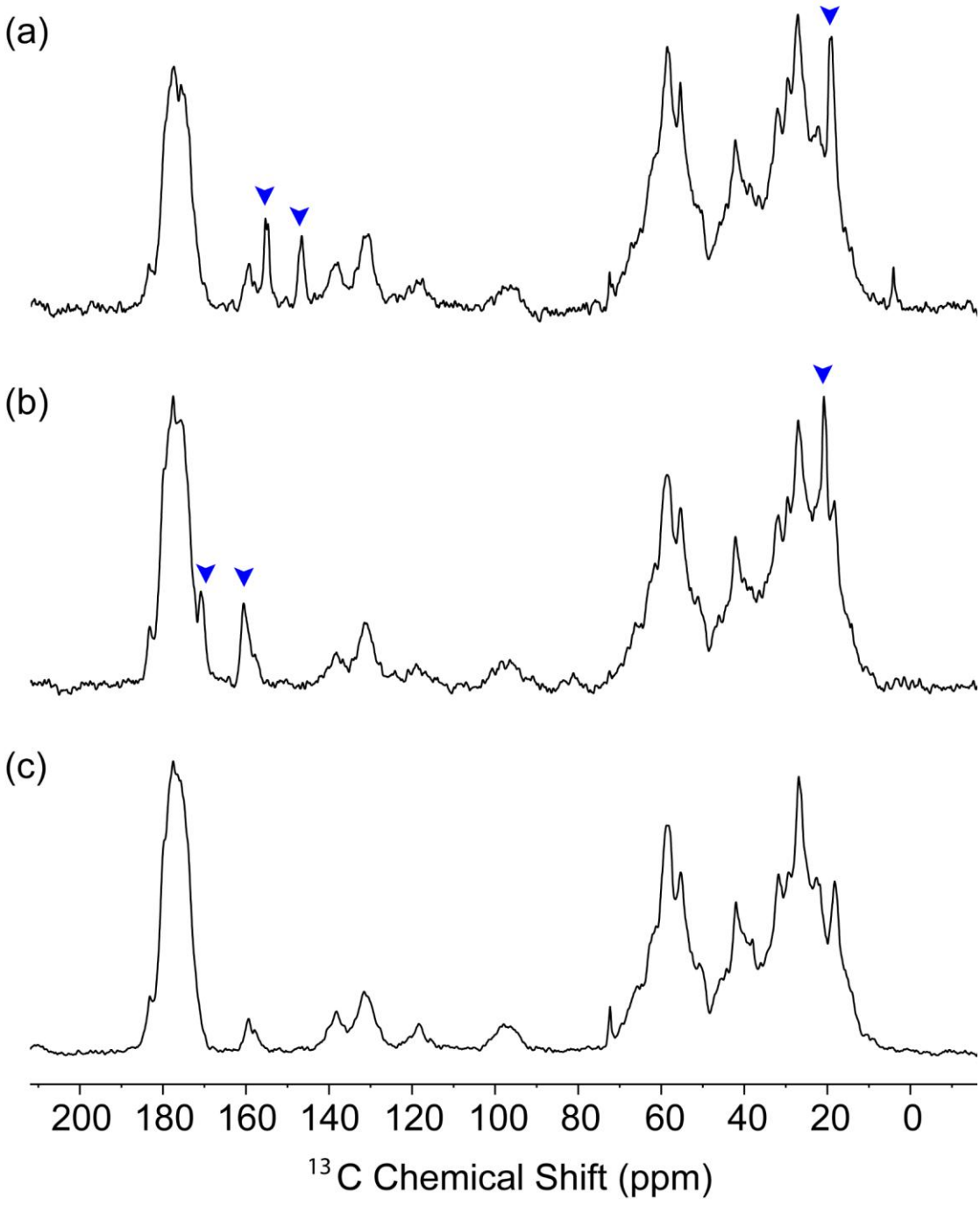

Figure 3.4. ^{13}C CP-MAS experiments of TS. From bottom to top: (c) natural abundance (NA) TS with extensive number of scans (20480 transients coadded), in the form of E(Ain). (b) TS/2,2',3-$^{13}C_3$;^{15}N-PLP E(Ain), with 10240 transients coadded. (a) TS/2,2',3-$^{13}C_3$;^{15}N-PLP 2-AP quinonoid, $E(Q)_{2AP}$, with 8192 transients coadded. The peaks corresponding to ^{13}C enriched sites on PLP is marked by blue arrows.

in pH 7.8 50 mM Cs-bicine buffer, as measured at 390 nm using UV/vis spectroscopy. The calibration curve is shown in Fig. 3.3.

Solid-state NMR experiments were then performed on the reconstituted TS/2,2',3-$^{13}C_3$,^{15}N-PLP sample. The ^{13}C spectra are shown in Fig. 3.4. In comparison with the spectrum of TS with natural abundance PLP (Fig. 3.4 (c)), three extra chemical can be observed for E(Ain) in Fig. 3.4 (b), corresponding to the three ^{13}C labeling sites on PLP. The addition of 2-AP and L-serine into the rotor caused the conversion of E(Ain) into the stable $E(Q)_{2AP}$. And the three labeling sites again were distinguished from the natural

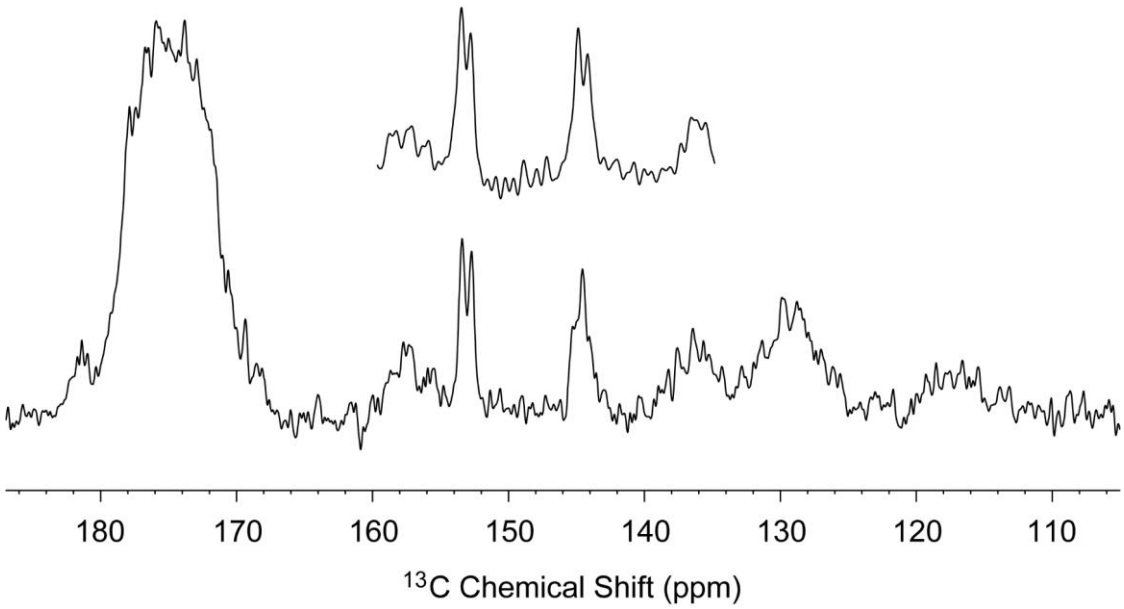

Figure 3.5. Comparison of LOW-BASHD filtered CP-MAS ^{13}C spectrum with the non-filtered experiment of TS/2,2',3-$^{13}C_3$; ^{15}N-PLP $E(Q)_{2AP}$. The top smaller sized spectrum is LOW-BASHD filtered, while the lower larger spectrum is the normal CP-MAS spectrum. The down field peak was identified as C3 because of the only *J*-coupling with C2. The other upfield peak was identified as C2 due to the *J*-couplings wth both C3 and C2'.

abundance background in Fig. 3.4 (a). Chemical shifts of 2, 2', and 3 positions carbons of the PLP were identified as 158.6 ppm, 18.5 ppm, and 168.7 ppm respectively in E(Ain). And in $E(Q)_{2AP}$, the three sites were observed as 144.6 ppm, 16.9 ppm, and 153.1 ppm respectively in the same order. The aromatic C_2 and C_3 of PLP ring were distinguished from each other by using LOW BASHD as shown in Fig. 3.5. The decoupling of $C_{2'}$ resulted in the removal of the *J*-coupling splitting between C_2 and $C_{2'}$ in the LOW-BASHD filtered spectrum, while not affecting C_3. The upper field peak did condense from a triplet

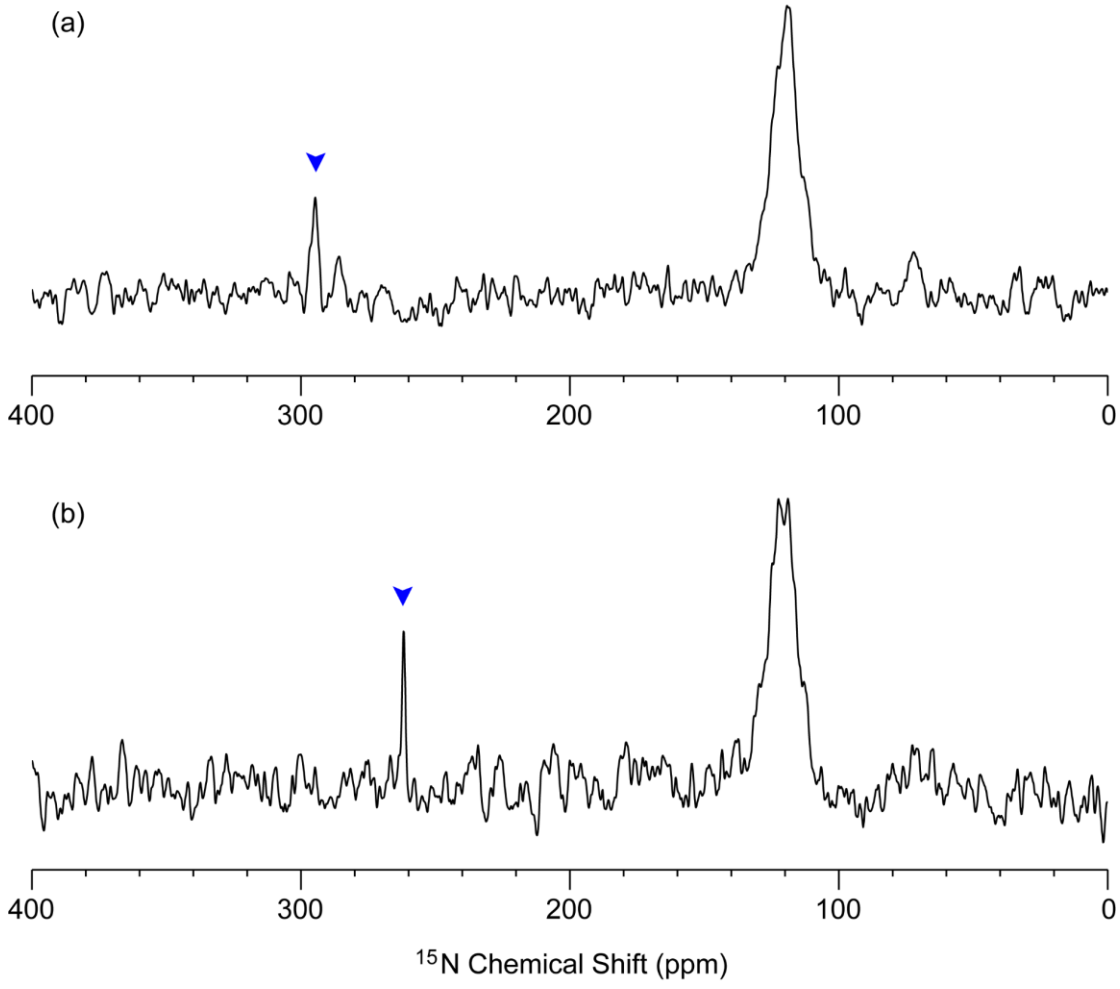

Figure 3.6. ^{15}N CP-MAS experiments of TS /2,2',3-$^{13}C_3$;^{15}N-PLP (a) E(Ain). (b) 2-AP quinonoid.

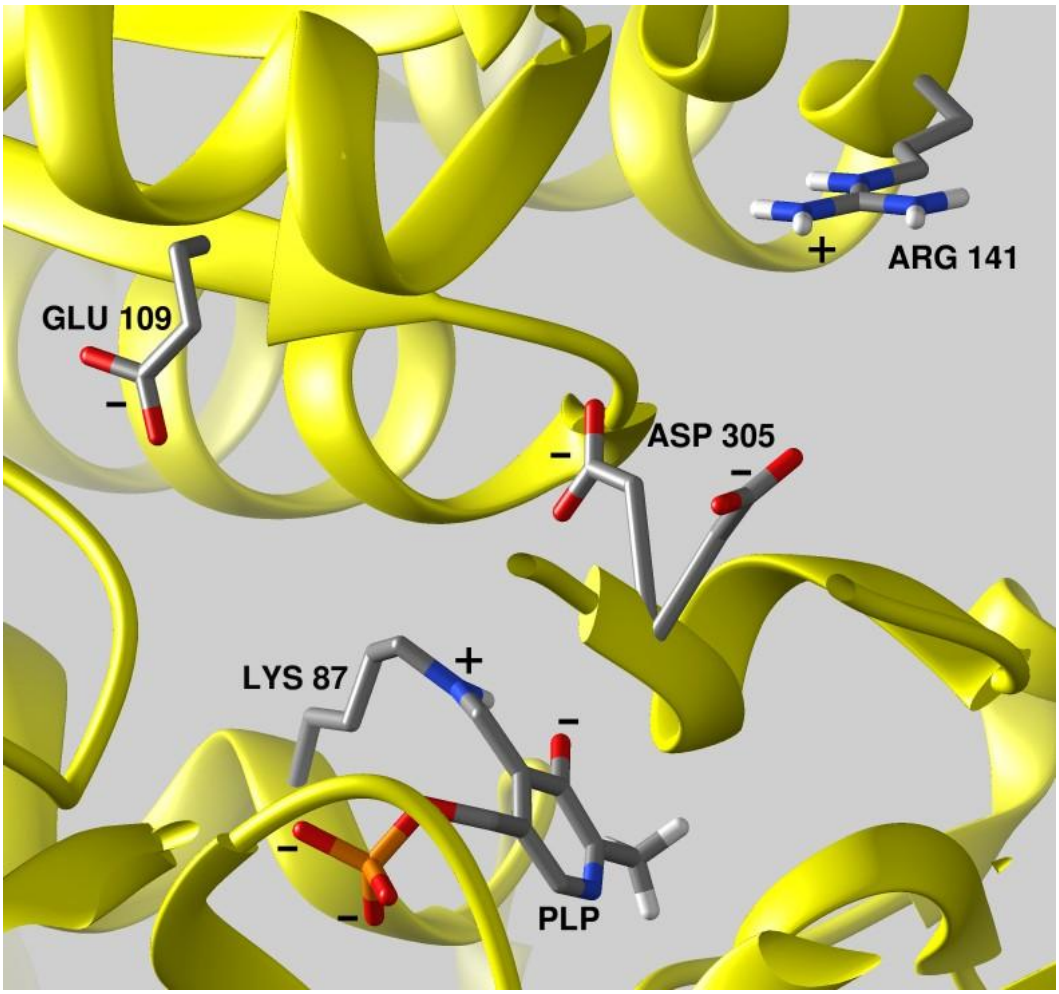

Figure 3.7. The structure of the β-active site intermediate E(Ain) investigated in this work (PDBID 4HT3).

into a doublet by LOW-BASHD. The other peak was not affected, and remained a doublet. In this way, C_3 was identified at lower field, and C_2 upper field.

With the TS/2,2',3-^{13}C3;^{15}N-PLP been identified and confirmed exchanged into TS active site, ^{15}N CP-MAS experiments were acquired on E(Ain) and E(Q)$_{2AP}$ (Fig. 3.6) to explore the protonation states of the two intermediates. The pyridine nitrogen (N1) showed chemical shift at 294.7 ppm for E(Ain), Fig. 3.6(a), indicating the position been deprotonated.[31] In the E(Q)$_{2AP}$, the pyridine nitrogen chemical shift moved upfield to 261.8

ppm, showing stronger hydrogen-bonding interaction with βSer377, while remaining deprotonated. The results are in agreement with the protonated Schiff base (PSB) hypothesis at the β-site.[32] The PSB mechanism suggests that in E(Ain), the $C_{4'}$ is the preferred location for nucleophilic attack during transamination reaction.[1] The transamination step exchanges the PLP Schiff base linkage from to the protein βLys87 to the substrate. The positively charged Schiff base nitrogen in this step can be stabilized by the PLP π system. This is supported also by UV/vis optical spectroscopy, because the 412

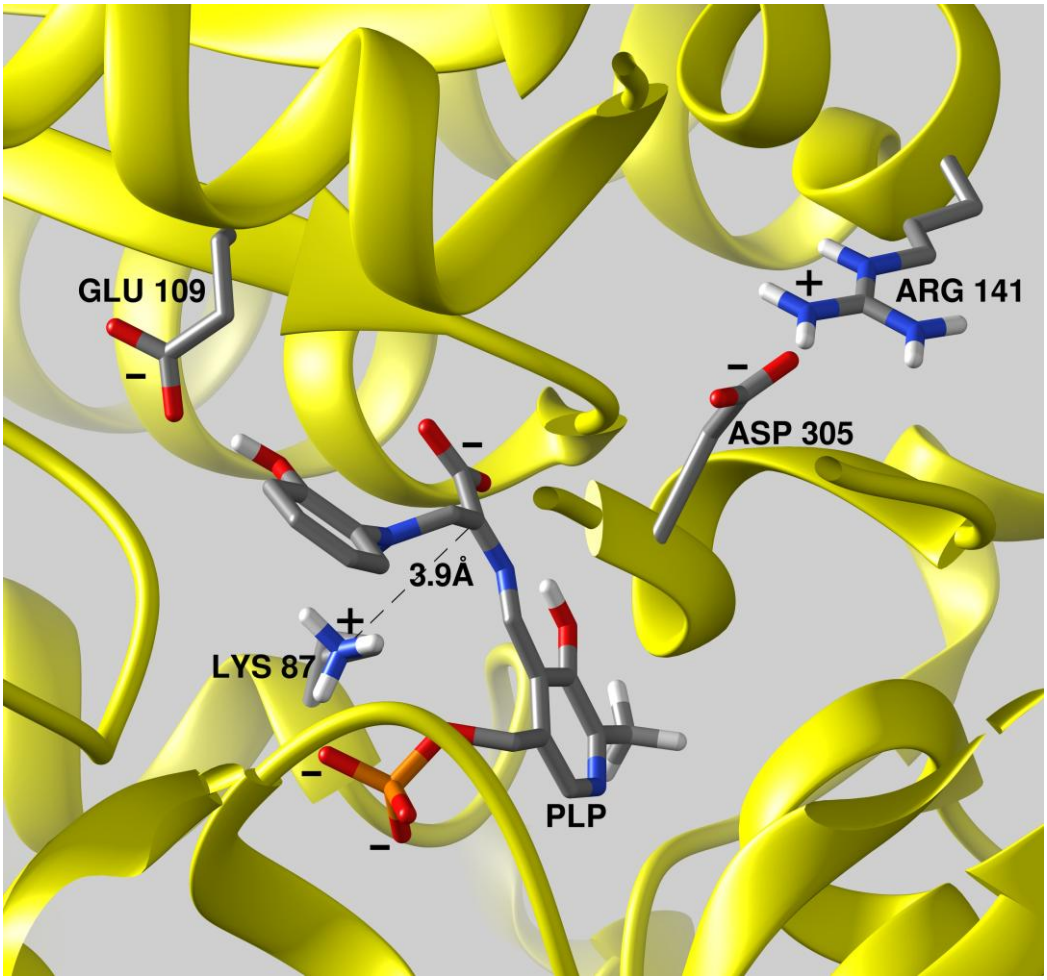

Figure 3.8. The structure of the β-active site intermediate $E(Q)_{2AP}$ investigated in this work (PDBID 4HPJ).

nm absorption maxima of E(Ain) appeared to be lower than in most PLP enzymes[32] (ranging from 420 nm to 430 nm). The observed UV/vis absorption maxima is independent of pH over the range 5.8 – 10.4, and indicating a single ionic form of the E(Ain) β-site.[8,33,34] The deprotonated pyridine nitrogen behaves as an electron sink, which provides an alternative resonance structure for the E(Ain), resulting in stabilized E(Ain) structure. The neutral deprotonated nitrogen is stabilized by βSer377. Based on XRD crystal structures[13], chemical shifts measured in hand[14], the E(Ain) structure, with its associated protonation states are shown in Fig. 3.7. For $E(Q)_{2AP}$, a complete description of the protonation states would still need efforts on chemical shifts introduced by ^{13}C,^{15}N-labeled L-serine, or chemical shifts of the hydroxyl group by using ^{17}O labeled PLP. Although based on XRD, and preliminary SSNMR studies[1,14], the protonation states are likely represented as in Fig 3.8 for $E(Q)_{2AP}$. The βLys87 is protonated in this intermediate, which helps stabilize the negatively charged L-serine C^{α}. In the case of a real reaction, which results in the $E(Q_2)$ intermediate using indole and L-serine, the stabilized C^{α} of L-serine substrate will withdraw a proton from the positively charged βLys87, and also initiate the formation of positively charged Schiff base nitrogen. The positive charge on nitrogen would finally induce the detachment of the synthesized L-tryptophan, and the formation of E(Ain), finishing the catalytic cycle.

3.4 Conclusion

Atomic-resolution within the enzyme active site provided by solid-state NMR contributes to a precise description of protonation states within TS β-subunit, with TS $\alpha_2\beta_2$ complex in the microcrystal form. Although the global assignment is not achievable for the

144 kDa enzyme macromolecule, the labeling of interesting sites introduced by coenzyme or substrate is still effective in estimating the chemical environment around the labeled sites. The coenzyme exchange procedure adapted in this work made possible the measurements of chemical shifts directly on PLP, producing chemical shifts of pyridine nitrogen, and three PLP carbons. The procedure will also be useful in the future for introducing in ^{17}O or $C_{4'}$ labelings into the active site. With chemical shifts in proximity to related protons partially or all identified in the future after this work, the chemical environment within the TS β-subunit can be precisely determined. In this way, SSNMR, in complementary to X-ray crystallography and optical spectroscopy, demonstrates its power of sensitivity to local chemical environment, and the great potential in broader application in crystal structure interpretation.

3.5 References

(1) Lai, J.; Niks, D.; Wang, Y.; Domratcheva, T.; Barends, T. R. M.; Schwarz, F.; Olsen, R. a; Elliott, D. W.; Fatmi, M. Q.; Chang, C. a; Schlichting, I.; Dunn, M. F.; Mueller, L. J. *J. Am. Chem. Soc.* **2011**, *133*, 4.

(2) Dunn, M. F.; Niks, D.; Ngo, H.; Barends, T. R. M.; Schlichting, I. *Trends Biochem. Sci.* **2008**, *33*, 254.

(3) Miles, E.; Bauerle, R.; Ahmed, S. *Methods Enzymol.* **1987**, *142*, 398.

(4) Miles, E. W. In *Advances in Enzymology and Related Areas of Molecular Biology*; Meister, A., Ed.; John Wiley & Sons, Inc., 1979; pp. 127–186.

(5) Lane, a N.; Kirschner, K. *Eur. J. Biochem.* **1983**, *129*, 571.

(6) Yanofsky, C.; Crawford, I. P. In *The Enzyme*; Academic Press, 1972.

(7) Toney, M. D. *Biochim. Biophys. Acta* **2011**, *1814*, 1405.

(8) Metzler, D. E.; Ikawa, M.; Snell, E. E. *J. Am. Chem. Soc.* **1954**, *76*, 648.

(9) Kappes, B.; Tews, I.; Binter, A.; Macheroux, P. *Biochim. Biophys. Acta* **2011**, *1814*, 1567.

(10) Romo, A. J.; Liu, H. *Biochim. Biophys. Acta* **2011**, *1814*, 1534.

(11) WB_Dempsey_Synthesis of PLP_book.pdf.

(12) Milest, E. W.; Kawasaki, H.; Ahmedv, S. A.; Morita, H. *J. Biol. Chem.* **1989**, *264*, 6280.

(13) Niks, D.; Hilario, E.; Dierkers, A. T.; Ngo, H.; Borchardt, D.; Neubauer, T. J.; Fan, L.; Mueller, L. J.; Dunn, M. F. *Biochemistry* **2013**.

(14) Caulkins, B. G.; Bastin, B.; Yang, C.; Neubauer, T. J.; Young, R. P.; Hilario, E.; Huang, Y.-M. M.; Chang, C.-E. a; Fan, L.; Dunn, M. F.; Marsella, M. J.; Mueller, L. J. *J. Am. Chem. Soc.* **2014**, *136*, 12824.

(15) Crugeiras, J.; Rios, A.; Riveiros, E.; Richard, J. P. *J. Am. Chem. Soc.* **2011**, *133*, 3173.

(16) Major, D. T.; Gao, J. *J. Am. Chem. Soc.* **2006**, *128*, 16345.

(17) Major, D. T.; Nam, K.; Gao, J. *J. Am. Chem. Soc.* **2006**, *128*, 8114.

(18) Renault, M.; Cukkemane, A.; Baldus, M. *Angew. Chemie - Int. Ed.* **2010**, *49*, 8346.

(19) Ye, T.; Chen, L.; Niks, D.; Kaiser, J. M.; Lai, J.; Rienstra, C. M.; Dunn, M. F.; Mueller, L. J. *Phys. Chem. Chem. Phys.* **2009**, *11*, 6875.

(20) Ferrari, D.; Niks, D.; Yang, L.-H.; Miles, E. W.; Dunn, M. F. *Biochemistry* **2003**, *42*, 7807.

(21) Yang, L.; Ahmed, S. A.; Miles, E. W. **1996**, *136*, 126.

(22) Creighton, T. E.; Yanofsky, C. *J. Biol. Chem.* **1965**, *241*, 980.

(23) Remeta, D. P.; Miles, E. W.; Ginsburg, A. *Pure Appl. Chem.* **1995**, *67*, 1859.

(24) Bartholmes, P.; Teuscher, B. *Eur. J. Biochem.* **1979**, *95*, 323.

(25) Miles, E. W.; Moriguchi, M. *J. Biol. Chem.* **1977**, *252*, 6594.

(26) Hartmann, S.; Hahn, E. *Phys. Rev.* **1962**, *128*, 2042.

(27) Fung, B. M.; Khitrin, a K.; Ermolaev, K. *J. Magn. Reson.* **2000**, *142*, 97.

(28) Bertini, I.; Emsley, L.; Lelli, M.; Luchinat, C.; Mao, J.; Pintacuda, G. **2010**, 5558.

(29) Morcombe, C. R.; Zilm, K. W. *J. Magn. Reson.* **2003**, *162*, 479.

(30) Struppe, J. O.; Yang, C.; Wang, Y.; Hernandez, R. V; Shamansky, L. M.; Mueller, L. J. *J. Magn. Reson.* **2013**, *236*, 89.

(31) Sharif, S.; Huot, M. C.; Tolstoy, P. M.; Toney, M. D.; Jonsson, K. H. M.; Limbach, H. **2007**, 3869.

(32) Peracchi, A.; Bettati, S.; Mozzarelli, A.; Rossi, G. L.; Miles, E. W.; Dunn, M. F. *Biochemistry* **1996**, *35*, 1872.

(33) Heinert, D.; Martell, A. E. *J. Am. Chem. Soc.* **1963**, *85*, 183.

(34) Christensen, H. N. *J. Am. Chem. Soc.* **1958**, *80*, 99.

Chapter 4

Development of Proton Detection Based Solid-State NMR Experiments at 50 kHz MAS for Biological Macromolecules

4.1 Introduction

In recent years, advancements in hardware design have made available SSNMR experiments on protein samples at very fast magic angle spinning (MAS) conditions.[1–3] With dipolar interactions being partially averaged by MAS, proton detections are possible nowadays. Proton detection take advantage of the higher gyromagnetic ratio intrinsic to ^{1}H, as compared to ^{13}C or ^{15}N, giving higher sensitivity. The dipolar couplings to ^{1}H can further be circumvented by using ^{1}H spin dilution via perdeuteration during protein expression, with back-exchange in H_2O to bring back ^{1}H at exchangeable sites. The high resolution and sensitivity offered by proton detection and its associated correlation method provide us a promising approach for handling large enzymatic systems, like the tryptophan synthase (144 kDa). However, before being overly ambitious to directly apply multidimensional correlation SSNMR experiments on the tryptophan synthase, RF pulse sequence techniques were examined at 50 kHz using the β1 immunoglobulin binding domain of protein G (GB1). GB1 is a 56-residue protein serving as an excellent standard for setting up SSNMR experiments. The protein is of small size (around 8 kDa), and at room temperature all 56 residues of GB1 in microcrystalline form were already assigned in previous works.[3–6] Also the crystal polymorphism of GB1 was extensively explored with different precipitation procedures.[7] SSNMR Experiments optimized on GB1 can provide us a qualitative estimate of the best resolution and sensitivity one should expect when

moving to a larger protein system. As the protein size increases, the detectable signal density of a specific site within a protein would decrease, resulting in lowered sensitivity. Because of that, multidimensional techniques have to work really well on GB1, before being even applicable to any assignment tasks for tryptophan synthase. Besides studying CP conditions at both low power and high power, the effect of deuteration was also studied by optimizing (HC)N DCP experiments on both U-^{13}C-^{15}N-labeled GB1 and U-^{2}H-^{13}C-^{15}N-labeled back-exchanged GB1 samples at varied CP conditions. Transfer efficiency was quantified by comparison with the (H)N CP experiments. The efficiency measured at these conditions provided us reference for future development of 3D correlation experiments.

In addition to setting experiments up with protein samples, U-^{13}C-^{15}N-labeled alanine was used for estimation of refocused transverse relaxation time (T_2') at different MAS rates ranging from 20 kHz to 50 kHz. In solid-state NMR, the apparent linewidth T_2 is independent of the size of a protein, making NMR in solid state potentially very powerful at proteins of larger sizes. However, without the frequent tumbling in the liquid state, dipolar interactions contribute to severe homogeneous linebroadening (with linewidth quantified as $1/2\pi T_2'$), the effect of which has to be quenched by MAS in combination with effective decoupling sequences. The length of T_2' on ^{13}C and ^{15}N resonances are largely dependent on the effectiveness of ^{1}H heteronuclear decoupling performance. The measurements of T_2' provide a quantitative description of homogeneous linebroadening induced by ^{1}H dipolar coupling network, with interference also modulated by MAS. A better decoupling performance is treated here as longer T_2' when measured using spin-echo experiment detecting on ^{13}C or ^{15}N.[8] The XiX (X-inverse-X) ^{1}H decoupling sequence[9] was

used here, because of its easy optimization and better performance at higher spinning speeds. The XiX sequence is a continuous replication of two nested pulses of equal width (t_p) and opposite phase. The optimum pulse length t_p is constant at different MAS rate,[10] with the decoupling power being the only variable for setting up the sequence. The monitoring of the decoupling performance on different carbons at different MAS with varied decoupling powers gave us information in understanding the interaction of MAS and dipolar couplings, and how the RF power mediates the interactions. The measurements of T_2' at various conditions are useful in determining the evolution time for the indirect dimensions in designing multidimensional correlation methods, and can help decide the possibility of polarization transfer through *J*-couplings.[11] The small U-^{13}C-^{15}N-labeled amino acid L-alanine was monitored as simplified models for C^{α}, C' and C^{β} within a protein backbone. The C^{α} is the most similar to within a protein backbone of the three, with both connections to N and C'. The modeling of C' and C^{β} are more rough estimations. Because, in reality, apart from the C' terminal of a polypeptide, C' would always connect with the nitrogen of the adjacent amino acid. For C^{β}, it can connect with C^{γ}, hydroxyl groups, or sulfhydryl group, or not even exist (in the case of glycine). And in cases when C^{β} presents, the variations of amino acids can result in very different C^{β}'s. Although care should be taken when considering the results performed on the L-alanine sample, the mapping of T_2' gives us the general trend of T_2' when changing the decoupling power and spinning speed.

One application of proton detected correlation experiments on a protein sample is demonstrated here for the Pf1 bacteriophage. Pf1 bacteriophage is a filament with a sheath formed of thousand copies of coat protein monomer (46 residues), enclosing the DNA in

the center. The structure of the coat protein in Pf1 bacteriophage has been revealed in previous works.[12,13] The proton detected $^{1}H/^{15}N$ correlation experiment was implemented on the sample of highly concentrated noncrystalline Pf1 bacteriophage particles. The study provides a model for more complex systems of membrane proteins. The bacteriophage samples were also deuterated and back-exchanged in H_2O. The deuteration helped isolate ^{1}H-^{15}N spin pairs. And since Pf1 filaments were aligned during sample rotation along the rotor axis, the system enabled the measurements of dipolar couplings between ^{1}H-^{15}N spin pairs by variable contact time (VCT) during CP. The measurements can help resolve overlapping chemical shifts by the orientation of NH bonds relative to the rotor axis.

4.2 Experimental Section

4.2.1 Measurements of Refocused Transverse Dephasing Time

The correlations of refocused transverse dephasing time (T_2') and decoupling power at various MAS rate were mapped using the XiX (X-inverse-X) heteronuclear ^{1}H decoupling scheme[9] on the U-^{13}C-^{15}N-labeled L-alanine.

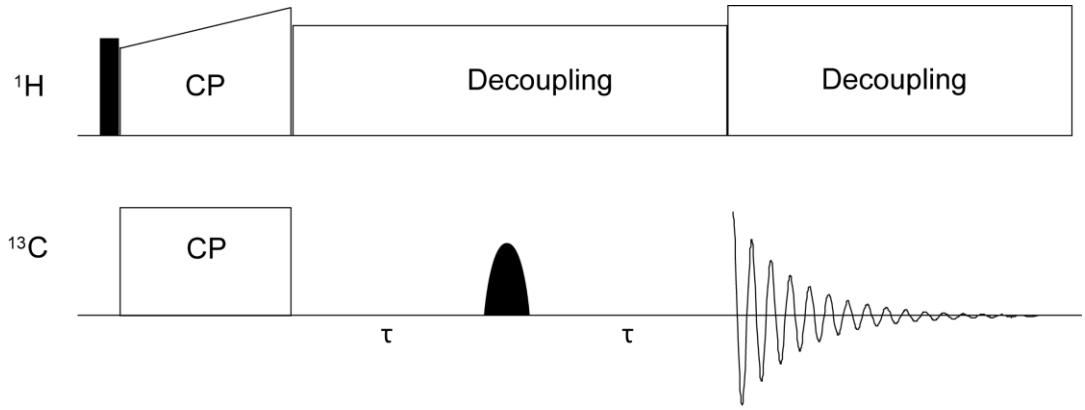

Figure 4.1. Schematic representation of the pulse sequence for transverse dephasing time (T_2') measurements. The filled rectangle represents 90° pulse on ^{1}H channel. And the filed bell shape represents selective 180° π pulse on ^{13}C channel.

At MAS rates of 20 kHz, 25 kHz, and 27.5 kHz, experiments were performed at 9.4 T (400.37 MHz ^{1}H, 100.69 MHz ^{13}C) on a Bruker AVIII spectrometer equipped with a 2.5 mm MAS probe. Cross Polarization (CP) from ^{1}H to ^{13}C was accomplished at a ^{1}H spin-lock field of 3.5 times the spinning speed (tangent ramped ± 10 kHz) and ^{13}C spin-lock field of 2.5 times the spinning speed. The intensities of C^{α}, C^{β}, and C' were monitored respectively after the echo τ-π- τ sequence (Fig. 4.1), with the offset of the selective π pulse at the center of the interesting carbon in each case. At each MAS rate, before studying the decoupling intensities, the pulse length (t_p) for XiX decoupling was scanned from 1 μs to 200 μs (Fig. 4.3) on C^{α} with a total τ-π- τ length of 10 ms, and decoupling power at 4.4 times the spinning speed in each case (87.5 kHz, 109.2 kHz, and 120.2 kHz). The experiments confirmed that t_p maximized at both the $1.85\tau_r$ ('τ_r' represents one rotor period) and $2.85\tau_r$ optimum conditions as previously described.[14] Then the decoupling strengths during the τ-π- τ period were scanned from 0 kHz to 160 kHz for the 1 ms τ length (2 ms total echo period) at the $1.85\tau_r$ condition. The scan was achieved with 587 different decoupling strength data points at 20 kHz, 617 data points at 25 kHz, and 297 data points at 27.5 kHz. After that, at each MAS rate, τ periods of 2 ms, 4 ms, 6 ms, 8 ms, and 10 ms were explored with varied XiX decoupling intensities respectively in each case of C^{α}, C^{β}, and C'. Although for these longer delays, only six different intensities were recorded while holding the delay periods constant for each τ. The intensities recorded at longer τ's at each spinning speed for each carbon were used to correlate intensity and T_2'.

For MAS rates of 30 kHz, 40 kHz, and 50 kHz, similar experiments were performed at 14.1 T (600.13 MHz ^{1}H, 150.92 MHz) on a Bruker AV600 spectrometer equipped with

a 1.3 mm MAS probe. CP from ^{1}H to ^{13}C was accomplished at a ^{1}H spin-lock field of 2.5 times the spinning speed (tangent ramped ± 10 kHz) and ^{13}C spin-lock field of 1.5 times the spinning speed respectively at each MAS rate. Correlations of *T2'* and decoupling strength during the τ-π- τ echo period were studied with XiX decoupling at the $t_p=2.85\tau_r$ condition. The decoupling strengths were varied from 0 kHz to 160 kHz, with the echo durations τ held at 1 ms. And the total number of decoupling strength values are 514 at 30 kHz, 554 at 40 kHz, and 514 at 30 kHz. Then τ periods of 2 ms, 4 ms, 6 ms, 8 ms, and 10 ms were also explored with far fewer data points (6 values). These experiments estimates the correlation of *T2'* and intensity. And the correlation is used to map the T_2' landscape using the 1 ms τ data. Only C^{α} and C' were monitored at these three higher spinning speed, since they are more useful sites, considering the similarity with protein backbones.

4.2.2 VC-CP Experiments on Pf1 Bacteriophage

Solid-state NMR experiments were performed at 14.1 T (600.01 MHz ^{1}H, 60.8 MHz ^{15}N) on a Bruker AV600 spectrometer equipped with a triple resonance 1.3 mm MAS probe. The sample spinning rate was controlled to 50 kHz (±2 Hz). The probe temperature was lowered to 14 °C using dry-air cooling gas at -36 °C and a flow rate of 800 l/h; the actual effective sample temperature based on calibration with KBr[15] was estimated to be 29 °C due to frictional heating.

Two-dimensional proton-detected ^{15}N chemical shift/^{1}H chemical shift correlation spectra and three-dimensional proton-detected ^{1}H–^{15}N heteronuclear dipolar coupling/^{15}N chemical shift/^{1}H chemical shift correlation spectra were acquired using the pulse sequence diagrammed in Fig. 4.2, which was adapted from Marchetti et al.[16] to include variable contact time (VCT) cross- polarization (CP) in the manner of Paluch et al.[17]. In these sequences, hard $\pi/2$ pulses were used with nutation frequencies of 83 kHz and 50 kHz for ^{1}H and ^{15}N, respectively. CP was achieved using constant amplitude RF spin-lock pulses with nutation frequencies of 125 kHz for ^{1}H and 75 kHz for ^{15}N (+1 match condition).[18] The contact time was 2 ms for constant-time CP transfers, and varied between 60 μs and 3840 μs during VCT experiments. XiX ^{1}H decoupling,[19] with a nutation frequency of 125 kHz and decoupling pulse width of 57 μs (2.85τ), was applied during evolution on ^{15}N. MISSISSIPPI water suppression[5] (without homospoil pulses) was implemented during τ_{ws}

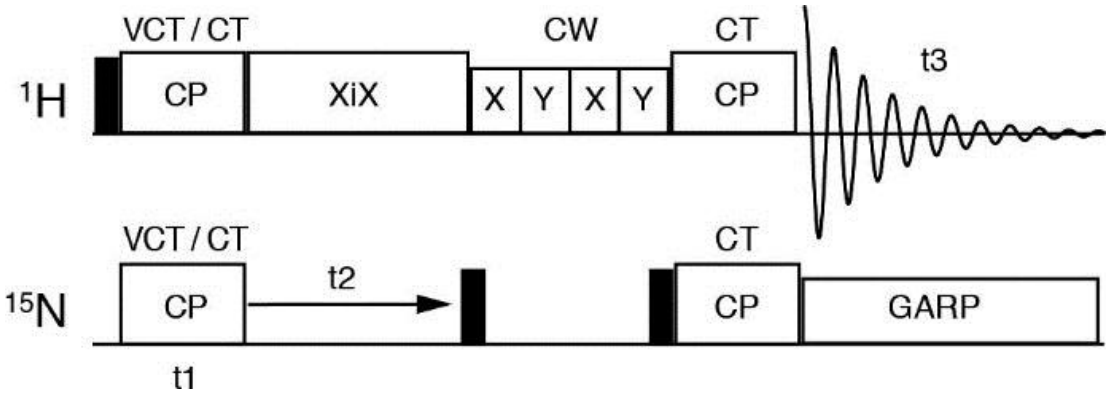

Figure 4.2. Diagram of the pulse sequence used in the correlation experiments. The two-dimensional experiment utilized constant time (CT) cross polarization (CP) for both magnetization transfer steps. The three-dimensional experiment utilized a variable contact time (VCT) during the first CP. Other aspects are the same for both experiments. Narrow filled rectangles indicated 90° pulses, and blank rectangles are noted with text above or inside.

on the proton channel using four 75 ms, 9.6 kHz RF saturation pulses. ^{15}N GARP decoupling with irradiation of 22.6 kHz was applied during ^{1}H acquisition.

Correlation spectra were acquired using 64 complex-valued time-domain points with a dwell of 250 μs (spectral width 4 kHz, total data acquisition time 16 ms) in the indirect nitrogen shift dimension, and 256 complex time-domain points with a dwell of 40 μs (spectral width 25 kHz, total data acquisition time 10.2 ms) in the directly detected proton shift dimension. For three-dimensional variable-contact-time experiments, 64 real-valued time-domain points were acquired with an increment of 60 μs. 128 scans per t1 point were averaged for the two-dimensional ^{15}N chemical shift–^{1}H chemical shift correlation experiments; 4 scans per transient were co-added for the three-dimensional correlation experiments. The relaxation delay for all experiments was 2.5 s. The data were zero filled to yield a 1024 × 1024 data matrix for two-dimensional and a 1024 × 128 × 128 data matrix for three-dimensional experiments. Polynomial correction and solvent filter[20] window functions were used in the proton chemical shift and dipolar dimensions, respectively, before the application of a 30° phase shifted sine bell function and an exponential filter (30–60 Hz). The NMR data were processed using the program NMRPipe/NMR-Draw.[21]

4.2.3 2D Correlation Experiments on GB1

U-^{2}H-^{13}C-^{15}N-labeled GB1 and U-^{13}C-^{15}N-labeled GB1 were expressed and purified as previously described.[22] For the deuterated protein, during purification, buffer was prepared using H_2O, making the exchangeable deuterons replaced by protons.[8] GB1 nanocrystalline samples were prepared by using the natural abundance methyl-2,4-

pentanediol (MPD) and 2-propanol (IPA) in a 2:1 ratio as precipitants. The precipitants were added into the protein stock solution stepwise, until total volume amount of four times the protein solution.[7]

Two-dimensional proton-detected $^{15}N/^{1}H$ correlation spectra were also performed at 14.1 T (600.01 MHz ^{1}H, 60.8 MHz ^{15}N) on a Bruker AV600 spectrometer equipped with a triple resonance 1.3 mm MAS probe, with sample spinning rate of 50 kHz (±2 kHz). . General setup is the same as previously described for Pf1 bacteriophage, with a different CP condition. The CP from ^{1}H to ^{15}N was accomplished at a ^{1}H spin-lock field of 2/3 times the spinning speed (tangent ramped ± 2 kHz) and ^{15}N spin-lock field of 1/3 times the spinning speed. The same low power CP condition was used from ^{15}N to ^{1}H for proton detection. The setup of double CP (DCP) (HC)N experiments were performed and optimized by varying the CP powers and contact times. The transfer efficiency was quantified by comparison with the CP (H)N experiments. The experiments set the ground for the setup of further three-dimensional proton-detected (H)CNH correlation experiments at 50 kHz MAS on the spectrometer.

4.3 Results and Discussion

4.3.1 Refocused Transverse Dephasing Time at Different MAS Rates

Refocused transverse dephasing time (T_2') was measured out at 20 kHz, 25 kHz, 27.5 kHz MAS using a 2.5 mm rotor. And at 30 kHz, 40 kHz, and 50 kHz MAS, T_2' was measured using a 1.3 mm rotor. The measurement scheme is shown in Fig. 4.1. Before the intensities measurements to derive T_2', XiX optimum pulse length (t_p) conditions were first examined. The test maintained decoupling during acquisition to be also XiX, with its

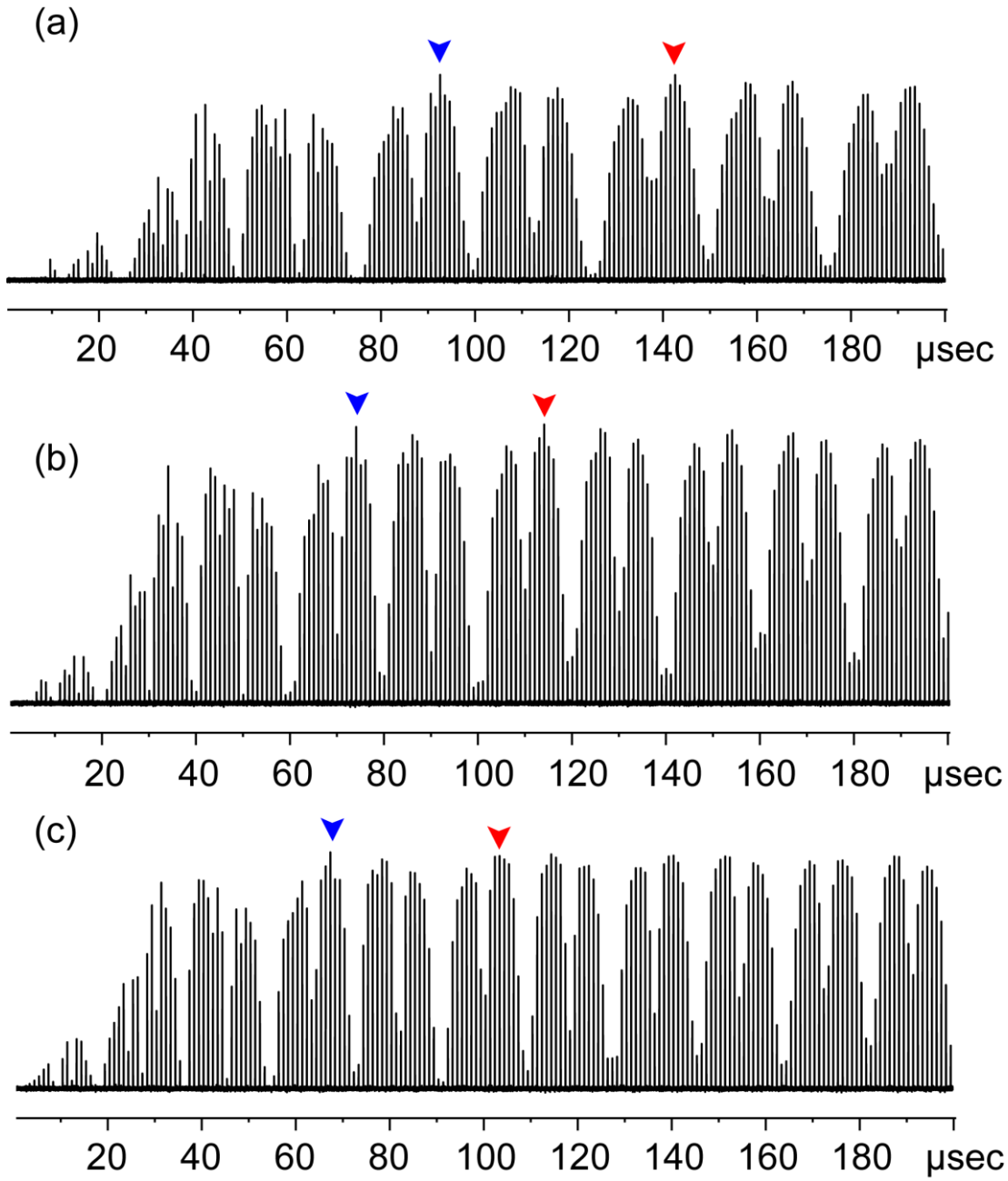

Figure 4.3. Intensities recorded on C^{α} of U-^{13}C-^{15}N-labeled L-alanine, with XiX decoupling pulse length varied from 1 μs to 200 μs during the τ-π-τ spin echo period. The spin echo total length was held at 10 ms The sample spinning speed was (a) 20 kHz, (b) 25 kHz, and (c) 27.5 kHz, using a 2.5 mm rotor. Blue arrows were pointed at the theoretical $1.85\tau_r$ conditions, and red arrows were pointed at the theoretical $2.85\tau_r$ conditions[14] for corresponding spinning speeds.

theoretical optimum condition of $t_p = 1.85\tau_r$, and decoupling power corresponding to 90 kHz, while during the spin echo period, decoupling strength was held at 4.4 times the spinning, and t_p was scanned from 1 μs to 200 μs. The result is shown in Figure 4.3. The intensities recorded after spin echo periods dictate the homogeneous linebroadening effect, as reflected in intensities. In general, a higher T_2' corresponds to a higher intensity. Since the longer the T_2' is, the stronger the intensity during the refocused echo period. The intensities measured at varied t_p's , during echo period, as shown in Fig 4.3, follow the general trend for the scan of t_p during the direct acquisition of a simple equivalent CP experiment.[9,14] The t_p's at the theoretical optimum $1.85\tau_r$ and $2.85\tau_r$ conditions did show intensities among the highest during the spin echo experiments, corresponding to longer T_2's. And since decoupling powers were held at 4.4 times the spinning speeds during the echo period, decoupling powers were lower at 20 kHz, and higher at the 25 kHz and 27.5 kHz MAS rates. And the difference in the highest peak intensities shows the same trend when comparing Fig. 4.3(a) to Fig 4.3(b) and (c), with lower intensities at 20 kHz MAS, and higher intensities at the 25 kHz and 27.5 kHz MAS rates. In sum the intensities of different t_p's behave the same as described in previous theoretical works.[14,23] For this work on U-^{13}C-^{15}N labeled L-alanine, at lower spinning speeds (from 20 kHz to 27.5 kHz), the $1.85\tau_r$ condition was used, while at higher spinning speeds (from 30 kHz to 50 kHz) the $2.85\tau_r$ condition was used for the decoupling power studies.

The T_2's at different decoupling powers and spinning speeds were estimated from scans of decoupling powers at τ of 1 ms for refocused echo τ-π-τ period, with the correlation between intensities and T_2' derived from a fitting of intensities at different

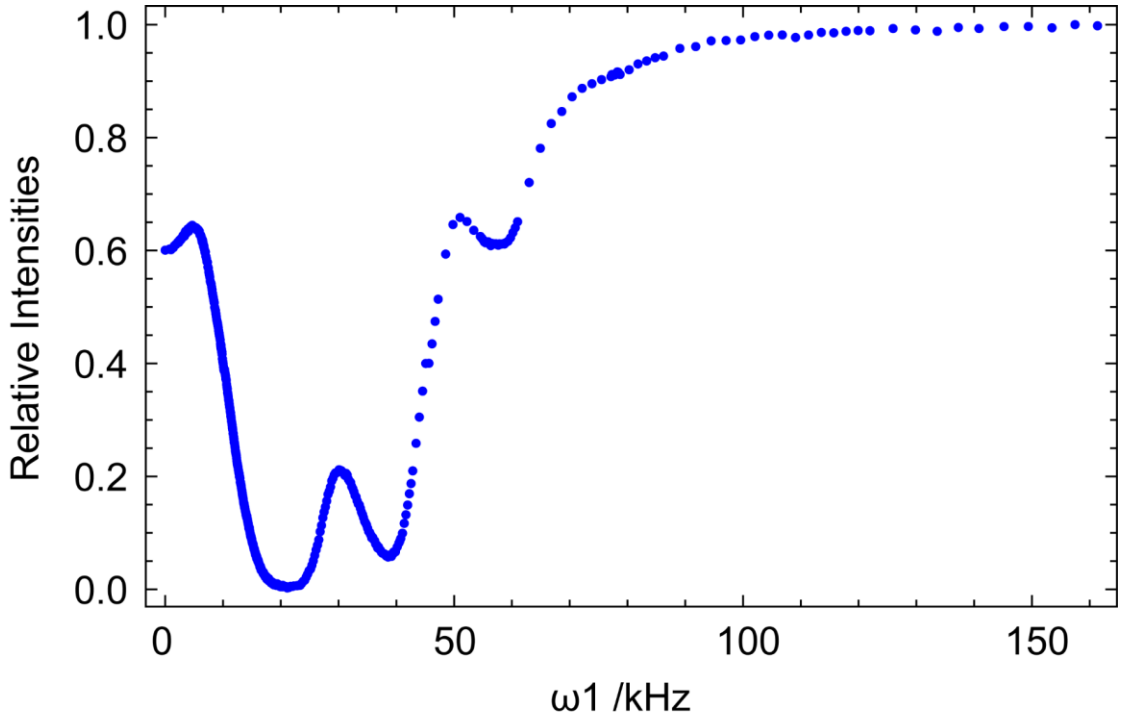

Figure 4.4. Intensities recorded on C' of U-^{13}C-^{15}N-labeled L-alanine, with decoupling power (ω1) during the echo period varied from 0 kHz to 160 kHz. The sample spinning speed was 20 kHz, using a 2.5 mm rotor. XiX decoupling was used, with t_p = 1.85 t_τ condition. C' was not directly bonded to ^{1}H in L-alanine, resulting in the almost flat plateau above 3 times the spinning speed (or above 60 kHz).

refocusing lengths of a constant decoupling power. Take C' in U-^{13}C-^{15}N-labeled L-alanine at 20 kHz as an example: First the scan at τ = 1 ms was performed with decoupling powers varied from 0 kHz to 160 kHz, resulting in correspondingly varied C' intensities (Fig. 4.4). Secondly, decoupling power was held at 160 kHz during the τ-π-τ refocused echo period, and intensities were measured with τ periods of 1 ms, 2ms, 4 ms, 6 ms, 8 ms, 10 ms, and 12 ms respectively. Since

$$Intensity = Cnst\ e^{-(2\tau + pulselength)/T_2'} \quad (1)$$

for homogeneous broadened linewidth, with *Cnst* indicating the proportional constant, and T_2' the refocused transverse relaxation time. The T_2' and *Cnst* can be fitted to the exponential function with intensities, τ values, and the length of selective π pulse plugged in (Fig. 4.5). With the *Cnst* defined,

$$T_2' = \frac{2\tau + pulselength}{Ln(Cnst/Intensity)} \quad (2)$$

Then the T_2's can be derived from Fig 4.4 from intensities, creating the T_2' profile corresponding to the decoupling strength ω1 from 0 to 160 kHz (Fig 4.6 Blue). For MAS rates of 20 kHz, 25 kHz, and 27.5 kHz, T_2' for C^{α}, C^{β}, and C' were all mapped. And at 30 kHz, 40 kHz, and 50 kHz, T_2' were mapped for C^{α} and C'.

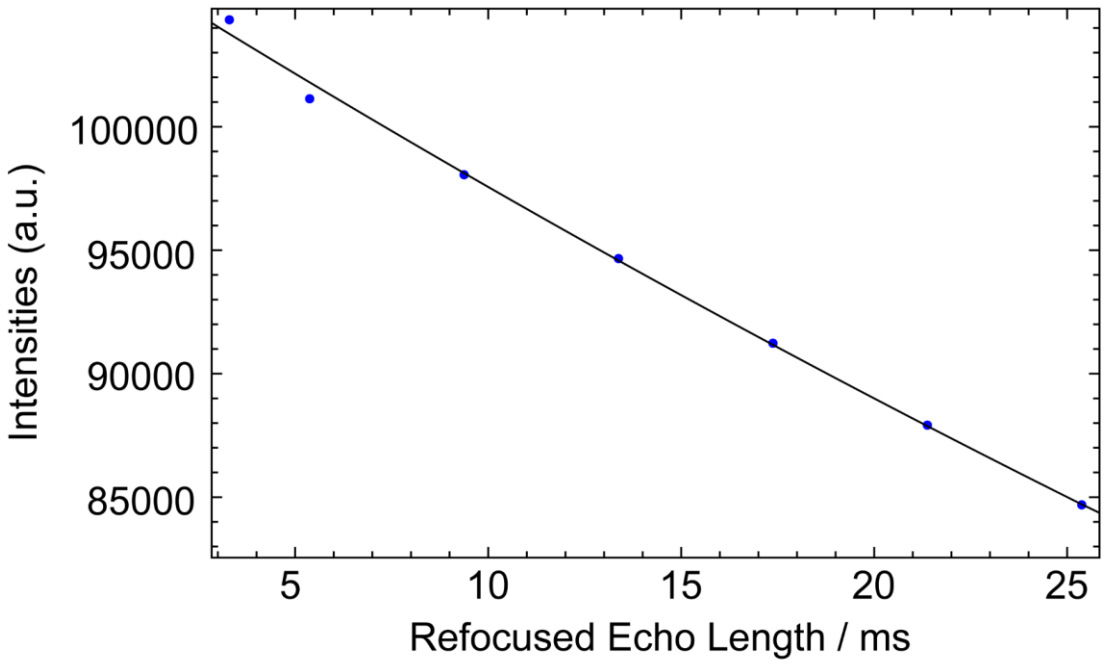

Figure 4.5. Fitting of T_2' from the intensities recorded on C' of the U-^{13}C-^{15}N-labeled L-alanine, with the τ delay of the τ-π-τ echo period varied from 1 ms to 12 ms. The XiX decoupling strength was maintained at 160 kHz during the echo period, with $t_p = 1.85\ t_\tau$ condition.

In the case of C', which is not directly attached to ^{1}H's in L-alanine, at MAS rate of 20 kHz, intensities already reached plateau at around 100 kHz decoupling strength (ω1). When spinning speed was increased to 25 kHz, the T_2' increased more rapidly at the similar region of ω1 (Fig 4.6 Green). However, still taking 100 kHz ω1 as an example, now the ω1 value is only four times the spinning speed instead of five, resulting in the actual decoupling performance similar as decoupling at the 20 kHz MAS spinning speed. If the spinning speed is raised to 27.5 kHz (Fig 4.6 Red), the high power XiX decoupling did not perform as good as at 25 kHz. This is probably due to the smaller ratio of decoupling strength to MAS rate when holding the decoupling power constant.[14] Although in all cases, the spinning speed range of 20 kHz to 27.5 kHz did not induce differences for the

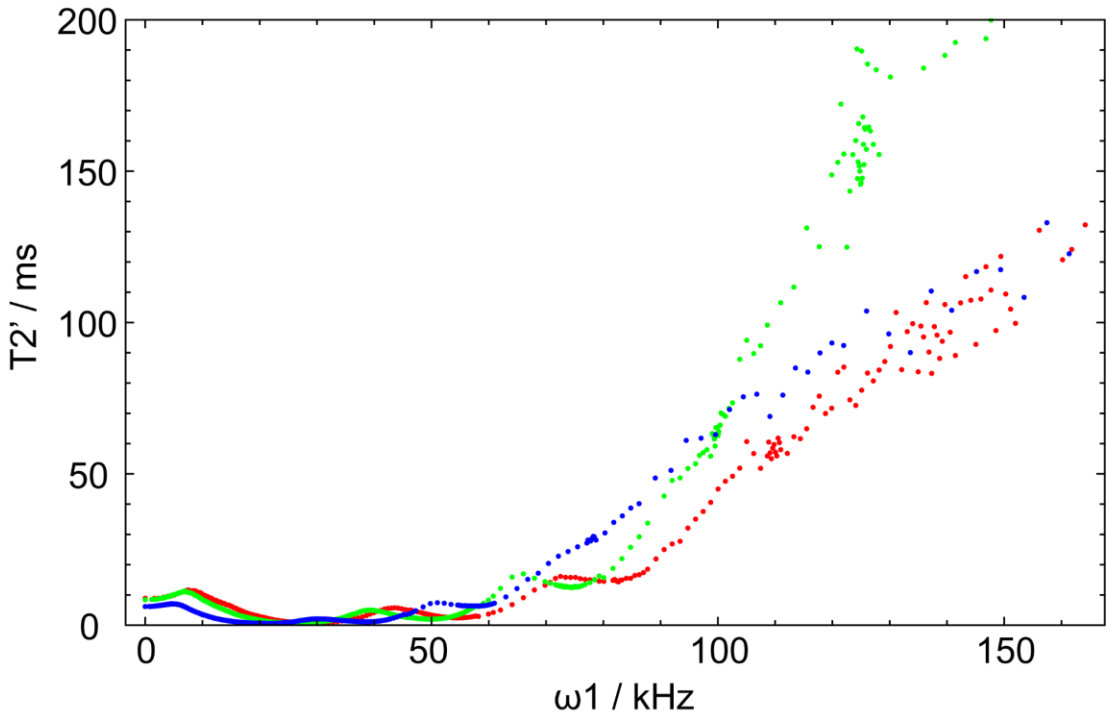

Figure 4.6. Refocused transverse relaxation time (T_2') mapped on C' of the U-^{13}C-^{15}N-labeled L-alanine at 20 kHz (Blue), 25 kHz (Green), and 27.5 kHz (Red). The decoupling strength (ω1) during the τ-π-τ echo period was varied from 0 kHz to 160 kHz.

performance at high power, with T_2' easily exceeding 60 ms. Nevertheless, even at these MAS rates, low power XiX, of decoupling power less than the MAS rates, already shows maxima at around ¼ the spinning speeds, as described by Ernst et al.[24] The low power XiX maximum intensities increased as the MAS rates increased, with the largest T_2' being around 14 ms at 27.5 kHz MAS. As ω1 being more than the ¼ maximum, at ω1= ω_r, T_2' minimized due to the rotary resonance recoupling (R^3) condition.[25] T_2' would not start to show apparent increase until larger than $2\omega_r$. And when ω1 is larger than $2\omega_r$, local minimum at ω1 = $3\omega_r$ and at ω1 = $4\omega_r$ would appear on the T_2' slope.

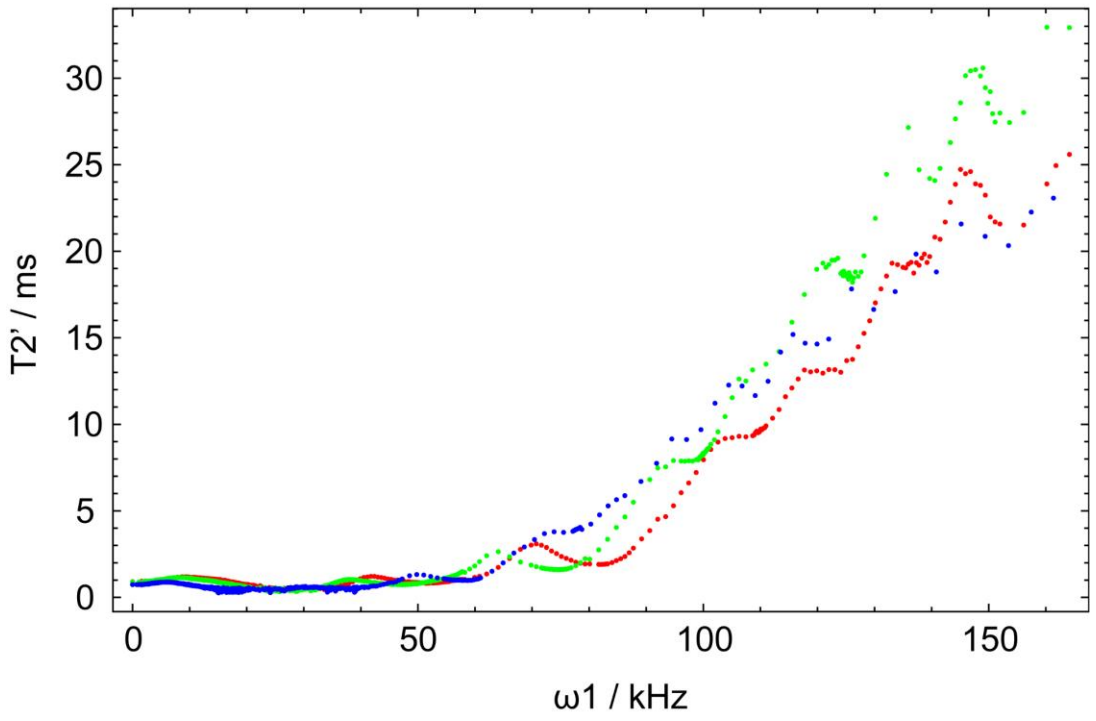

Figure 4.7. Refocused transverse relaxation time (T_2') mapped on C^{α} of the U-^{13}C-^{15}N-labeled L-alanine at 20 kHz (Blue), 25 kHz (Green), and 27.5 kHz (Red). The decoupling strength (ω1) during the τ-π-τ echo period was varied from 0 kHz to 160 kHz.

The T_2' curve of C^{α} is shown in Fig 4.7 for MAS of 20 kHz, 25 kHz, and 27.5 kHz. The C^{α} is not as easy to decouple as compared to C', resulting in the maximum T_2' being only 30 ms (Fig 4.7 Green). For $\omega 1 < 2\omega_r$, T_2' was less than 3 ms, while at higher $\omega 1$, T_2' increased more rapidly with respect to decoupling powers. At lower power XiX, as expected, at the ¼ $\omega 1/\omega_r$ ratio maxima, XiX did not give improved T_2' at this scale of spinning speed yet. On the other hand, at high power, for the decoupling strengths available (in the range from 0 kHz to 160 kHz), the T_2' was observed the highest at 25 kHz MAS at around 150 kHz $\omega 1$. Although the maximum T_2' did not appear at MAS rate of 27.5 kHz, as one would expect; since XiX usually performs better at higher MAS rates. This observation can be explained by the higher $\omega 1/\omega_r$ ratio at 25 kHz when comparing the 25 kHz and 27.5 kHz MAS rates, with same range of available decoupling powers.[14,26] And when comparing the 20 kHz and 25 kHz MAS, at 150 kHz $\omega 1$, the decoupling strength is already six times the 25 kHz MAS rate. As the $\omega 1/\omega_r$ ratio grow higher, the less it will contribute to decoupling performance. The ratio of six is already near the convergence, where the decoupling performance depends more on the MAS rate, resulting in the decoupling at the 25 kHz MAS better than at 20 kHz MAS. In summary, the measurements provide us the preferred conditions when applying XiX on protein samples, with both the consideration of MAS and the $\omega 1/\omega_r$ ratio. And most likely due to the C^{α} in L-alanine being similar to the C^{α}'s of protein backbone residues, the measured T_2' values are on the same scale in comparison with our previous T_2' values acquired on U-^{13}C-^{15}N GB1 samples at 25 kHz MAS.[27] Such data is useful for rapid inquiries of T_2' on small amino acid samples, without the necessity for extensive number of scans usually required for a less sensitive

protein sample. For the application using our 2.5 mm probe, 25 kHz MAS and 150 kHz XiX decoupling strength would be the most realistic combination when T_2' is in need.

The T_2' of C^{β} is also included in the study at MAS of 20 kHz, 25 kHz, and 27.5 kHz. C^{β} is not usually encountered in correlation methods for protein backbone structures, although for correlation experiments of aliphatic regions, the position in L-alanine does resemble certain similarities of some amino acid side chains, like the side chains of valine, leucine, and isoleucine. Also, since the C^{β} in L-alanine has the most number of ^{1}H attached, it is also interesting to check the position for ^{1}H decoupling performance. The plot for T_2' is shown in Fig 4.8. The general trend is very similar to that of C^{α} (Fig 4.7). T_2' is very

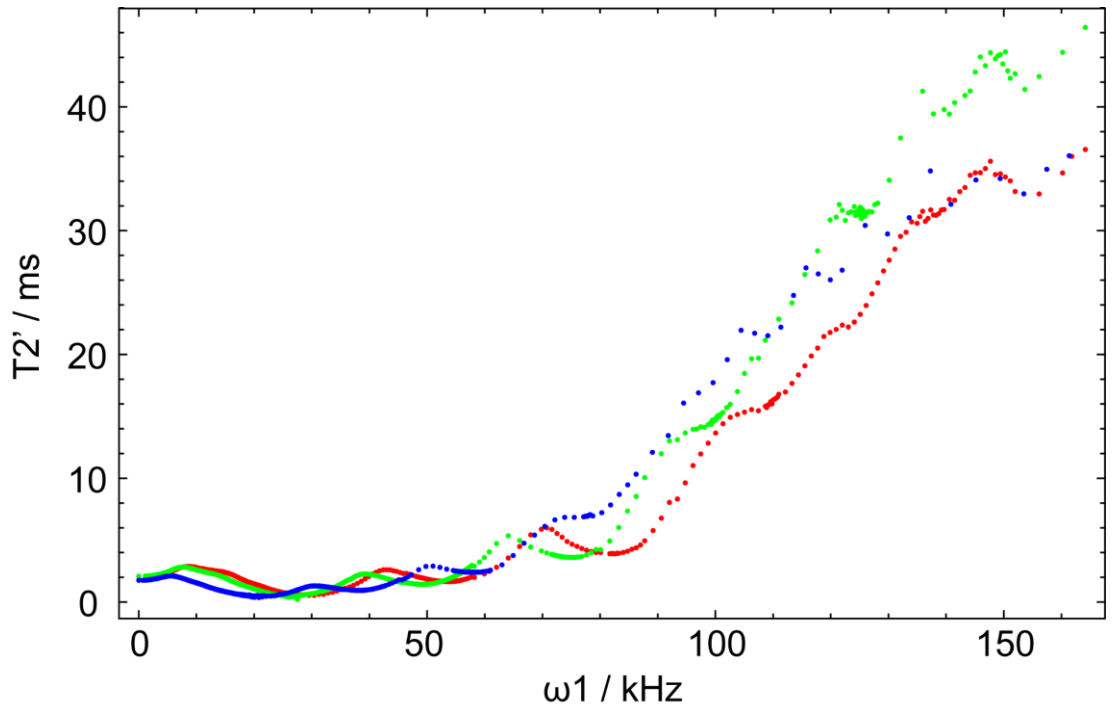

Figure 4.8. Refocused transverse relaxation time (T_2') mapped on C^{β} of the U-^{13}C-^{15}N-labeled L-alanine at 20 kHz (Blue), 25 kHz (Green), and 27.5 kHz (Red). The decoupling strength (ω1) during the τ-π-τ echo period was varied from 0 kHz to 160 kHz.

small (less than 4 ms) until decoupling strength ω1 larger than $2\omega_r$, and the T_2' increased almost linearly with respect to ω1 above the $2\omega_r$ region, with the modulation spaced by ω_r on top of the linear trend. For the entire 0 kHz to 160 kHz region, at $\omega 1 = n\,\omega_r$, certain rotary recoupling conditions happen, resulting in local minima at these integer multiples of ω_r. Among these conditions, at higher n values, local minima turns out to be less severe than the lower n conditions, with n=1 R^3 condition corresponds to the lowest T_2' minima. The same trend is preserved for spinning speed at 20 kHz, 25 kHz, and 27.5 kHz. Still, with the decoupling strength available, ω1 at around 150 kHz with 25 kHz MAS results in the optimum T_2' of around 40 ms.

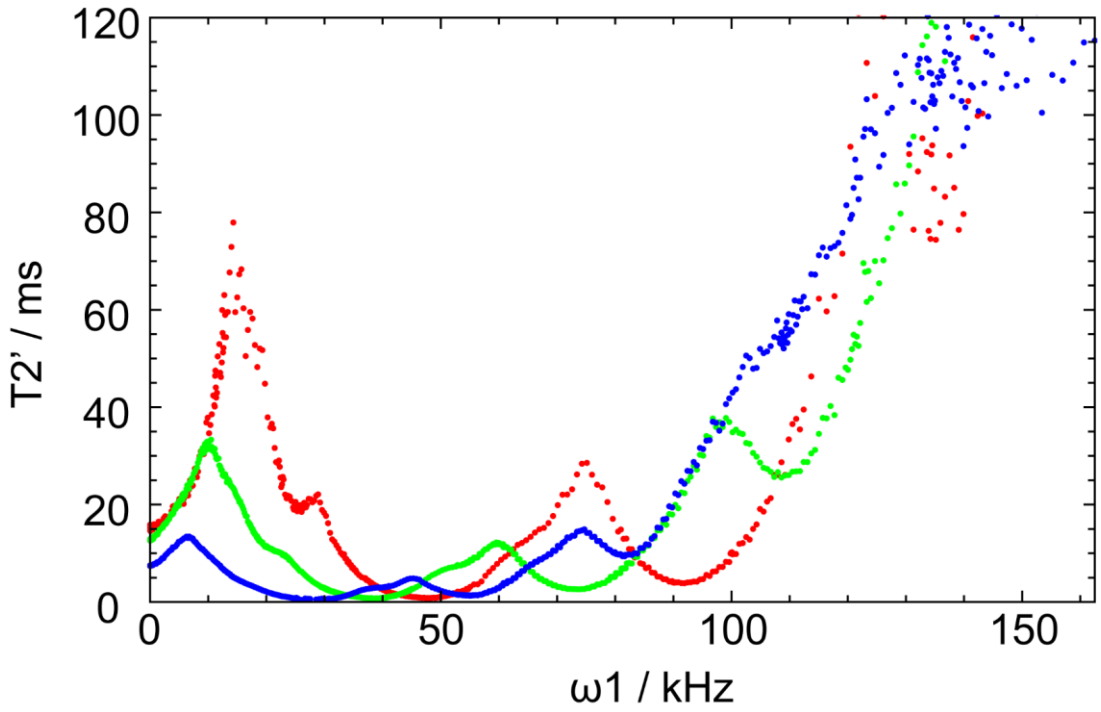

Figure 4.9. Refocused transverse relaxation time (T_2') mapped on C' of the U-^{13}C-^{15}N-labeled L-alanine at 30 kHz (Blue), 40 kHz (Green), and 50 kHz (Red). The decoupling strength (ω1) during the τ-π-τ echo period was varied from 0 kHz to 160 kHz.

At higher MAS, XiX decoupling performance was studied using a 1.3 mm probe with spinning speed of 30 kHz, 40 kHz, and 50 kHz. As the spinning speed goes up, the T_2' landscapes begin to show more interesting features.

For C' (Fig. 4.9), the non-hydrogen attached position is most easily decoupled. Without any decoupling power ($\omega 1 = 0$), the T_2' is already 7 ms at 30 kHz MAS (Fig 4.9 Blue), 13 ms at 40 kHz MAS (Fig 4.9 Green), and 15 ms at 50 kHz MAS (Fig 4.9 Red). This indicates that when the spinning speed is exceeding the ^{1}H-^{1}H or ^{1}H-^{13}C dipolar coupling strength, MAS is effective in removing the dipolar interactions. More interesting is the low power region. At the theoretical $\omega 1/\omega_r=1/4$ low power XiX decoupling condition, the maxima increased as the MAS increases: T_2' is 15 ms at 30 kHz MAS, 35 ms at 40 kHz MAS, and almost 80 ms at 50 kHz MAS. The T_2' values at the maxima can be fitted to the MAS rate by at least a second order polynomial, and potentially an exponential function. In either case, T_2' benefit a lot from the combined effect of high MAS and XiX decoupling scheme. The low decoupling power can help avoid sample heating induced by RF power, especially for protein sample with water solvent. Also, the 80 ms T_2' is already adequate for correlation techniques involving evolution periods on C'. On the shoulder of the right side of the low power $\omega 1$, the HORROR condition[28] started to show up at 40 kHz (Fig 4.9 Green at around 20 kHz $\omega 1$), and became apparent at 50 kHz (Fig 4.9 Red at 25 kHz $\omega 1$). For decoupling at high power, for example 150 kHz, although $\omega 1/\omega_r$ ratio is only 3 at 50 kHz MAS, while 5 at 30 kHz, similar T_2' were achieved in both cases of about 100 ms. In reality, our 1.3 mm rotor has been designed to spin more stable at above 30 kHz conditions.

The T_2' data for the 40 kHz and 50 kHz MAS rates are more useful because of this. And in both cases, the maximum T_2' still appears at high power.

T_2' measurements at 30 kHz, 40 kHz, and 50 kHz were also carried out on C^{α} (Fig 4.10). C^{α} has been an essential site of a protein residue, because of wider distributions of chemical shifts among different amino acid species. The distribution of chemical shift distinguishes residues better, which is beneficial for solving a protein structure. A longer T_2' granted more flexibility in designing more complex correlation techniques with evolution periods on C^{α}, thus better resolution. In the scan of T_2' against decoupling strength ω1, at zero decoupling power, T_2' is also zero. This means that in the region where MAS is comparable to dipolar couplings between directly bonded ^{1}H-^{13}C and nearest ^{1}H-

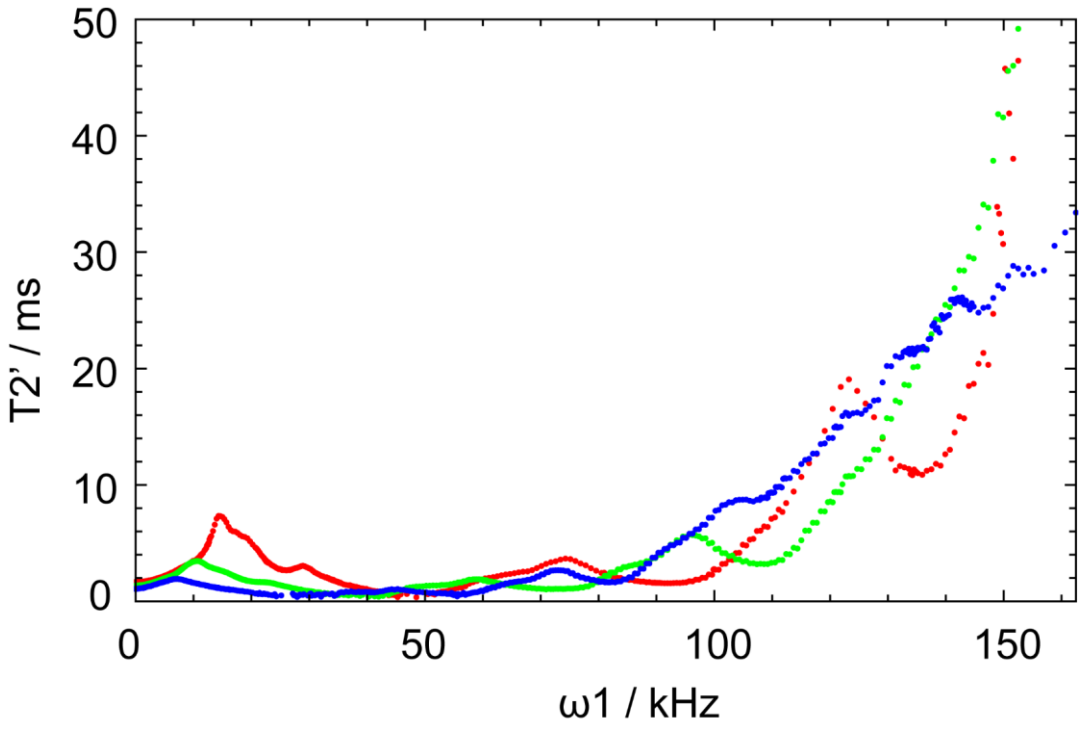

Figure 4.10. Refocused transverse relaxation time (T_2') mapped on C^{α} of the U-^{13}C-^{15}N-labeled L-alanine at 30 kHz (Blue), 40 kHz (Green), and 50 kHz (Red). The decoupling strength (ω1) during the τ-π-τ echo period was varied from 0 kHz to 160 kHz.

^{1}H (around 40 kHz),[29] MAS alone is still not enough to average out even partially the dipolar coupling induced relaxation. However, at low decoupling power, the maxima at around ¼ $\omega 1/\omega_r$ ratio of higher MAS rates (Fig. 4.10) appear to be more apparent than the lower spinning speed conditions (Fig. 4.7). The most apparent low power maxima was observed at the 50 kHz MAS (Fig. 4.10 Red), with a corresponding T_2' of 8 ms. The value is still too small for real applications including evolving on C^{α}, although at higher spinning speed (>50 kHz), the low power decoupling can potentially provide longer T_2'. At higher end of decoupling power, the maximum T_2' achieved at 30 kHz is around 30 ms (Fig. 4.10 blue). For the T_2' data of 40 kHz (Fig. 4.10 Green) and 50 kHz (Fig. 4.10 Red) at the highest ω1 values, care should be taken in interpreting the result. At above the 150 kHz ω1, the

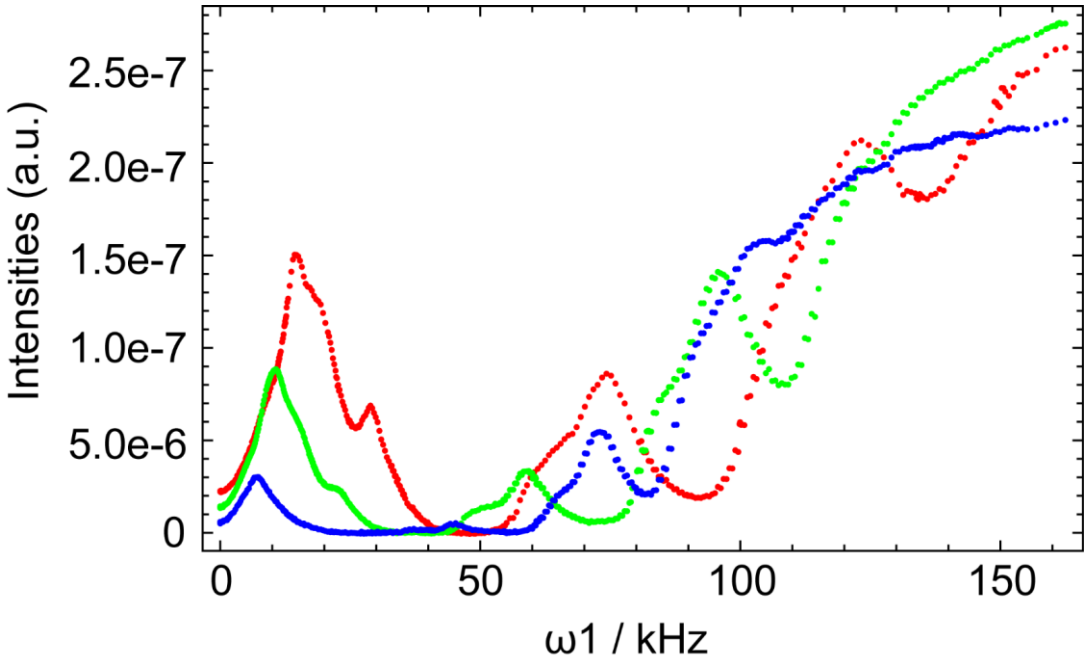

Figure 4.11. Intensities of C^{α} of the U-^{13}C-^{15}N-labeled L-alanine at 30 kHz (Blue), 40 kHz (Green), and 50 kHz (Red). The decoupling strength (ω1) during the τ-π-τ echo period was varied from 0 kHz to 160 kHz.

derived T_2' experienced great increase of 20 ms within the increase of decoupling strength of only 5 kHz. Similar phenomena, of even larger variations were also observed for T_2' of C' at similar regions of ω1, where T_2' were at higher end (Fig. 4.6 and Fig. 4.9). Direct T_2' measurements were then performed within the region, resulting in the actual maximum T_2' been 30 ms for C^{α} at both 40 kHz and 50 kHz MAS rates, and 150 ms for C' at 50 kHz MAS. The unstable behavior of T_2' at high decoupling power can be explained by the derivation of T_2', where in equation (2), the intensities were on the denominator. As the ω1 increases, the intensity is approaching the fitted *Cnst*, causing the denominator to decrease to almost zero, leading to the diverged T_2' of the higher end ω1 values. T_2' at lower intensities are more stable, with intensities been further away from the fitted *Cnst*. For the precise T_2' values at the very high ω1 decoupling intensities, a more precise way would be

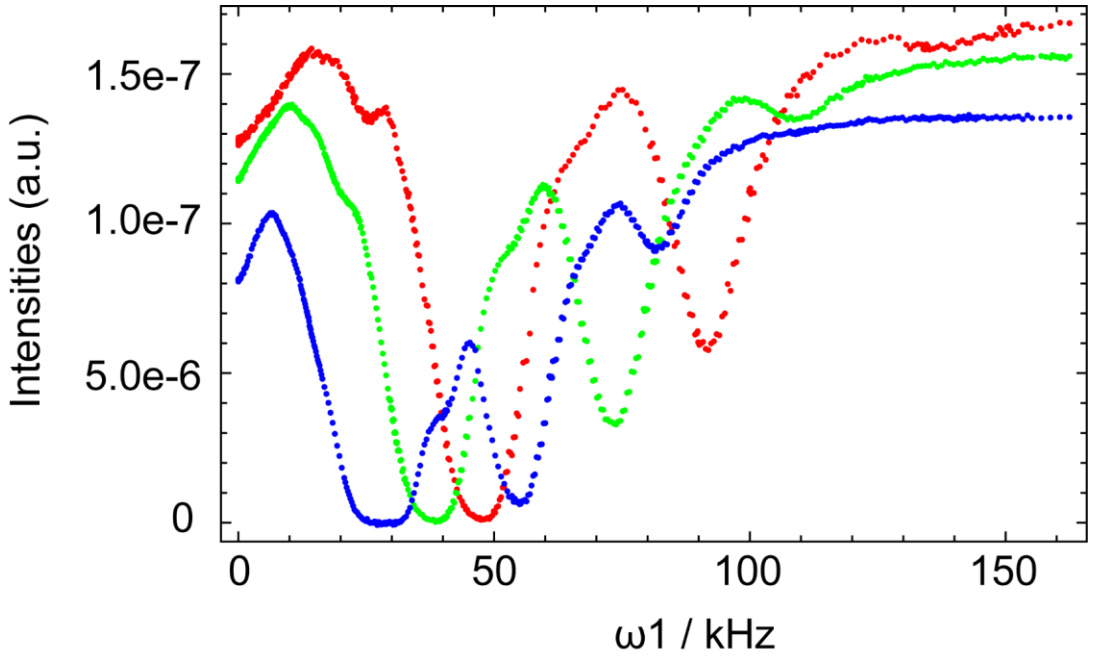

Figure 4.12. Intensities of C' of the U-^{13}C-^{15}N-labeled L-alanine at 30 kHz (Blue), 40 kHz (Green), and 50 kHz (Red). The decoupling strength (ω1) during the τ-π-τ echo period was varied from 0 kHz to 160 kHz.

to fit T_2' at the intensities with varied echo period directly. The intensities of C^{α} after the 3.4 ms total refocused echo period with varied decoupling powers are shown in Fig 4.11. And same experiment on C' is also shown in Fig 4.12. For C^{α}, at the higher end of the decoupling power, intensities were still climbing, indicating potential better performance (higher T_2') at even higher powers. However, within the power range of the scan, C^{α} peak intensity at 40 kHz MAS is slightly higher than at 50 kHz MAS, while maximum direct calculated T_2' was 30 ms at 50 kHz MAS, and 29.4 ms at 40 kHz. For C', at 50 kHz MAS, the decoupling is more effective than at 40 kHz (Fig 4.12), with higher peak intensity and the maximum T_2' of 158 ms, while at 40 kHz, maximum T_2' directly measured is 132 ms.

4.3.2 Correlation Experiments Performed on Pf1 Bacteriophage

The two-dimensional proton-detected-HN correlation solid-state NMR spectra are shown for the major coat protein of Pf1 bacteriophage in Fig. 4.13. The experiments were performed at an MAS rate of 50 kHz using a 1.3 mm triple resonance probe. The HN correlation experiment of regular protonated, U-^{15}N-labeled Pf1 bacteriophage is shown in Fig. 4.13(c). Although Glycine peaks from ^{15}N chemical shifts of 105 ppm to 110 ppm region can be identified and almost resolved, other region suffer from heavily peak overlay. Deuteration of the sample with partial reprotonation of exchangeable NH sites greatly improved the correlation experiment result (Fig. 4.13(b)). The proton resonance linewidths of the six glycines of the perdeuterated sample (113 ± 15 Hz) (Fig. 4.14(a, b)) are reduced by a factor of approximately 3 compared to those of the fully protonated sample (302 ± 48

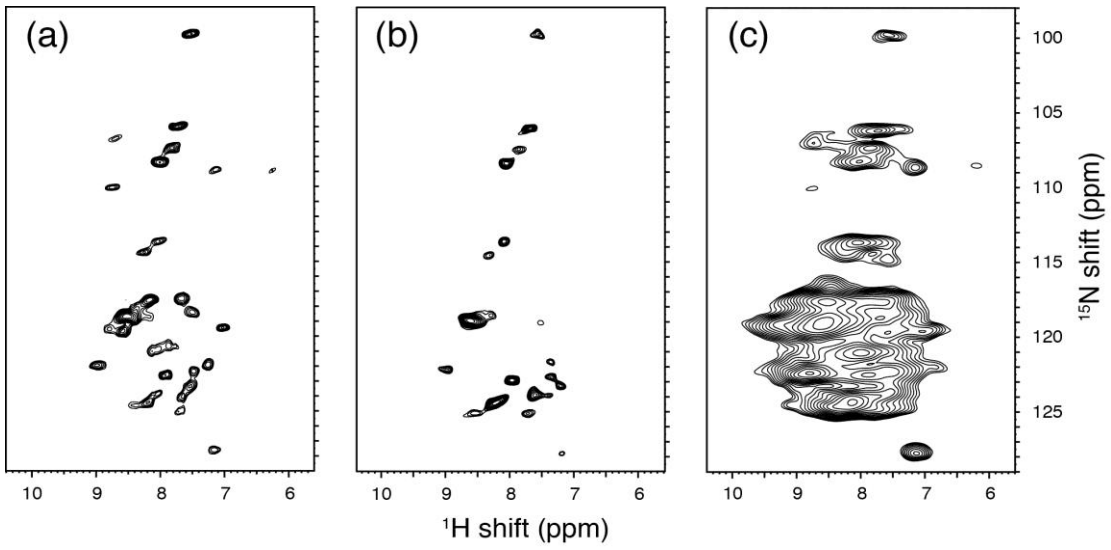

Figure 4.13. Complete two-dimensional proton-detected HN correlation solid-state NMR spectra of the major coat protein of Pf1 bacteriophage at an MAS rate of 50 kHz. (a) ^{2}H, ^{15}N-labeled sample with complete reprotonation of exchangeable NH sites. (b) ^{2}H, ^{15}N-labeled sample with partial reprotonation of exchangeable NH sites. (c) Regular, protonated, uniformly ^{15}N-labeled sample.

Hz) (Fig. 4.13(c)). The partially protonated sample was prepared with purification completed using protonated aqueous solution after the expression of U-^{2}H-^{15}N-labeled Pf1. In comparison with the fully reprotonated sample (Fig 4.13(a)), 13 resonances are missing in the spectrum for partially reprotonated sample (Fig 4.13(b)). The complete reprotonation was achieved by placing the partially reprotonated sample, with supernatant containing $^{1}H_2O$, in a 60 °C water bath for 30 min at pH 8, and then slowly cooling the sample to room temperature.[30,31] The difficulty of reintroducing in the proton at exchangeable nitrogen sites is most likely due to the hydrogen bonding in the transmembrane helix. This is supported by identifying the missing resonances being mostly between L26 and Y43.[31]

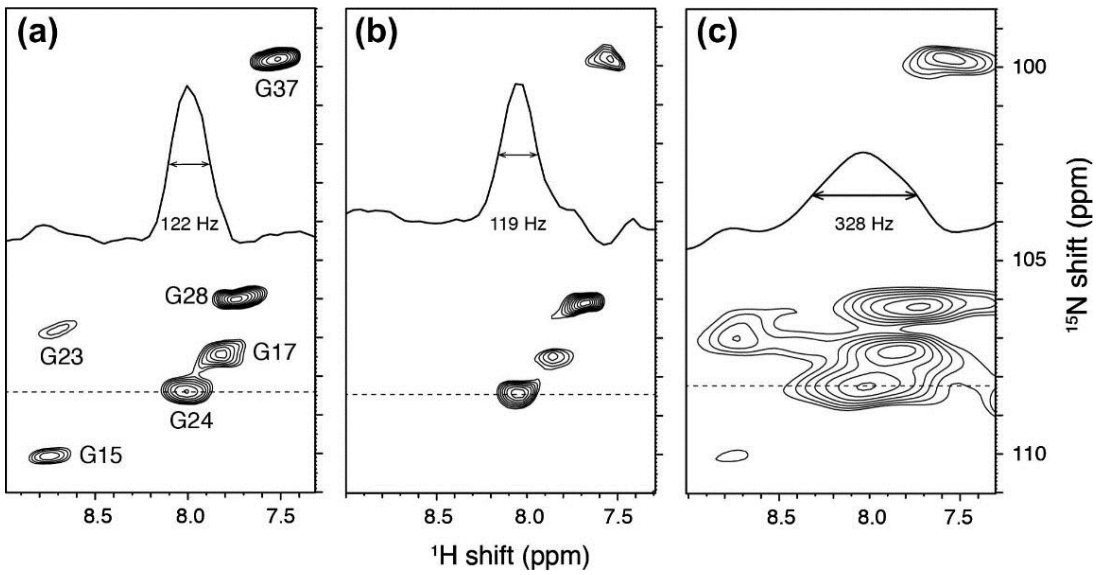

Figure 4.14. Expanded spectral region of two-dimensional proton-detected HN correlation solid-state NMR spectra of the major coat protein of Pf1 bacteriophage at an MAS rate of 50 kHz. (a) ^{2}H,^{15}N-labeled sample with complete reprotonation of exchangeable NH sites. (b) ^{2}H,^{15}N-labeled sample with partial reprotonation of exchangeable NH sites. (c) Regular, protonated, uniformly ^{15}N-labeled sample. The assignments of the Gly residues are marked and the linewidths from the slices through the resonance for residue Gly24 are shown.

Besides contributing to narrower linewidth, the deuteration of the Pf1 sample enabled the measurements of NH distances at the 50 kHz MAS. ^{15}N-^{1}H spin pairs along the protein backbone are isolated in the deuterated sample,[17] which would otherwise be surrounded by ^{1}H dipolar coupling network involving multiple-spin interactions. The experimental three-dimensional spectrum is presented as a cube in Fig. 4.15(a).[31] The spectrum was obtained by applying the pulse sequence Fig 4.2 derived from the two-dimensional correlation experiment by systematically varying the length of the first CP contact time. The dipolar transfer of magnetization from ^{1}H to ^{15}N during the spin lock follows the analytical form derived by Vogt et al.

$$S(t) = \frac{1}{2} - \frac{1}{2} J_0\left(\frac{\pi D t}{\sqrt{2}}\right) + \sum_k \frac{1}{16k^2-1} J_{2k}\left(\frac{\pi D t}{\sqrt{2}}\right), \quad (3)$$

Where the dipolar coupling, D, is given in Hz and J_k are Bessel functions of the first kind. The experimental signal is typically shifted so that it decays to zero before Fourier

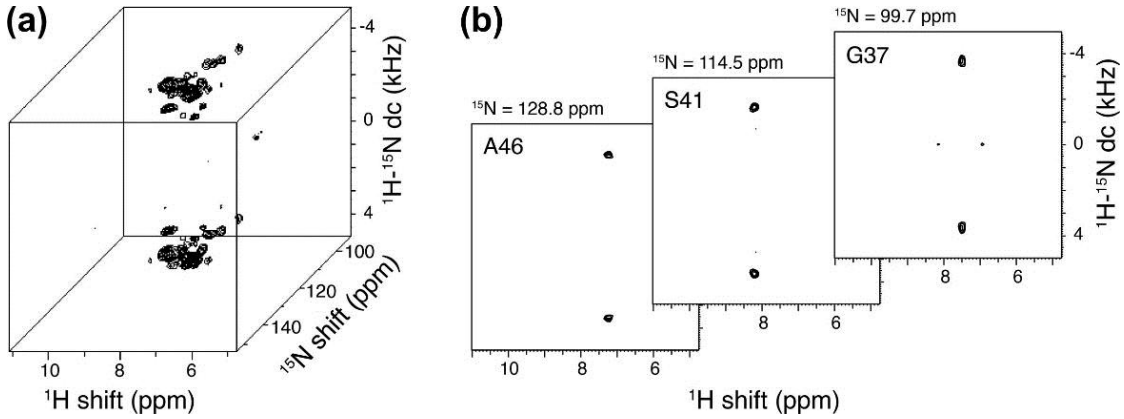

Figure 4.15. Expanded spectral region of two-dimensional proton-detected HN correlation solid-state NMR spectra of the major coat protein of Pf1 bacteriophage at an MAS rate of 50 kHz. (a) ^{2}H,^{15}N-labeled sample with complete reprotonation of exchangeable NH sites. (b) ^{2}H,^{15}N-labeled sample with partial reprotonation of exchangeable NH sites. (c) Regular, protonated, uniformly ^{15}N-labeled sample. The assignments of the Gly residues are marked and the linewidths from the slices through the resonance for residue Gly24 are shown.

transformation. This can be accomplished by subtracting a constant from the experimental data or, as implemented here, using the solvent suppression method of Marion et al.,[20] that removes additional low-frequency components (that can arise from $T_{1\rho}$ decay during the CP period, for example) along with the zero-frequency term. The Fourier transform of the resulting signal

$$S'(t) = \frac{1}{2}J_0\left(\frac{\pi Dt}{\sqrt{2}}\right) + \sum_k \frac{1}{16k^2-1}J_{2k}\left(\frac{\pi Dt}{\sqrt{2}}\right), \tag{4}$$

can be performed analytically[32] to give the frequency-domain signal

$$S'(\nu) = \begin{cases} \dfrac{\sqrt{1-\sqrt{1-\dfrac{8\nu^2}{D^2}}+\sqrt{1+\sqrt{1-\dfrac{8\nu^2}{D^2}}}}}{2\pi D\sqrt{1-\dfrac{8\nu^2}{D^2}}} & |\nu| \le \dfrac{D}{2\sqrt{2}} \\ 0 & |\nu| > \dfrac{D}{2\sqrt{2}} \end{cases} \tag{5}$$

The equation will have maxima (discontinuity) at the condition

$$1 - \frac{8\nu^2}{D^2} = 0 \tag{6}$$

This condition results in dipolar coupling constant at $\sqrt{2}$ times the frequency difference between the discontinuities.[17]

The sample of uniformly ^{15}N and perdeuterated Pf1 bacteriophage yielded the two-dimensional ^{1}H-^{15}N dipolar coupling/^{1}H chemical shift planes taken from the three-dimensional spectrum at ^{15}N chemical shift frequencies of 128.8 ppm, 114.5 ppm, and 99.7 ppm; these spectra show single-site resolution of ^{1}H-^{15}N dipolar couplings for A46, S41, and G37, respectively (Fig. 4.15). The average ^{1}H-^{15}N dipolar coupling for six glycine residues is 10.49±0.05 kHz, which is close to the rigid lattice value of 10.5 kHz,

corresponding to an NH bond length of 1.05 Å, indicating the backbone nitrogen being rigid on the time scales of 10^6 Hz under our sample conditions.

4.3.3 The Study of Correlation Techniques by Using GB1 samples

The two-dimensional proton-detected-HN correlation solid-state NMR was also applied on U-^{2}H-^{13}C-^{15}N-labeled GB1 sample using a 1.3 mm rotor at 50 kHz MAS. Then

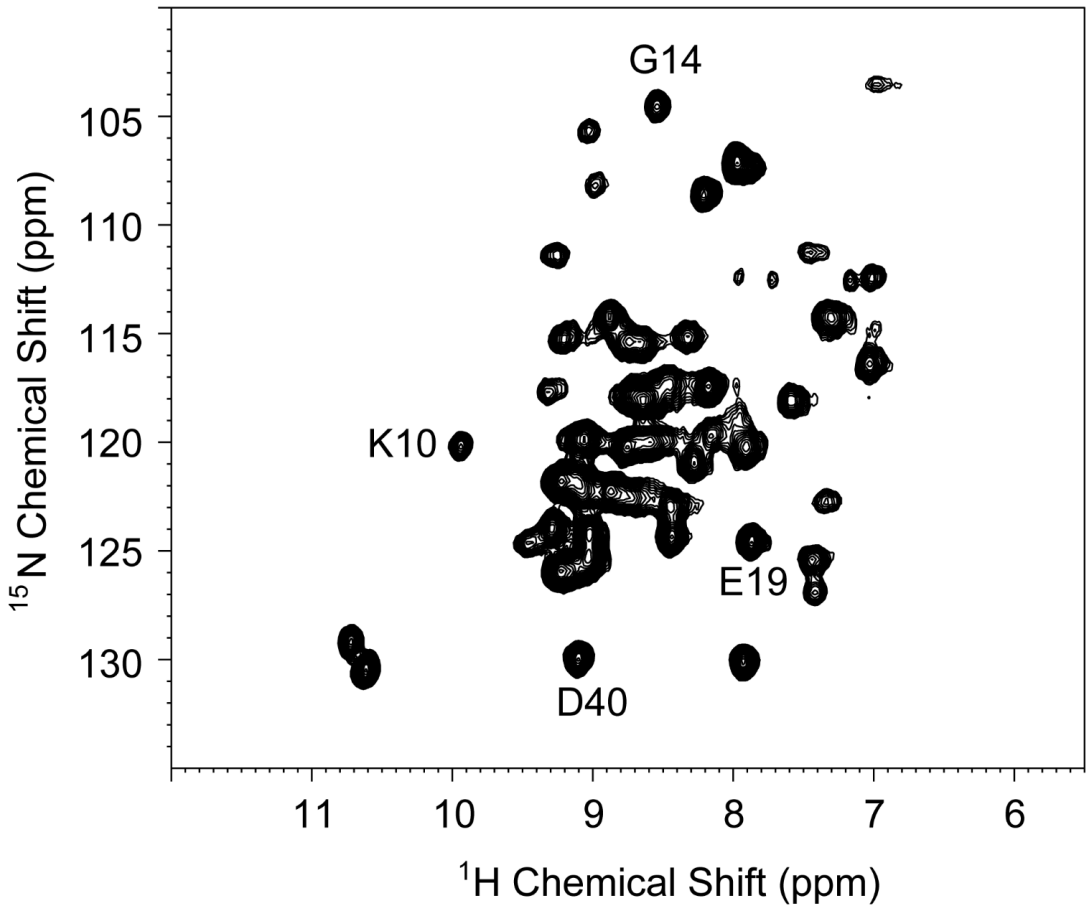

Figure 4.16. Solid-state proton-detected-HN 2D NMR spectrum of U-^{2}H,^{13}C,^{15}N-labeled GB1, back-exchanged with $^{1}H_2O$ (600 MHz, 50 kHz MAS). 20 Hz EM linebroadening was used in ^{1}H dimension, and cosine-squared window function was used in ^{15}N dimension. Linewidth was measured by using the four proton resonances labeled on the 2D spectrum.

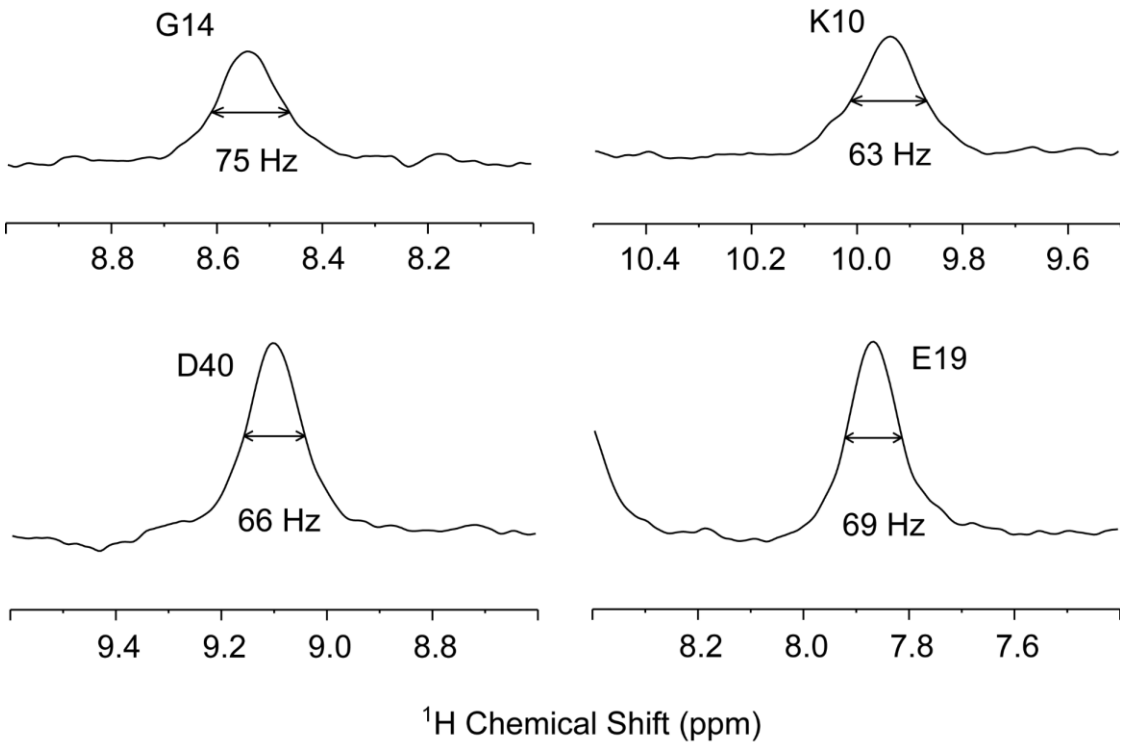

Figure 4.17. Slices from solid-state proton-detected-HN 2D NMR spectrum of U-^{2}H,^{13}C,^{15}N-labeled GB1, back-exchanged with $^{1}H_2O$ (600 MHz, 50 kHz MAS). The residue names are labeled on the side of the peaks. And linewidth were measured by fitting the experimental peaks against lorentzian lineshape.

proton-detected-(H)CONH and proton-detected-(H)CANH correlation methods were explored for the preparation of correlation techniques to be applied on tryptophan synthase in the future at 50 kHz MAS.

The spectrum of proton-detected-HN 2D correlation is shown in Fig.4.16. The sample was deuterated, and back-exchanged during purification, with buffer prepared using $^{1}H_2O$. The proton resonance linewidths were estimated using the peaks marked with residue name in the 2D spectrum. The corresponding slices are displayed in Fig. 4.17. Proton resonance inewidths are in the range of 63 Hz to 75 Hz, which were fitted against a

lorentzian lineshape function. The residue assignments followed a previous work by Donghua Zhou et al.[6] Proton detection at 50 kHz MAS in combination with perdeuteration and back-exchange provided us a powerful tool. The technique benefit from the high sensitivity gained by detecting on ^{1}H, and high resolution because of deuteration. The experiment is useful for chemical shift measurements of each residue. The pulse sequence can be further modified for multidimensional correlation techniques including carbon dimension(s),[2] or distance measurements using variable contact time during CP.[17] Although the sample was already deuterated, with ^{1}H presenting on exchangeable ^{15}N only, intensities from $^{1}H_2O$ and ^{1}H of precipitants were very strong. If we directly acquire the ^{1}H spectrum of the GB1 sample right after a 90° pulse, protein ^{1}H signals will be mostly covered by the signals of H_2O and precipitants. Water suppression (Fig. 4.2) before the

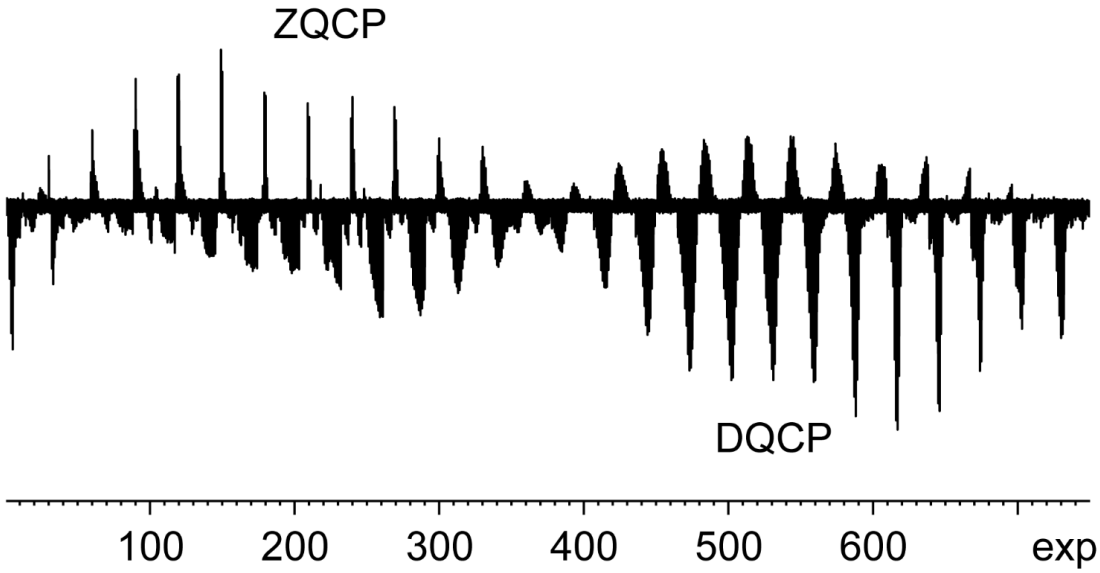

Figure 4.18. Intensities from the carbonyl carbon of U-^{13}C,^{15}N-labeled glycine of a (H)C CP experiment. (600 MHz, 50 kHz MAS). CP powers on C' and H were both varied throughout the n=1 ZQCP and n=1 DQCP region, with a constant contact time of 2ms. Other regions was not explored due to considerations on power level (for n>1 ZQCP) and offset effects (SOCP and n>2 DQCP).

acquisition was effective in removing the signals covering the protein chemical shift region.[5] Deuterated precipitants can further improve the linewidth, in combination with water suppression. However, the application of the correlation technique will be applied at last on tryptophan synthase, using PEG (polyethylene glycol) 3000 precipitant. And the deuteration of PEG 3000 would require nontrivial efforts.

Another interesting observation at 50 kHz MAS is that, double quantum (DQ) transfer turned out to be more effective than zero-quantum (ZQ) during cross polarization.[33,34] An example is shown on a U-^{13}C-^{15}N-labeled glycine sample (Fig. 4.18). Both CP powers on ^{1}H and ^{13}C were optimized with offset on ^{13}C channel centered near the carbonyl region. The intensity of carbonyl carbon was monitored throughout the CP power range. The n=1 ZQCP match condition was observed on the left region with positive intensities. And the n=1 DQCP condition was matched on the right region with negative intensities. The DQCP condition resulted in larger intensity for the glycine sample at C'. The C' was the preferred position for monitoring the intensity, due to its closer similarity to deuterated protein system. Since in deuterated proteins, ^{1}H would only directly bond with nitrogen. Thus in a deuterated protein backbone, HC correlation can be established most likely from a neighboring proton attached to nitrogen. Both ZQCP and DQCP conditions were explored on GB1 sample then. And the effect of deuteration was also considered, by using both the deuterated and non deuterated GB1 of ^{13}C and ^{15}N enrichment. The effectiveness of proton-carbon cross polarization was studied by indirectly monitoring the (HC)N correlation 1D nitrogen spectra. The SPCP of CN part

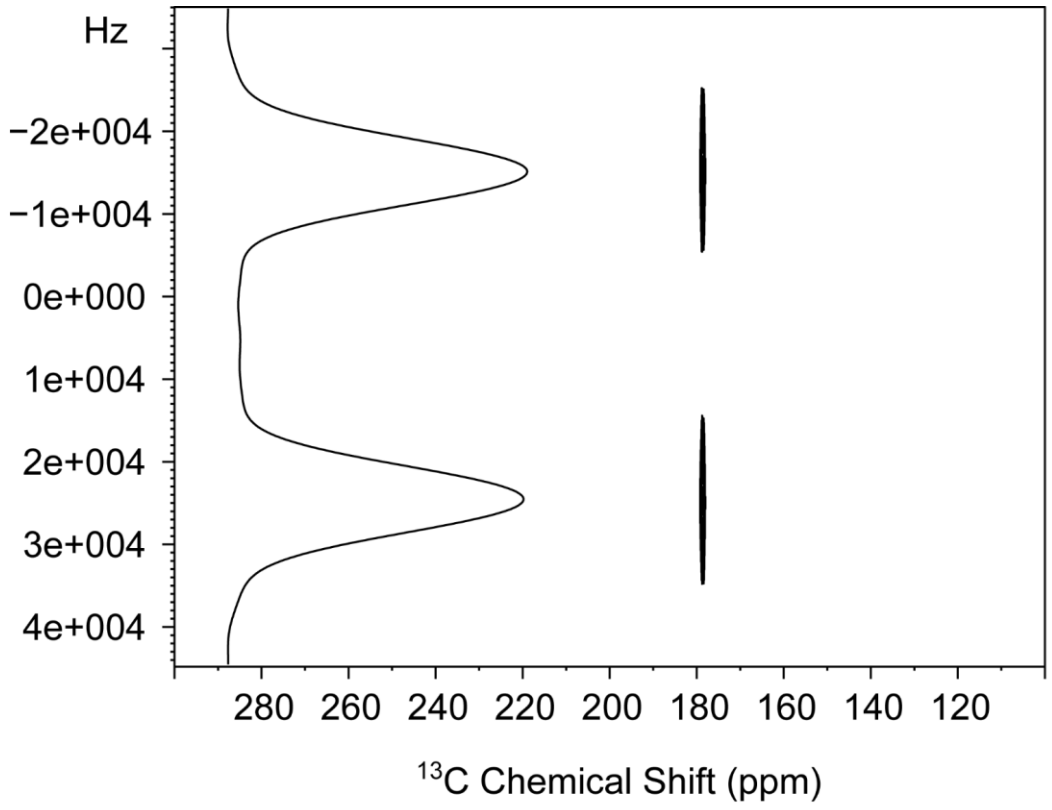

Figure 4.19. ^{1}H nutation frequency 2D spectrum acquired on U-^{13}C,^{15}N-labeled glycine, with HC CP condition optimized on C' The corresponding effective nutation frequency of the proton power was quantified by measuring half of the distance between the two peaks in the indirect dimension.

was held the same, while HC polarization transfer were performed at both ZQCP n=1 and DQCP n=1 conditions. The CP conditions were determined with CP power levels exactly quantified through ^{1}H and ^{13}C nutation experiments performed on the previous U-^{13}C,^{15}N-labeled glycine sample. The ^{1}H nutation experiment was performed by including an evolution period at the beginning of a (H)C CP experiment. A low power nutation pulse was applied on the evolution period before the 90° pulse and CP, and was incremented as the indirect dimension. The spectrum is shown in Fig. 1.19. The correspondence of proton power level and nutation frequency was then determined by extracting the distance

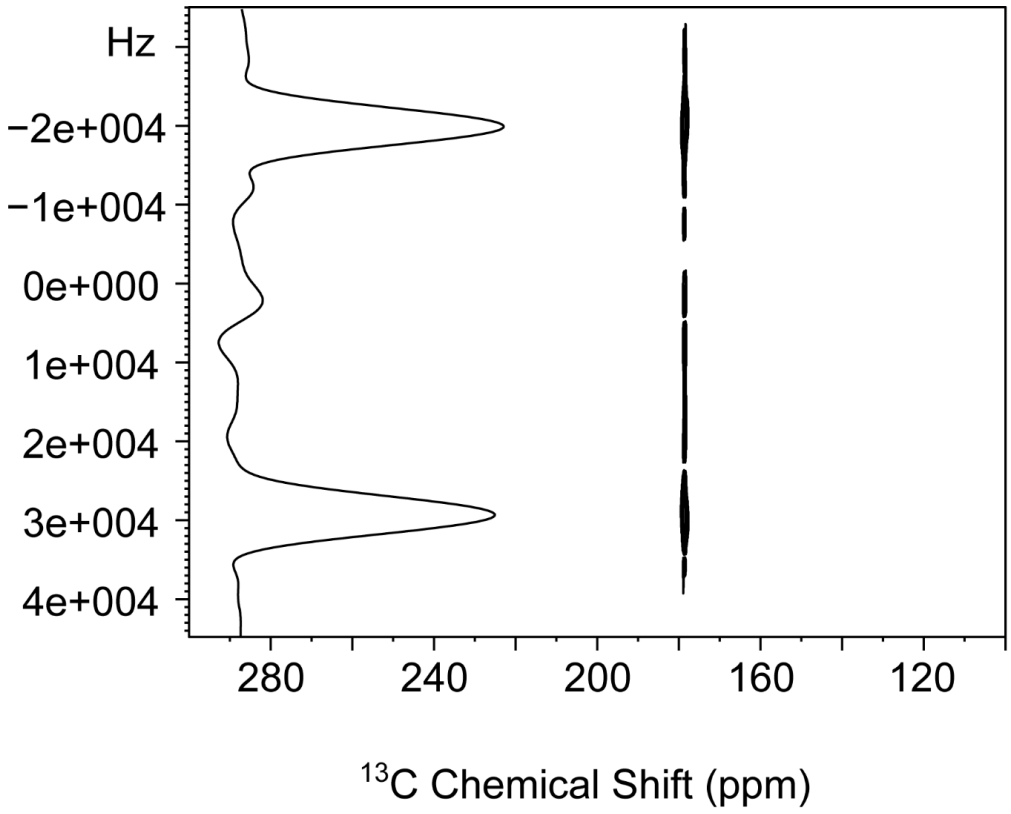

Figure 4.20. ^{13}C nutation frequency 2D spectrum acquired on U-^{13}C,^{15}N-labeled glycine, with HC CP condition optimized on C' The corresponding effective nutation frequency of the carbon power was quantified by measuring half of the distance between the two peaks in the indirect dimension.

between the two C' peaks in the indirect dimension. Similar nutation experiment was also performed for C', with nutation period of a low power carbon nutation pulse right after CP. Z-filter[35] followed the nutation period for pure phase detection. Based on the measured nutation frequencies and further scans of CP power directly performed on GB1 samples, the CP match condition was established between carbon and proton at $2/5\omega_r$ H and $3/5\omega_r$ C at the DQCP condition, and $5/3\omega_r$ H and $2/3\omega_r$ C at the ZQCP condition, with ω_r denoting MAS rate (50 kHz). C^{α} and C' were treated separately by switching the ^{13}C offset center in each case. The analysis of HC CP efficiency is included in the table below.

The (HC)N DCP experiments are in general much less effective than the direct (H)N transfer. For the deuterated sample, this can be interpreted as the difficulty of CP at longer distances for ^{1}H-^{13}C in comparison with the directly attached ^{1}H-^{15}N pairs. To our surprise, the (HCA)N correlation experiment at DQCP condition gave much worse signal to noise ratio (S/N = 3.2) than the (HCO)N correlation (S/N = 5.5) with the DCN GB1 sample. Although the number of scans doubled in the measurements with transfer through C^{α} (ns = 128) than through C' (ns = 64), the result lead to a lower S/N (Table 4.1). One

Table 4.1. Signal to noise ratios (S/N) estimated for the influence of proton-carbon CP condition, carbon position, and deuteration on the DCP transfer efficiency.

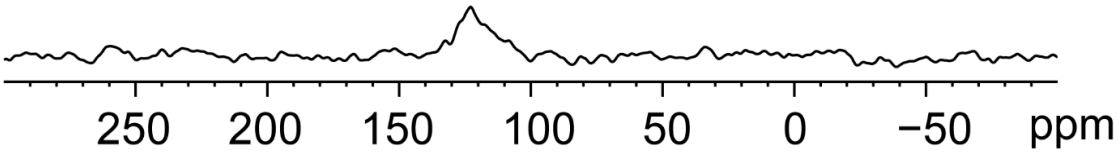

Sample	[d]ns	[c]S/N	Correlation	CP Condition
[a]DCN GB1	16	**9.3**	(H)N	DQCP
DCN GB1	64	**5.5**	(HCO)N	DQCP
DCN GB1	128	**3.2**	(HCA)N	DQCP
[b]CN GB1	128	**5.6**	(HCO)N	DQCP
CN GB1	128	**3.7**	(HCA)N	DQCP
DCN GB1	128	**4.3**	(HCO)N	ZQCP
DCN GB1	128	**4.1**	(HCA)N	ZQCP
CN GB1	128	**4.1**	(HCO)N	ZQCP
CN GB1	128	**3.7**	(HCA)N	ZQCP

[a] Uniformly-^{2}H,^{13}C,^{15}N-labeled GB1 back-exchanged in $^{1}H_2O$.
[b] Uniformly-^{13}C,^{15}N-labeled GB1 (no deuteration).
[c] Signal to noise ratio was calculated with the command 'SINOCAL 150 100 80 -50 100' in the Topspin 3.0 software (Bruker BioSpin, Germany). The resulting ^{15}N DCP spectrum of (H)N experiment is shown above the table. Linebroadening of 200 Hz was applied for complete capture of ^{15}N resonance intensities.
[d] The number of transients coadded in the time domain before producing the spectrum.

assumption could be the necessity for deuterium decoupling, which was not implemented in these experiments. On the other hand, the DQCP of HC transfers implemented in the DCP experiments for CN GB1 gave similar results, with (HCO)N more effective (S/N=5.6) than the (HCA)N transfer (S/N=3.7). However, deuterium is not presented in this case. And instead C^{α}'s were directly attached to protons. From the T_2' studies in Fig. 4.9 and Fig. 4.10, we can conclude that it is more difficult for C^{α} than C' to decouple from proton. And the less effective proton decoupling might contribute to the less effectiveness during the SPCP transfer, resulting in the total lower efficiency during DCP through C^{α}. ZQCP studies on both DCN GB1 and CN GB1 sample with DCP through C^{α} and through C' produced very similar results (S/N = 4.0 ±0.3). And the S/N ratio were at the lower end in all these four cases (last four rows in Table 4.1). Of all the eight DCP experiments, the (HCO)N correlation produced a S/N roughly twice of the other DCP choices. The correlation experiment would potentially be more effective than in other cases when building a 3D (H)CONH correlation experiment, requiring less experimental time.

4.4 Conclusion

Heteronuclear decoupling performance and CP conditions are important components for the design of multidimensional correlation techniques. The T_2' studies at various MAS rates provide optimum XiX decoupling power and spinning speeds for both 2.5 mm rotor and 1.3 mm rotor applications when T_2' is a limiting parameter. The application of proton-detected-HN correlation experiments can help improve resolution by taking advantage of the sensitive ^{1}H chemical shifts. The variable CP time implemented in the correlation method are potentially very useful in determining important distances at

atomic scale. Different CP conditions achieved by using the GB1 samples helped us examine various choices for effective multidimensional correlation techniques possible for solving the structure of tryptophan synthase. In cases when the amount of sample appears to be the limiting parameter, the 1.3 mm rotor would be very useful in providing ^{1}H chemical shifts in solid-state, and help us understand the behavior of acquisition at very fast MAS speed. When sensitivity becomes even more demanding than the availability of protein sample, the 2.5 mm rotor can be used, which still grants reasonable T_2' for ^{13}C and ^{15}N in solid-state, while providing a larger amount of sample available for detection.

4.5 References

(1) Barbet-Massin, E.; Felletti, M.; Schneider, R.; Jehle, S.; Communie, G.; Martinez, N.; Jensen, M. R.; Ruigrok, R. W. H.; Emsley, L.; Lesage, A.; Blackledge, M.; Pintacuda, G. *Biophys. J.* **2014**, *107*, 941–946.

(2) Barbet-Massin, E.; Pell, A. J.; Retel, J. S.; Andreas, L. B.; Jaudzems, K.; Franks, W. T.; Nieuwkoop, A. J.; Hiller, M.; Higman, V.; Guerry, P.; Bertarello, A.; Knight, M. J.; Felletti, M.; Le Marchand, T.; Kotelovica, S.; Akopjana, I.; Tars, K.; Stoppini, M.; Bellotti, V.; Bolognesi, M.; Ricagno, S.; Chou, J. J.; Griffin, R. G.; Oschkinat, H.; Lesage, A.; Emsley, L.; Herrmann, T.; Pintacuda, G. *J. Am. Chem. Soc.* **2014**.

(3) Franks, W. T.; Zhou, D. H.; Wylie, B. J.; Money, B. G.; Graesser, D. T.; Frericks, H. L.; Sahota, G.; Rienstra, C. M. *J. Am. Chem. Soc.* **2005**, *127*, 12291.

(4) Moseley, H. N. B.; Sperling, L. J.; Rienstra, C. M. *J. Biomol. NMR* **2010**, *48*, 123–128.

(5) Zhou, D. H.; Shah, G.; Cormos, M.; Mullen, C.; Sandoz, D.; Rienstra, C. M. *J. Am. Chem. Soc.* **2007**, *129*, 11791–11801.

(6) Zhou, D. H.; Shea, J. J.; Nieuwkoop, A. J.; Franks, W. T.; Wylie, B. J.; Mullen, C.; Sandoz, D.; Rienstra, C. M. *Angew. Chem. Int. Ed. Engl.* **2007**, *46*, 8380–8383.

(7) Schmidt, H. L. F.; Sperling, L. J.; Gao, Y. G.; Wylie, B. J.; Boettcher, J. M.; Wilson, S. R.; Rienstra, C. M. *J. Phys. Chem. B* **2007**, *111*, 14362–14369.

(8) Tang, M.; Comellas, G.; Mueller, L. J.; Rienstra, C. M. *J. Biomol. NMR* **2010**, *48*, 103–111.

(9) Detken, A.; Hardy, E. H.; Ernst, M.; Meier, B. H. *Chem. Phys. Lett.* **2002**, *356*, 298–304.

(10) Vinogradov, E.; Madhu, P.; Vega, S. *Chem. Phys. Lett.* **2000**, *329*, 207–214.

(11) Ye, T.; Chen, L.; Niks, D.; Kaiser, J. M.; Lai, J.; Rienstra, C. M.; Dunn, M. F.; Mueller, L. J. *Phys. Chem. Chem. Phys.* **2009**, *11*, 6875.

(12) Thiriot, D. S.; Nevzorov, A. a; Zagyanskiy, L.; Wu, C. H.; Opella, S. J. *J. Mol. Biol.* **2004**, *341*, 869–879.

(13) Park, S. H.; Marassi, F. M.; Black, D.; Opella, S. J. *Biophys. J.* **2010**, *99*, 1465–1474.

(14) Ernst, M.; Geen, H.; Meier, B. H. *Solid State Nucl. Magn. Reson.* **2006**, *29*, 2–21.

(15) Thurber, K. R.; Tycko, R. *J. Magn. Reson.* **2009**, *196*, 84–87.

(16) Marchetti, A.; Jehle, S.; Felletti, M.; Knight, M. J.; Wang, Y.; Xu, Z.-Q.; Park, A. Y.; Otting, G.; Lesage, A.; Emsley, L.; Dixon, N. E.; Pintacuda, G. *Angew. Chemie* **2012**, *124*, 10914–10917.

(17) Paluch, P.; Pawlak, T.; Amoureux, J.-P.; Potrzebowski, M. J. *J. Magn. Reson.* **2013**, *233*, 56–63.

(18) Stejskal, E.; Schaefer, J.; Waugh, J. S. **1977**, *12*.

(19) Detken, A.; Hardy, E. H.; Ernst, M.; Meier, B. H. *Chem. Phys. Lett.* **2002**, *356*, 298–304.

(20) Marion, D.; Ikura, M.; Bax, A. Improved solvent suppression in one- and two-dimensional NMR spectra by convolution of time-domain data. *Journal of Magnetic Resonance (1969)*, 1989, *84*, 425–430.

(21) Delaglio, F.; Grzesiek, S.; Vuister, G. W.; Zhu, G.; Pfeifer, J.; Bax, A. *J. Biomol. NMR* **1995**, *6*, 277–293.

(22) Franks, W. T.; Zhou, D. H.; Wylie, B. J.; Money, B. G.; Graesser, D. T.; Frericks, H. L.; Sahota, G.; Rienstra, C. M. *J. Am. Chem. Soc.* **2005**, *127*, 12291–12305.

(23) Ramachandran, R.; Bajaj, V. S.; Griffin, R. G. *J. Chem. Phys.* **2005**, *122*, 164503.

(24) Ernst, M.; Samoson, A.; Meier, B. H. *J. Magn. Reson.* **2003**, *163*, 332–339.

(25) Oas, T. G.; Griffin, R. G.; Levitt, M. H. *J. Chem. Phys.* **1988**, *89*, 692.

(26) Scholz, I.; van Beek, J. D.; Ernst, M. *Solid State Nucl. Magn. Reson.* **2010**, *37*, 39–59.

(27) Chen, L.; Kaiser, J. M.; Polenova, T.; Yang, J.; Rienstra, C. M.; Mueller, L. J. *J. Am. Chem. Soc.* **2007**, *129*, 10650–10651.

(28) Nielsen, N. C.; Bildsoe, H.; Jakobsen, H. J.; Levitt, M. H. *J. Chem. Phys.* **1994**, *101*, 1805.

(29) Ernst, M.; Samoson, A.; Meier, B. H. *J. Chem. Phys.* **2005**, *123*, 64102.

(30) Schiksnis, R. a; Bogusky, M. J.; Tsang, P.; Opella, S. J. *Biochemistry* **1987**, *26*, 1373–1381.

(31) Park, S. H.; Yang, C.; Opella, S. J.; Mueller, L. J. *J. Magn. Reson.* **2013**, *237C*, 164–168.

(32) Van Rossum, B. J.; De Groot, C. P.; Ladizhansky, V.; Vega, S.; De Groot, H. J. M. *J. Am. Chem. Soc.* **2000**, *122*, 3465–3472.

(33) Demers, J.-P.; Chevelkov, V.; Lange, A. *Solid State Nucl. Magn. Reson.* **2011**, *40*, 101–113.

(34) Baldus, M.; Petkova, A. T.; Herzfeld, J.; Griffin, R. G. *Mol. Phys.* **1998**, *95*, 1197–1207.

(35) Sorensen, W.; Rance, M.; Ernst, R. R. **1984**, *534*.

Chapter 5

Symmetry Breaking Mechanism for the Photoinduced Expansion of Anthracene Ester Molecular Crystal Nanorods

5.1 Introduction

The ability to generate large mechanical displacements using light makes photomechanical materials a promising way to make light-controlled actuators and devices. These materials take advantage of photochemical reactions to convert photon energy directly into mechanical work. In order to generate useful amounts of motion and force, ordered assemblies of photoreactive subunits must be utilized.[1] For example, the cis-trans photoisomerization of azobenzene molecules embedded in liquid crystal polymers can drive dramatic light-induced bending and curling.[2,3] Molecular crystals have also attracted recent attention as dynamic entities,[4,5] and crystals composed of photoreactive molecules have been shown to undergo photoinduced shape changes, like bending, coiling, and twisting, and jumping.[6–18] In most cases, these dramatic shape changes rely on the formation of a bimorph structure, where interfacial stress between spatially distinct regions of reactant and photoproduct drives the deformation.[19–22] This mechanism for generating photomechanical motion requires generating an asymmetric spatial mixture of reactant and product molecules within the crystal. If the crystal is very small, the generation of asymmetric product and reactant spatial distributions becomes problematic. First, the diffraction limit of light limits the experimenter's ability to illuminate only one part of the structure. Second, the lack of light attenuation in small structures means that all regions react at the same rate, preventing the buildup of products on one side.

Rather than relying on the bimorph mechanism, a second approach is to convert 100% of the reactant crystal to the photoproduct. This would ideally lead to a Martensitic phase transition in which the product molecules rearrange while maintaining their relative positions, similar to what is observed in metallic shape-memory alloys.[23] The new photoproduct crystal will have different dimensions from the reactant crystal, leading to net motion as the crystal assumes its new shape. This approach simplifies the irradiation requirements, since it only requires that the light exposure be of sufficient duration to react the entire crystal. One challenge for this approach is that photochemically induced crystal-to-crystal phase transitions invariably produce internal strain which can lead to fracture.[24] To minimize fracture, one can look for reactant and product crystals that have similar dimensions. But while similar crystal dimensions can help the crystal remain intact during reaction, one might also expect that they would preclude the generation of large crystal shape changes.

The use of micro- or nanocrystals often permits the use of photochemical reactions with large shape changes because dissipation of strain at surfaces enables single-crystal-to-single-crystal transformations even in cases where larger crystals shatter.[25–27] The photodimerization of 9-tertbutyl-anthracene ester (**9TBAE**), illustrated in Fig. 5.1, is a good example of such a reaction. In 2006, we demonstrated that nanorods composed of **9TBAE** could expand by up to 15% upon irradiation.[26] This dimensional change was about one order of magnitude larger than those previously seen in single-crystal-to-single-crystal transformations, but could only be obtained for very small crystals. Larger crystals simply shattered under illumination.

The exact mechanism of **9TBAE**'s large photomechanical response was not immediately clear. Subsequent experiments on **9TBAE** and related esters showed that the photodimer product crystal was a metastable intermediate, denoted the "solid-state reacted dimer" (SSRD). The SSRD has a considerably different structure from that of the equilibrium dimer crystal obtained from solution growth (the "solution grown dimer" or SGD).[28] Lack of knowledge about the SSRD crystal structure prevented us from being able to quantitatively connect molecular-level rearrangements to larger scale changes in crystal shape.

In the present work, we return to the problem of how to connect the photoinduced changes in molecular structure and packing to the expansion of the crystalline nanorods. Using a combination of powder x-ray diffraction (PXRD), solid-state nuclear magnetic resonance (SSNMR), and computational modeling – an approach often referred to as NMR crystallography or NMR-assisted crystallography[29–38] – we determine the crystal structure of the SSRD intermediate. We find that the SSRD crystal unit cell and volume are quite similar to those of the monomer crystal. This is surprising in light of the large expansions observed for the crystalline nanorods. Fortunately, knowledge of the SSRD structure also

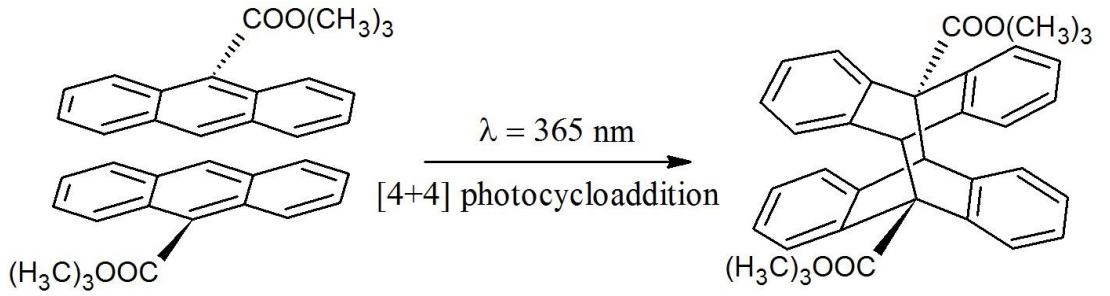

Figure 5.1. [4+4] photocycloaddition reaction scheme of **9TBAE.**

allows us to determine the orientation of the photodimer crystal relative to the monomer starting point. We find that the key to understanding the large expansion of the **9TBAE** nanorods is a photoinduced reorientation of the dimer unit cell within the rod, as opposed to a simple expansion of the unit cell. For **9TBAE**, two orientations of the photoproduct unit cell can arise from the initial monomer cell because the monomer crystal has two sublattices, and photoisomerization induces a symmetry breaking event that forces the molecules to choose between the orientations of these sublattices. One orientation leads to a 2% contraction, while the other leads to a 16% expansion. Based on our observations, the rods have a random mixture of these two dimer crystal reorientations.

The results of this work show that simple concepts about crystal expansion due to volume changes need to be augmented by more subtle considerations about how crystal domains are oriented within a specific structure. These insights suggest new strategies for generating large deformations after a photochemical reaction.

5.2 Experimental Section

5.2.1 Powder X-ray Diffraction (PXRD)

Powder X-ray diffraction (PXRD) data were collected on a Bruker D8 Advance X-ray powder diffractometer (CuK radiation, l = 1.5418 Å, 40KV/40mA power) at 296 K.

5.2.2 Solid State Nuclear Magnetic Resonance (SSNMR)

SSNMR experiments were performed at 14.1 T (600.01 MHz ^{1}H, 150.87 MHz ^{13}C) on a Bruker AV600 spectrometer using samples at natural abundance ^{13}C isotopomer concentration. Two-dimensional ^{1}H,^{13}C hetoronuclear-correlation (HETCOR)[39] spectra were acquired on a triple resonance 1.3 mm magic angle spinning (MAS) probe with a sample spinning rate of 50 kHz (±2 Hz). Less than 2 mg of microcrystalline sample were packed into each rotor. For these experiments, cross polarization (CP) was established using a 2 ms contact time with nutation frequencies of 125 kHz for ^{1}H and 75 kHz for ^{13}C; high power ^{1}H decoupling during ^{13}C acquisition was implemented using XiX (125 kHz, 2.85 τ_r).[40]

Two-dimensional isotropic-anisotropic chemical shift correlation spectra[41–44] were measured using the TOSS-t1-deTOSS approach of Kolbert and Griffin[41] modified in the following manner: (1) cogwheel phase cycling[45] was implemented for the 8 π pulses

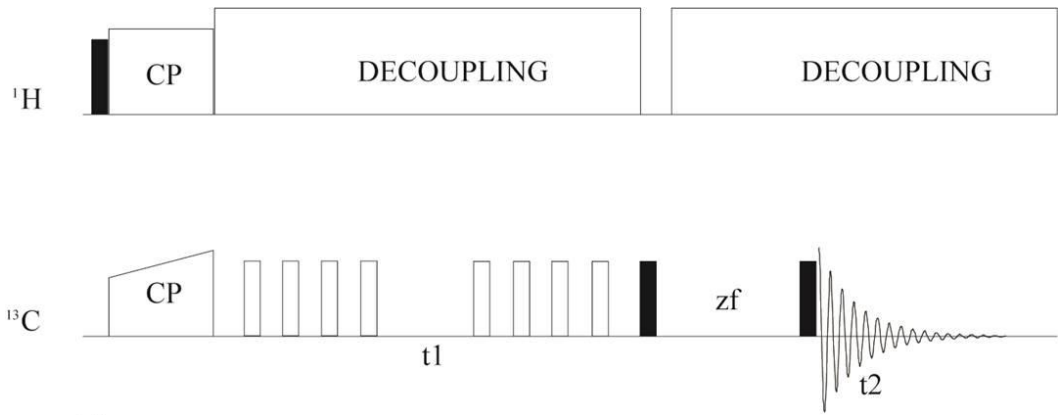

Figure 5.2. The TOSS-deTOSS pulse sequence.13 White boxes represent 180° pulses, and black boxes represent 90° pulses. The implementation of the Cog-wheel phase cycling14 will be demonstrated in a separate paper. The phase cycling utilized here is COG16(0,1,0,1,0,1,0,1,0;0) following Levitt's convention.

comprising the TOSS and deTOSS periods; (2) a Z-filter was applied at the end of the deTOSS period to combine the ±1 magnetization coherence pathways from the t1 evolution period and allow for pure phase detection.[46] These experiments were performed on a 4 mm double resonance MAS probe with samples spinning at 2 kHz; cross-polarization was implemented using spin locking fields of 40 kHz on ^{1}H and 38 kHz on ^{13}C with a 2 ms

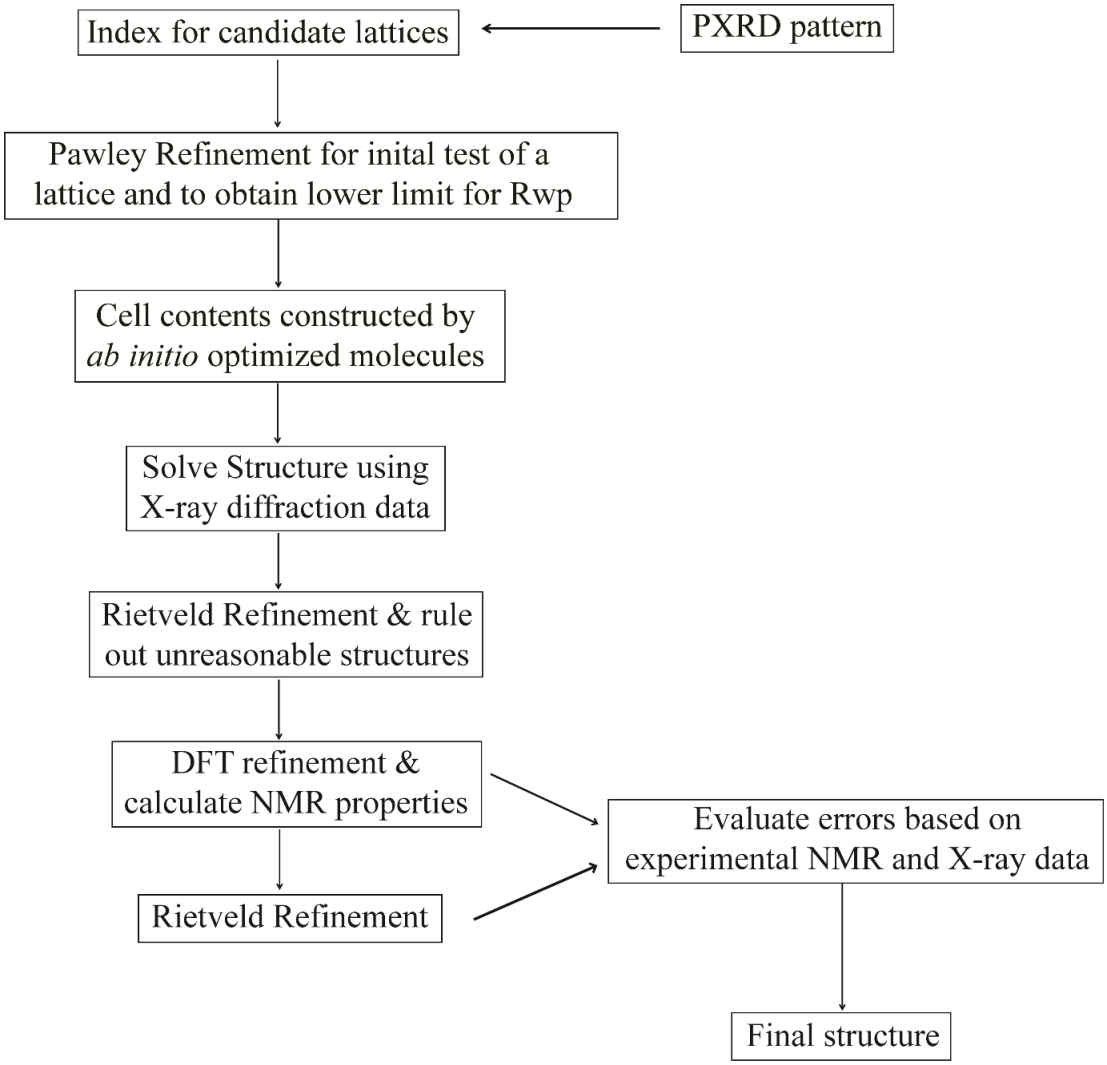

Figure 5.3. Workflow for the crystal structure determination of SSRD (solid-state reacted dimer), following the general schemes outlined by previous workers in the field.[49,50,89,90]

contact time; other RF powers were 83 kHz ^{1}H (excitation and decoupling) and 50 kHz ^{13}C (π and $\pi/2$ pulses).

Chemical shifts were indirectly referenced to neat TMS using an external sample of adamantane in which the ^{1}H resonance was set to 1.87 ppm[36] and the downfield ^{13}C peak to 38.48 ppm.[47]

5.2.3. Computational Analysis

All computations were performed using Materials Studio software.[48] The workflow (Supporting Information, Figure S1) for the structural refinement follows the general schemes outlined by previous workers in the field.[39,49–51]

5.2.3.1. Structure Prediction

The PXRD pattern of the SSRD was indexed using the Reflex X-Cell program.[52] Based on the raw PXRD spectrum (with 2θ angles ranging from 5° to 40°), nine candidates were generated using the X-Cell code for all potential crystal systems. Pawley refinement was used to generate peak lineshapes and the background baseline for these predicted cells in order to compare with experiment.[53] With these potential cells identified, the packing and relative orientations of SSRD molecules within the unit cells were optimized using the Reflex Powder Solve program.[54,55] SSRD molecules were first geometry optimized in gas phase before insertion into the unit cell. Finally the Powder Solve code searched through molecular translational, rotational, and torsional (torsion angles C12-C13-C15-O1 and C15-O2-C16-C17) degrees of freedom, until crystal structures converged to the experimental PXRD pattern.

5.2.3.2. Structure Validation Using PXRD

After Powder Solve, Rietveld refinement[56] generated a weighted profile R-factor (R_{wp}) for each candidate that indicates both the quality of the fit of the predicted cells relative to experiment and the noise level of the PXRD pattern.[57] The best of the nine candidates achieved an R_{wp} of 16.66%. Of the other candidate cells (Supporting Information), the second lowest R_{wp}, 29.10%, came from a triclinic cell. This crystal structure was overpacked (with a density of 1.75 g/cm^3), and was not able to converge upon further DFT geometry optimization. The other seven candidates resulted in R_{wp}'s ranging from 39.62% to 70.18%, and had obvious deviations from the SSRD PXRD pattern.

For the best-fit orthorhombic crystal system, all orthorhombic space groups were then explored using Powder Solve. These structures were subsequently DFT geometry optimized using CASTEP.[58] Chemical shielding tensors were then calculated for comparison with experimental NMR results.

5.2.3.3. CASTEP DFT Calculations[58–64]

Geometry optimization was performed using *CASTEP* to refine the possible candidate crystal structures of the orthorhombic space groups. The Perdew-Burke-Ernzerhof (PBE)[65] functional was employed, using an ultrasoft pseudopotential basis set.[66] The "ultra-fine" level was selected with a planewave cut-off energy of 800 eV, a k-point spacing of 0.071 Å^{-1} and a SCF convergence level of 5×10^{-7} eV atom^{-1}. The BFGS (Broyden, Fletcher, Goldfarb, and Shanno) minimization algorithm was used.[67] The optimizations were performed with cell dimensions fixed from the PXRD predicted structures.

5.2.3.4. SSNMR Analysis of Candidate Structures

Calculated NMR chemical shieldings were converted to chemical shifts according to the equation $\delta = (\sigma - \sigma_{ref})/m$, where δ and σ represents shift and shielding respectively and appropriate values for m and σ_{ref} taken from previous studies.[36,68] While ideally m = -1, systematic errors arise in first principles calculations of shielding due to approximations inherent to the level of theory and basis set choice. The linear rescaling given above, however, has been shown to be quite effective in allowing an accurate and precise conversion of calculated shielding and experimental shift.[60,61] For ^{13}C, we use the values of Johnston et al[68] who surveyed 14 organic crystals and determined that for carbohydrates m=-1.139 and σ_{TMS}=177.9 ppm (RMSD = 1.88) and for aromatics m=-1.041 and

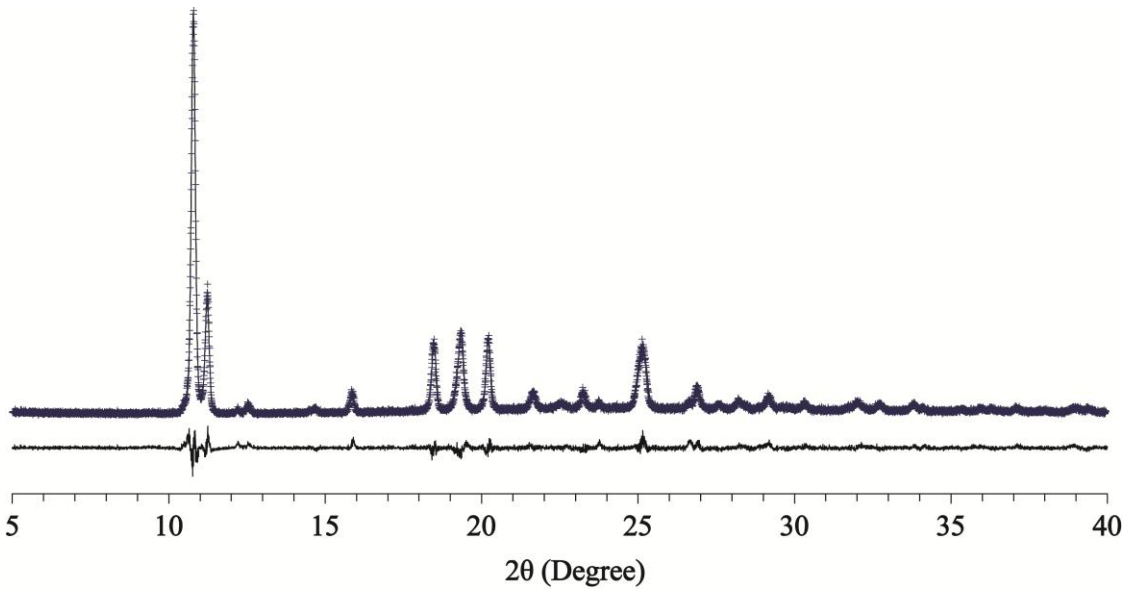

Figure 5.4. Comparison of the SSRD PXRD pattern with that calculated for the *Pccn* structure.The dark blue line is the calculated PXRD pattern, overlaid with experimental data points (crosses). The difference between experimental and calculated is shown as the black line below them. The final R_{wp} is 15.42% after geometry optimization using CASTEP. If no CASTEP refinements were performed, the R_{wp} was 16.66%.

Table 5.1. 'Best' candidates suggested by the X-Cell program when all 15 well identified peaks were used for indexing. Only the orthorhombic *Pccn* candidate has an R_{wp} of lower than 20% after Rietveld refinement.

#	Rel. FOM	Peaks Found	System	Volume	Extinction Class
1	1.009	14 of 15	Orthorhombic	2.27E+03	*Pmma*
2	0.821	14 of 15	Orthorhombic	3.01E+03	***Pccn***
3	0.636	15 of 15	Triclinic	1.01E+03	*P1*
4	0.458	14 of 15	Triclinic	675.16	*P1*
5	0.416	15 of 15	Triclinic	1.08E+03	*P1*
6	0.413	15 of 15	Monoclinic	2.29E+03	*C2*
7	0.221	15 of 15	Triclinic	979.25	*P1*
8	0.215	15 of 15	Triclinic	1.06E+03	*P1*
9	0.185	14 of 15	Triclinic	531.33	*P1*

σ_{TMS}=176.5 ppm (RMSD = 3.05). For ^{1}H, we use the values of Salager et al, with m=-1 and σ_{TMS} =31.18 ppm.[36]

5.3 Results

5.3.1. Determination of the SSRD Crystal Structure

The main challenge in understanding how photodimerization leads to nanorod expansion lies in determining the crystal structure of the metastable SSRD product crystal. This photodimer crystal phase is only accessible via photochemical reaction of the monomer crystal, but the large geometry changes that accompany this reaction led to crystal disintegration. This made it impossible to determine the SSRD structure using single crystal XRD experiments, although we were able to obtain PXRD and SSNMR data on the crystalline powder.[69] Those results clearly showed that the SSRD structure was different from the low energy SGD crystal. But we were unable to conclusively establish the exact nature of the molecular packing in the SSRD crystal. In this paper, we take

advantage of advances in computational methods for the analysis of the PXRD data and structural optimization. In principle, the PXRD pattern by itself should be sufficient to solve the crystal structure, but the low number of peaks and limited signal-to-noise ratio made it prudent to use NMR in conjunction with computational methods to confirm the results.

The procedure for determining SSRD crystal structure is outlined in Fig. 5.3. The PXRD pattern of the SSRD was indexed using the *Reflex X-Cell* program.[52] The *X-Cell* code was preferred here for two reasons. First the program enables customized tolerance of impurities. This is helpful for the photoreaction intermediate, because of the possible existence of **9TBAE** monomer reactant. Secondly, systematic absence was considered.

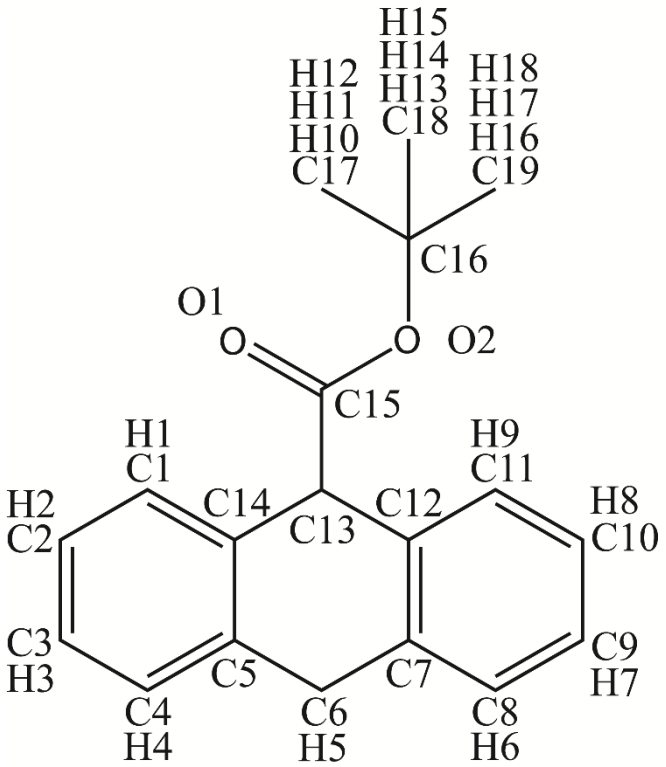

Figure 5.5. Numbering for the **9TBAE** SSRD half molecule. The carbon numbering is the same as **9TBAE** monomer in a previous work.

This can result in the correct cell being identified at an earlier stage, increasing the possibility of avoiding the feasibility limit. Initial peaks were selected using a background removed and smoothed PXRD pattern. Then the *X-Cell* code explored the search space using full profile fitting against the entire raw PXRD spectrum of 2θ angles from 5° to 40°. The nine candidates generated are shown in Table 5.1.

Pawley refinement was then used to refine and the calculated peak shapes and background of these predicted cells using the experimental PXRD spectrum as a reference.[53] The agreement of a predicted cell with the experimental PXRD spectrum was quantified as R_{wp}. The achieved R_{wp}'s of these 'empty boxes' set the lower limit for R_{wp}'s after the molecules were inserted into the cells. After Pawley refinement (Fig 5.6), eight of the nine candidates reported the R_{wp}'s ranging from 14.19% to 20.25%, with the other

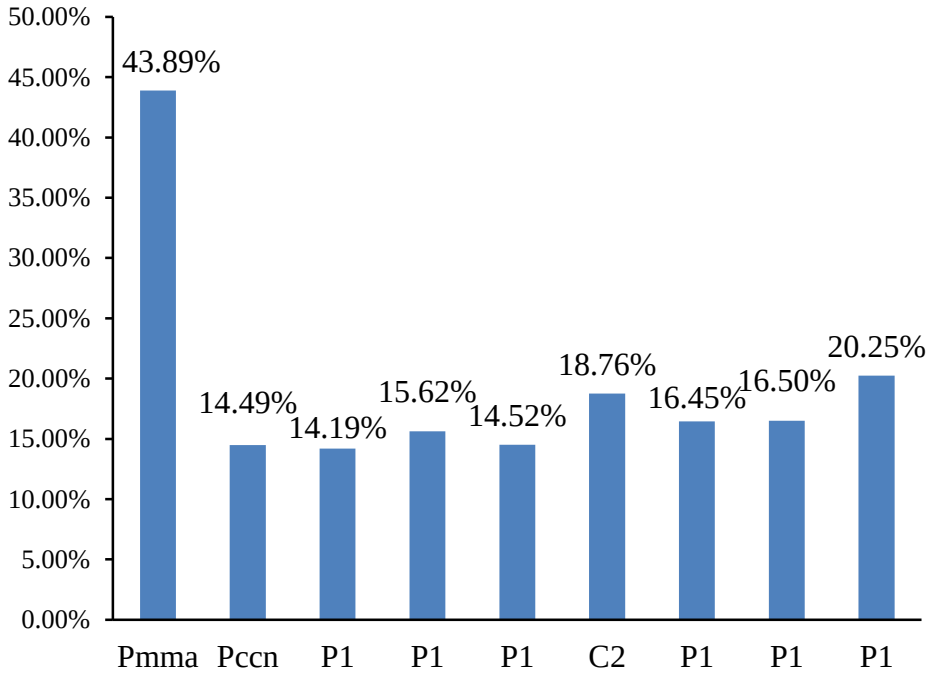

Figure 5.6. Pawley refinement results for the nine cells predicted by the *X-Cell* program. The R_{wp}'s are marked at the top of each cell with its associated space group.

candidate having an R_{wp} of 43.89%. For the organic photoreaction intermediate, the lowest possible R_{wp} value was about 14% due to the level of background noise.[57] Although one of the candidates strongly deviated from the observed PXRD pattern (43.89% R_{wp}), all were submitted for further PXRD analysis (Reflex Powder Solve and Rietveld Refinement).

The *Reflex Powder Solve* program optimized the molecular translational and rotational degrees of freedoms, and the torsion angles C12-C13-C15-O1 and C15-O2-C16-C17 (atom numbering shown in Figure 5.5).[54,55] The SSRD molecule was first geometry optimized in the gas phase using the PBE functional and Gaussian double zeta plus polarization function basis set (DNP). Then simulated annealing was used to optimize the

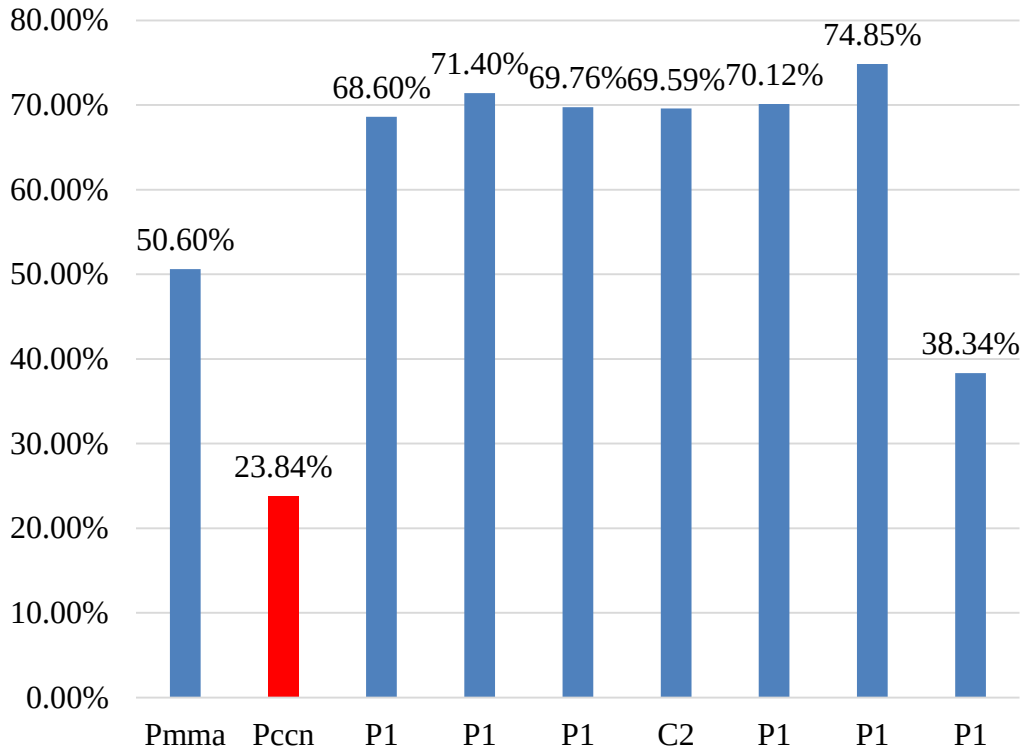

Figure 5.7. *Powder Solve* R_{wp}'s of the nine candidates predicted by X-Cell, with molecules introduced in, and molecular translational, rotational, and torsional degrees of freedom optimized against PXRD pattern.

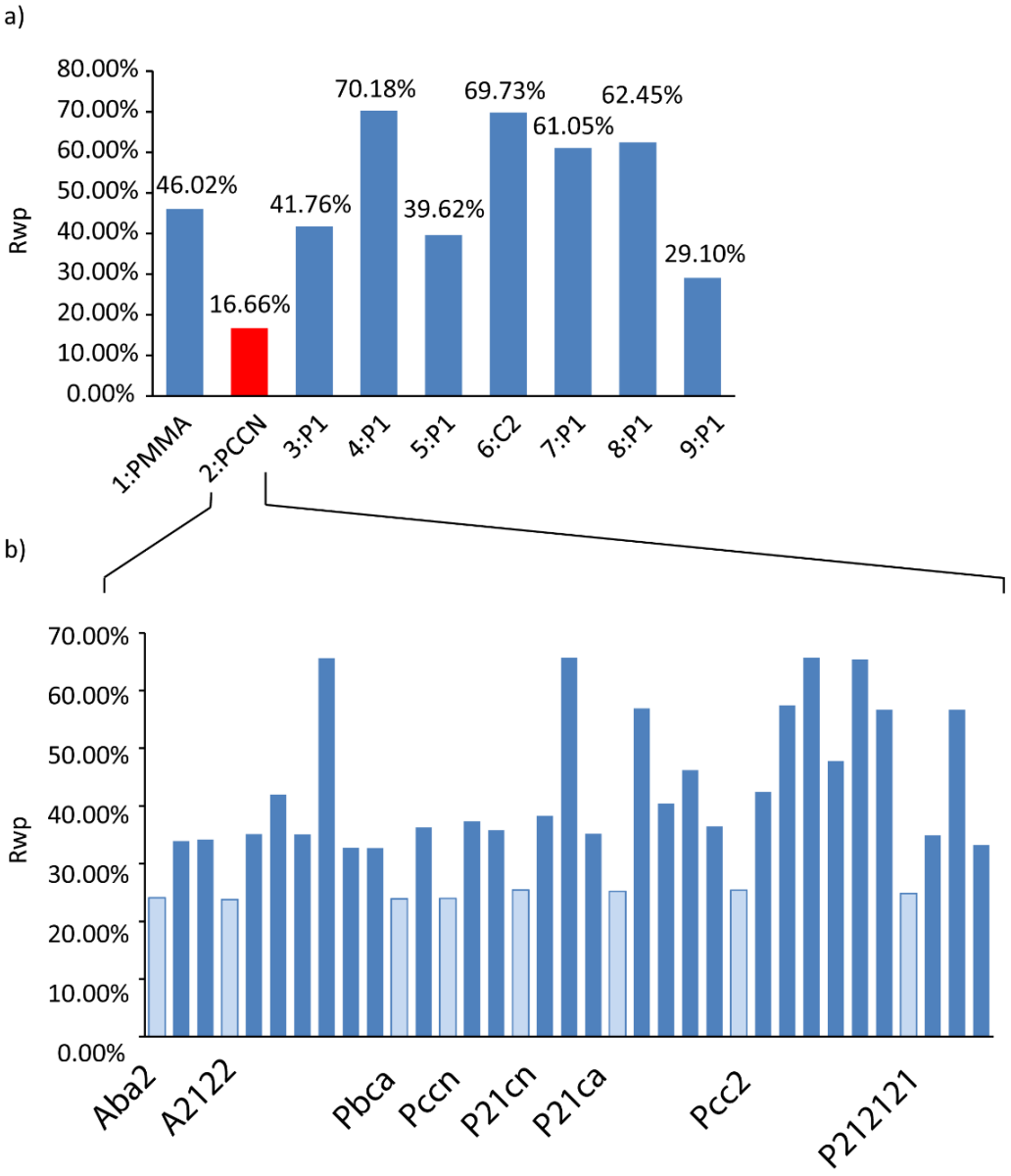

Figure 5.8. a) Rietveld Refinement Rwp's of the candidates as listed in Table 5.1, after cells underwent *Powder Solve*. The orthorhombic Pccn cell has a lowest Rwp of 16.7%. b) Rwp's after simulated annealing using Powder Solve. All orthorhombic space groups (International Table Number 16 to 74) were searched using the optimized cell parameters. Space groups giving a positive figure of merit were then further refined using Powder Solve. The results are listed as a histogram, ordered by figure of merit from the indexing program, with the most possible suggested structure starting on the left. Eight space groups produced similar low Rwp's, as shown in lighter blue. After Rietveld refinement, the Rwp's of these structures were at around 17%. They were DFT refined afterwards.

arrangement of molecules in the unit cell. The number of steps and annealing temperature were kept at the default 'automatic' (varied according to the number of degrees of freedom), with the number of annealing cycles set at 200 for an extensive coverage of the search space. The PXRD profiles (peak shape and background) were the same as those obtained from the previous Pawley refinements. One best match (lowest R_{wp}) to the PXRD pattern was achieved for each candidate cell after the *Powder Solve* process. After *Powder Solve*, the peak shape and background information were refined using the Rietveld refinement[56] method, with final R_{wp} results shown in Fig 5.8(a).

One cell of the orthorhombic crystal system (of space group *Pccn*) achieved an R_{wp} of 16.66%. 'Search Space Group' was then performed on the candidate cell for all the orthorhombic space groups (International Table number 16 - 74). These possibilities were explored using the same *Powder Solve* and Rietveld refinement setup as described previously. Seven additional orthorhombic space groups besides *Pccn* produced similar R_{wp}'s (ranging from 17.62% to 18.69%) with the same cell parameters (Fig. 5.8(b)). The original *Pccn* candidate and these seven orthorhombic alternatives were then DFT geometry optimized using *CASTEP*. Chemical shielding tensors were also calculated after the geometry optimization for comparison with experimental NMR results.

5.3.2. Refinement of Structure Using NMR Crystallography

The combination of solid-state NMR spectroscopy with first principle computation of chemical shieldings has developed into a powerful approach for screening and ranking potential crystal structures that result from diffraction-based methods. Here we make use of this general approach, often referred to as "NMR crystallography" or "NMR-assisted

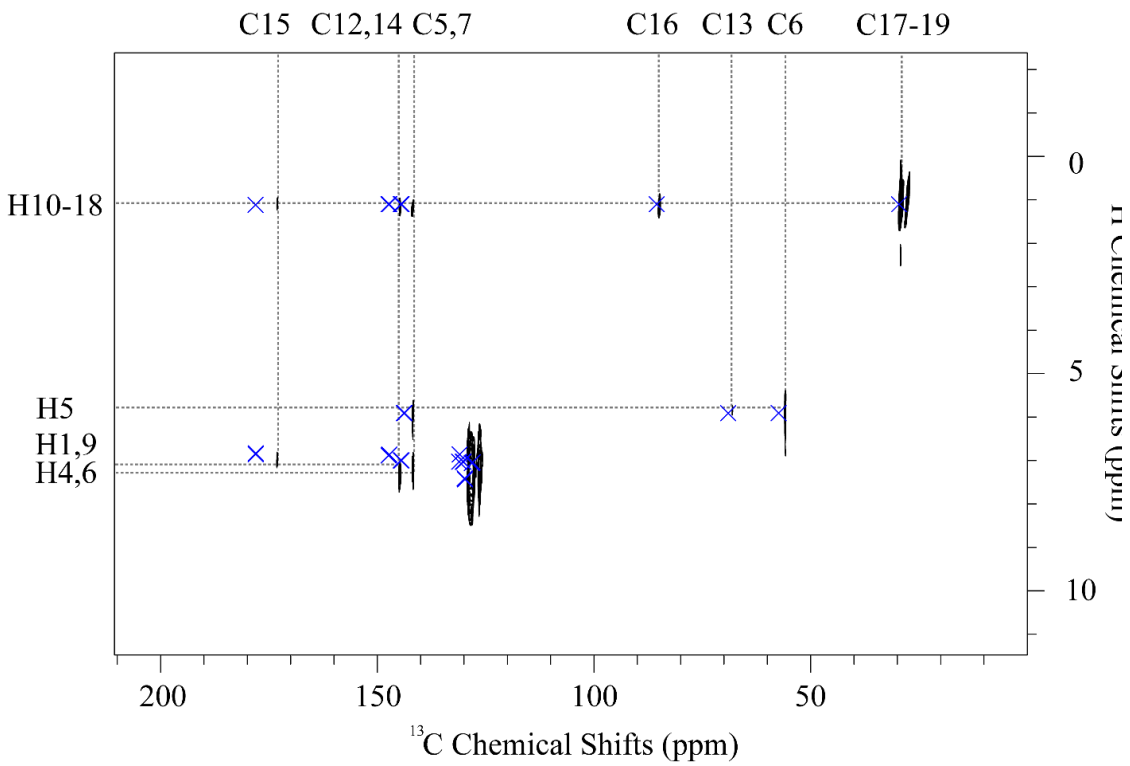

Figure 5.9. HETCOR experiment performed on SSRD, with NMR-CASTEP computed chemical shifts overlaid as X's. Chemical shifts assignments are indicated as dash lines, with labels on the sides. After geometry optimization using *CASTEP*, χ^2 was reduced to 0.80.

crystallography," to test for consistency between the eight solutions of the SSRD structure above and SSNMR observables. First, ^{1}H and ^{13}C isotropic chemical shifts and ^{13}C chemical shift tensors values were measured in the solid-state. Second, both isotropic and tensor quantities were used to examine the *DFT* predicted values from *CASTEP* for the calculated SSRD candidates.

Fig. 5.5 shows our carbon numbering convention for the **9TBAE** molecule. Fig. 5.9 shows the experimental two-dimensional ^{1}H-^{13}C HETCOR experiment that allowed us to partially assign ^{1}H and ^{13}C resonances for the SSRD. In addition, the methyl group ^{13}C signal at 27.7 ppm indicated the existence of residual monomer reactant. Because of

possible overlap with monomer in the region 122 ppm ~ 132 ppm, the aromatic carbons C2, C3, C10, and C9 in the SSRD, along with their corresponding protons, were not assigned; the remaining chemical shift assignments are reported in Table 5.2.

The agreement between calculated isotropic chemical shifts and experimental chemical shifts can be quantified by the reduced χ^2 statistics, $\chi^2 = \frac{1}{N}\sum_i \frac{\left(\delta_i^{calc} - \delta_i^{\exp}\right)^2}{RMSD_i^2}$. In the equation, δ_i^{calc} is the i^{th} calculated chemical shift, δ_i^{calc} is the corresponding experimental chemical shift, and $RMSD_i$ is the expected root-mean-standard deviation of

Table 5.2. Isotropic chemical shifts (ppm) for the SSRD[a]. Experimental values were measured using a HETCOR experiment. Computational values were calculated using *CASTEP* on the *Pccn* candidate.

Position	C^{exp}	C^{cal}	Position	H^{exp}	H^{cal}
C1		131.01	H1	7.31	6.86
C2		129.74	H2		7.44
C3		127.92	H3		7.04
C4		130.28	H4	7.27	7.03
C5	141.78	143.64	H5	5.93	5.91
C6	55.89	57.39	H6	7.27	7.03
C7	141.78	143.92	H7		7.06
C8		130.05	H8		7.41
C9		128.26	H9	7.31	6.83
C10		129.87	H10-18[c]	1.17	1.10[c]
C11		131.13			
C12	144.79	147.91			
C13	68.06	69.02			
C14	144.79	148.16			
C15	173.11	178.06			
C16	84.90	85.53			
C17-19[b]	29.19	29.60[b]			

[a] Chemical shifts were referenced to TMS by the CH_2 shift in adamantane at 38.48 ppm, and single proton shift observed at 1.87 ppm for adamantane.

[b] The average values of the three calculated methyl carbon chemical shifts were listed, since they were not resolved in the HETCOR spectrum.

the calculated versus experimental shift for the corresponding nuclei (proton, carbohydrate carbon, or aromatic carbon); values for $RMSD_i$ were taken from previous work that surveyed multiple compounds under analogous computational conditions.[68] A χ^2 value closer to 1.0 indicates a higher level of agreement between calculated and experimental chemical shifts. In the case of χ^2 analysis using isotropic chemical shifts, six candidates, of space groups *Pbca*, *Pccn*, *P2₁cn*, P2₁ca, Pcc2, and *P2₁2₁2₁*, all sit well within the 95% confidence interval (Fig. 5.12(a)). The other two candidates, *Aba2* and *A2₁22* did not agree with ^{13}C experimental chemical shifts. For these two structures, deviations mostly came from the extra chemical shifts calculated distributing over the 141 ppm to 149 ppm range,

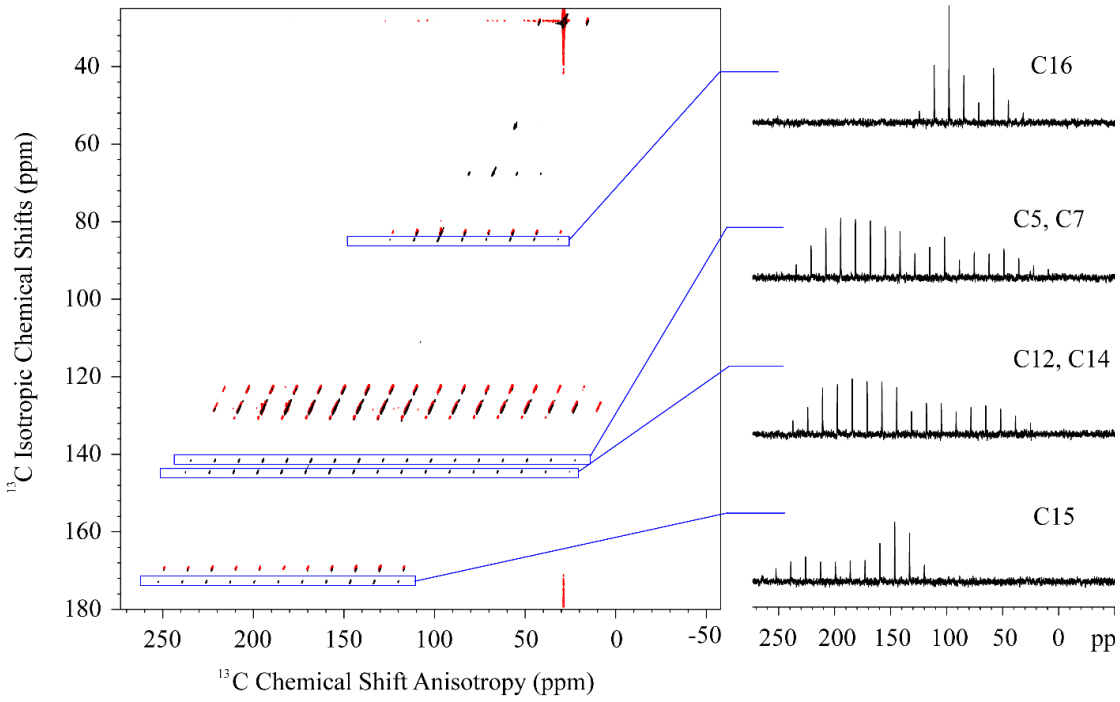

Figure 5.10. The TOSS-deTOSS experiment on SSRD (black). The sideband-free isotropic chemical shift is on y-axis, while chemical shift anisotropies are along x-axis. Four traces were taken for fitting using Mathematica, as marked in blue boxes. They are shown on the right. The monomer TOSS-deTOSS spectrum is overlaid on the 2D SSRD spectrum in red. Since there was residual monomer presented in the SSRD samples, overlapping areas were not taken into account for tensor fitting.

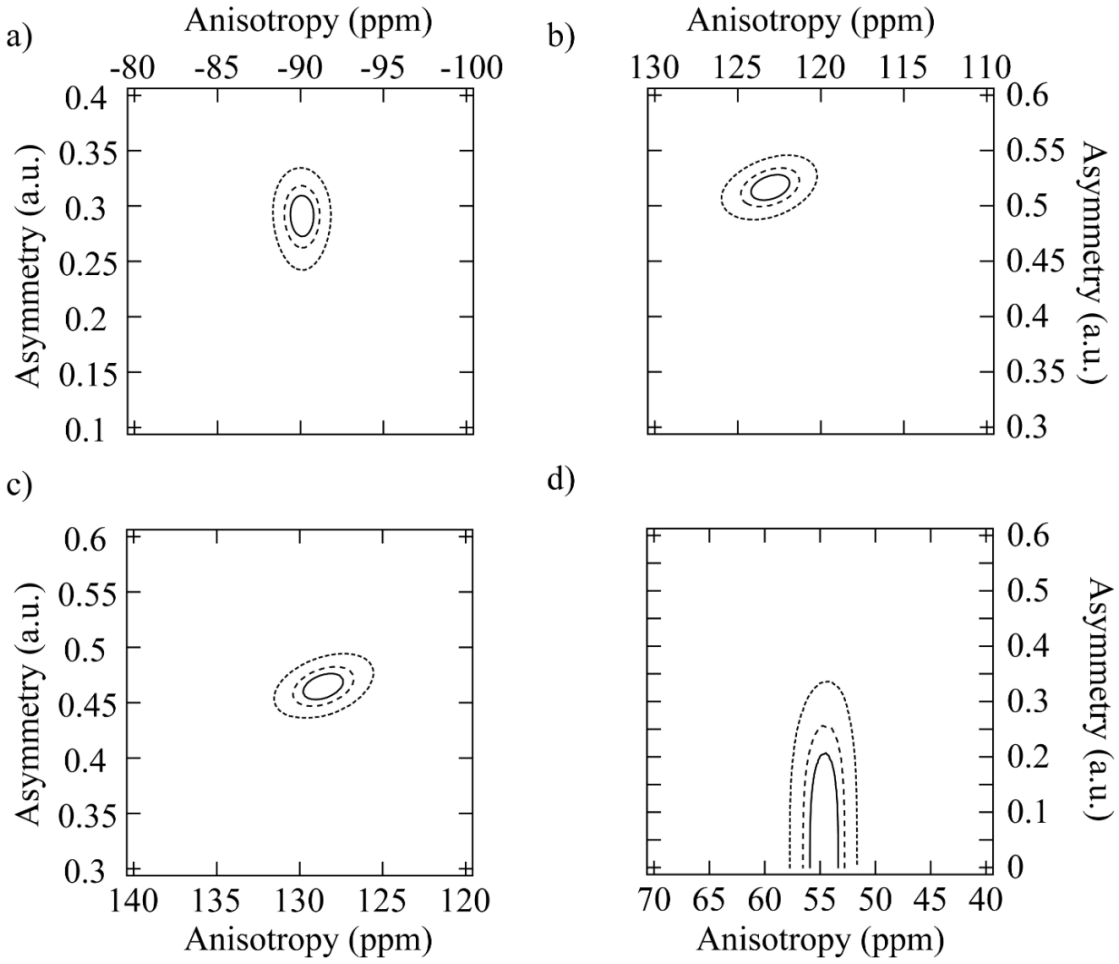

Figure 5.11. Anisotropy (Δ_{aniso}) and asymmetry (η) chemical shift tensor parameters fitted from sideband intensities extracted from Figure S8. χ^2 statistic corresponding to four distinctive traces from Fig. S3 are shown: a) C15, b) C12, C14, c) C5, C7, and d) C16. The values were determined using a mathematica notebook from Malcolm Levitt.[11] The solid contours represent the 68.3% confidence limits of the individual Δ_{aniso} and η components. The dashed contours bound the 68.3% joint confidence level, while the dotted contours represent the 95.4% joint confidence level. The tensor parameters correspond to tensor principle values following Haeberlen's convention, with $\delta_{iso} = (\delta xx + \delta yy + \delta zz)/3$, $\Delta = \delta zz - \delta iso$, and $\eta = (\delta xx - \delta yy)/(\delta zz - \delta iso)$. Three principle values for each δ_{iso}, Δ, and η pair were derived according to $\delta xx = -\frac{(1+\eta)\Delta}{2} + \delta_{iso}$, $\delta yy = -\frac{(1-\eta)\Delta}{2} + \delta_{iso}$, and $\delta zz = \Delta + \delta_{iso}$. Nine tensor values from a), b) and c) were used for further χ^2 analysis shown in Figure 5.12 b). Tensor values for C16 as shown in d) were not included, because of uncertainty in the asymmetry parameter and the rapid tumbling of the tert-butyl groups.

while only two chemical shifts were observed experimentally for these rigid carbons (C5, C7, C12, and C14). The six best structures were then screened against experimental ^{13}C chemical shift anisotropy tensor components.

^{13}C tensor values were measured using the TOSS-t_1-deTOSS pulse sequence (Fig. 5.2). Experimental results are shown in Fig. 5.10. Tensor values were determined by a fit of the sideband intensities using Herzfeld-Berger analysis[70] as shown in Fig. 5.11, implemented within a Mathematica notebook from Antzutkin et al.[71] Three traces of sidebands were selected (corresponding to tensor information from C5, C7, C12, C14 and C15). Other peaks were either contaminated by residual monomer signal or did not provide enough sidebands for a precise fit. The anisotropy (Δ) and asymmetry (η) parameters (defined using Haeberlen's convention; anisotropy parameter $\Delta = \delta_{zz} - \delta_{iso}$ and asymmetry parameter $\eta = (\delta_{xx} - \delta_{yy})/(\delta_{zz} - \delta_{iso})$.)[72] were converted to tensor components (δ_{xx}, δ_{yy}, and δ_{zz}). A χ^2 analysis of computed tensor components against experimental values (9 experimental tensor components in total) indicated that four candidates (of space groups *Pbca*, *Pccn*, $P2_1cn$, and $P2_12_12_1$) remained within the 95% confidence interval (Fig. 5.12(b)). These structures represent an ensemble of the closest description of the SSRD crystal structure (Fig. 5.17). When overlaid against the *Pccn* candidate, an RMSD range of 0.025 Å ~ 0.069 Å can be achieved for the *Pbca*, $P2_1cn$, and $P2_12_12_1$ candidates, with methyl groups left out of the structural overlays. Since these four structures are identical to within the experimental uncertainty, the mechanism for expansion was analyzed using the *Pccn* space group that produced the lowest R_{wp} value. We stress that after structural refinement in Powder Solve, followed by Rietveld refinement, and DFT geometry optimization, the alternative

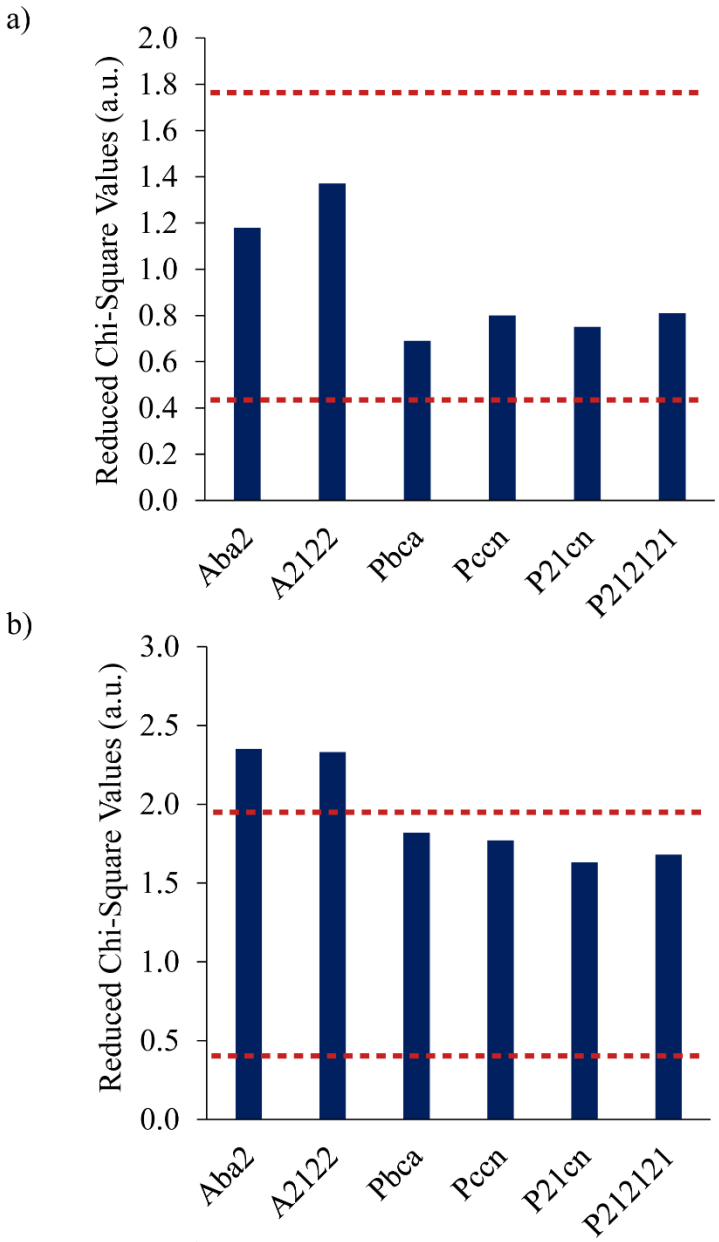

Figure 5.12. χ^2 analysis of calculated chemical shifts a) and chemical shielding tensors b) against experimental values. A χ^2 closer to 1.0 represents a better agreement with experiments. 95% confidence range is displayed as red lines. In a). Six candidates fell within the range. The calculated chemical shifts of space group *P2₁ca* and *Pcc2* are not assignable due to disagreement with experimental values, so they are discarded. In b), 9 tensor values were calculated from Fig. S10, and when 9 degrees of freedom were selected, the 95% confidence level resulted in χ^2 ranging from 0.369 to 1.880, as shown as red dashed lines in b). Pccn candidate was demonstrated in the major content for expansion because of its lowest R_{wp} value.

structures ended up being almost identical to the structure discussed below (Fig 5.17), and would lead to the same conclusions about the structural changes and the origin of the nanorod expansion.

The SSRD crystal parameters are compared to those of monomeric 9TBAE in Table 5.3, and the three relevant crystal structures (monomer, SSRD dimer, and the lower energy

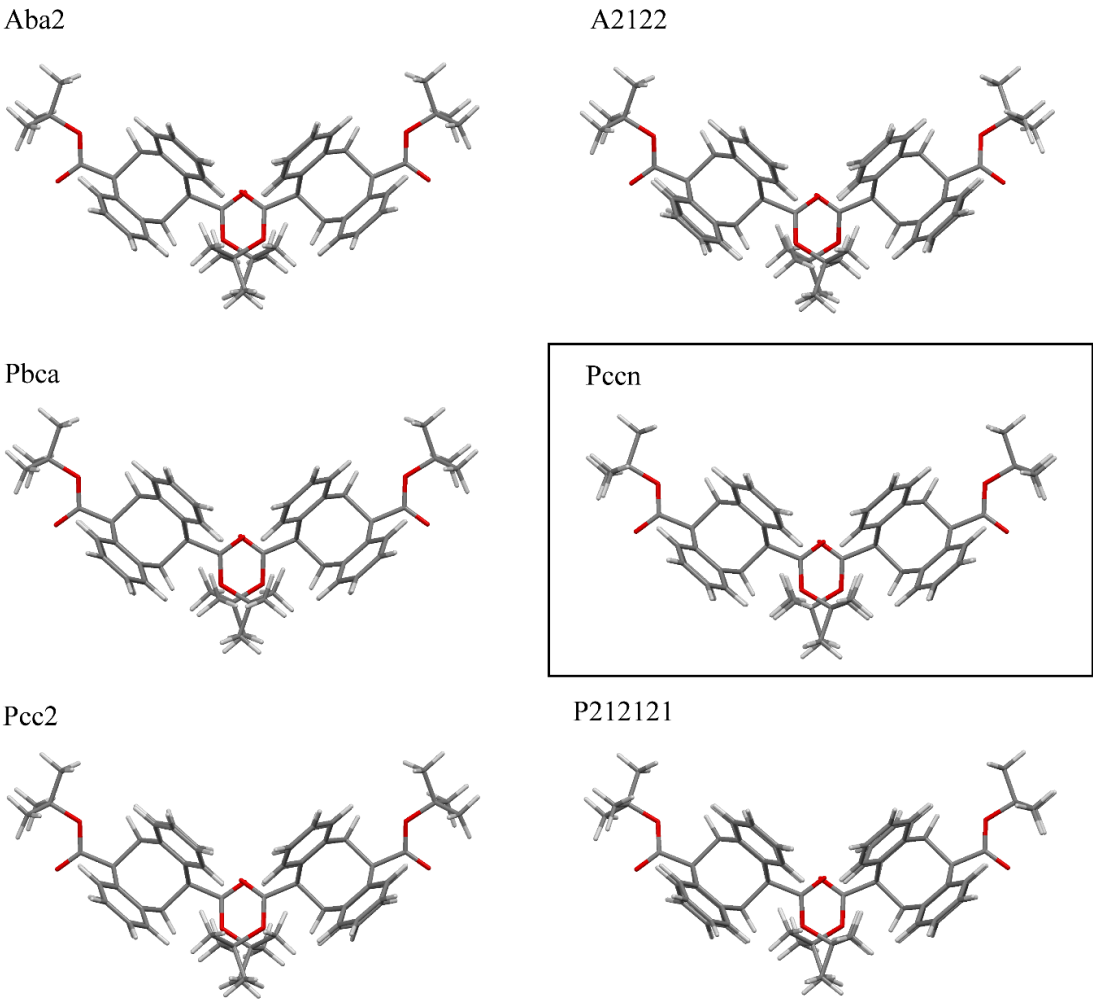

Figure 5.13. Six of the eight candidate structures, which agreed with the assignments by HETCOR experiments as shown in the paper contents. The *P2₁ca* and *Pcc2* candidates produce multiple chemical shifts not observed in our, and are filtered out by NMR. The *Pccn* space group produced both the smallest R_{wp}'s before and after *CASTEP* refinements, the bottom four structures are of RMSD < 0.1 Å when overlaid (excluding the rotating methyl carbons along with their attached protons).

Table 5.3. Crystal data for monomer and SSRD

	$C_{19}H_{18}O_2$ (monomer)	$C_{38}H_{36}O_4$ (SSRD)
Formula weight	278.33	556.67
Crystal System	Monoclinic	Orthorhombic
Space group	*P2(1)/n* (#14)	*Pccn* (#56)
Unit cell dimensions	a = 9.1313(7), α = 90.00 b = 17.5205(14), β = 99.9029(14) c = 9.7613(8), γ = 90.00	a = 15.8708, α = 90.00 b = 12.0647, β = 90.00 c = 15.7589, γ = 90.00
Volume	1538.39	3017.48
Z	4	4
Density (calculated)	1.202 Mg m^{-1}	1.225 Mg m^{-1}

SGD dimer) are shown in Fig. 5.14. The SSRD structure has an orthorhombic cell with unit cell dimensions a = 15.8708 Å, b = 12.0647 Å, and c = 15.7589 Å, and volume = 3017.46 $Å^3$. It is interesting to note that the volume per anthracene unit of the SSRD unit cell is actually slightly less than that of the monomer, leading to a slightly higher density.

5.3.3. PXRD Determination of Crystal Orientations within the Nanorods

Armed with knowledge of the SSRD crystal structure, we are now in a position to quantitatively analyze how photoreaction of the monomer **9TBAE** molecules within the nanorods leads to the observed expansion. The last step is to analyze the orientations of the crystals with respect to the nanorod axis. This was accomplished by performing PXRD experiments on **9TBAE** nanorods aligned within an AAO template lying horizontally on the diffractometer. These aligned crystals do not give a true powder pattern: the diffraction intensity is dominated by lines corresponding to Miller planes parallel to the template, or perpendicular to the rod axis. From this set of the PXRD data, and from the comparison with calculated PXRD of predicted SSRD crystal structures, the peak at 10.8° was assigned to SSRD (111) plane; and the peak at 27.4° was assigned to the (232) plane. In the monomer,

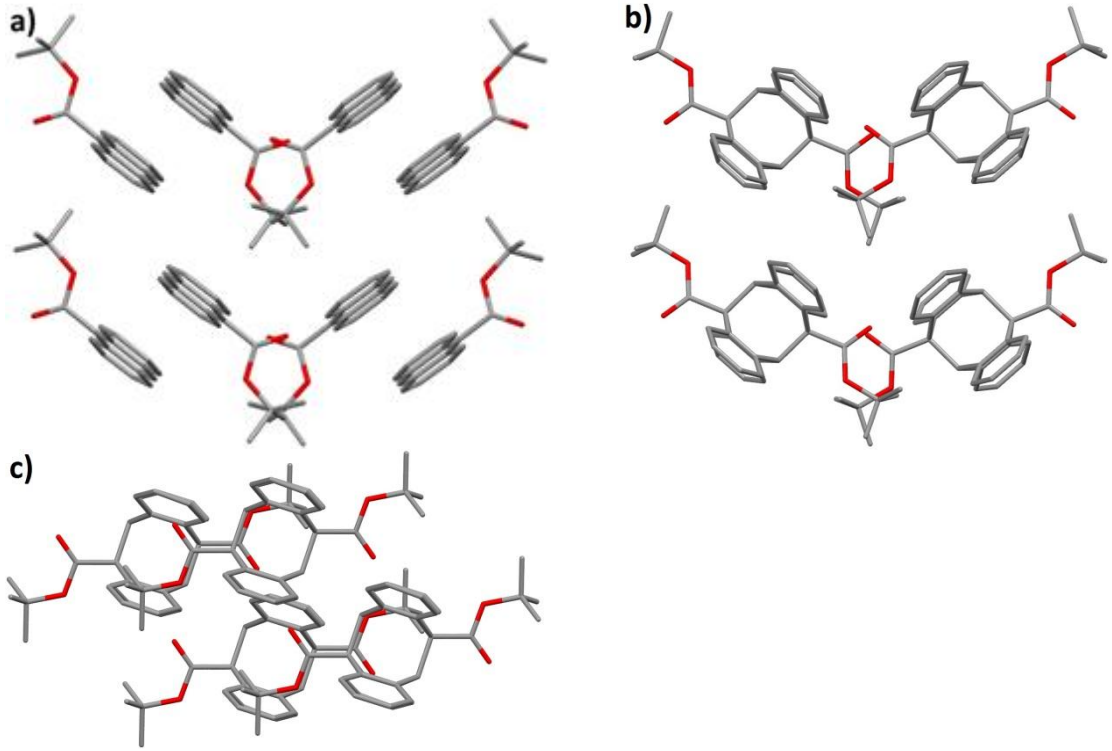

Figure 5.14. Molecular packing in a) the **9TBAE** monomer crystal; b) the metastable SSRD dimer crystal; and c) the stable SGD dimer crystal.

correspondingly, the peak at 10.5° was assigned the (011) plane. And the dimerization initiated by illumination causes the monomer (011) plane peak intensities to decrease, while the SSRD (111) and (232) peaks emerge and increase, indicating the conversion of monomer (011) plane into SSRD (111) and (232) plane, perpendicular to the nanorod growth direction. When the original (011) plane of monomer was transformed into the (111) plane of the SSRD after photoreaction, a 2% decrease of the molecules' projection onto the rod axis is calculated. However, if the crystal rotates so that the SSRD (232) plane is perpendicular to the rod axis, the molecular projection onto the rod axis increases by 16.2%, from 8.430 Å to 9.794 Å (see Fig. 5.15). The transformation that leads to the (232) dimer

plane being perpendicular to the rod axis can be viewed as a molecular rotation of 11.45°, as shown in Fig. 5.15

The appearance of the (232) peak at 27.4° provides an explanation for the large expansion of the 9TBAE nanorods, but before this conclusion can be taken as fact, several issues concerning the PXRD data need to be resolved. First, we need to consider the possible role of the monomer (110) orientation that is present as a minor component. Like

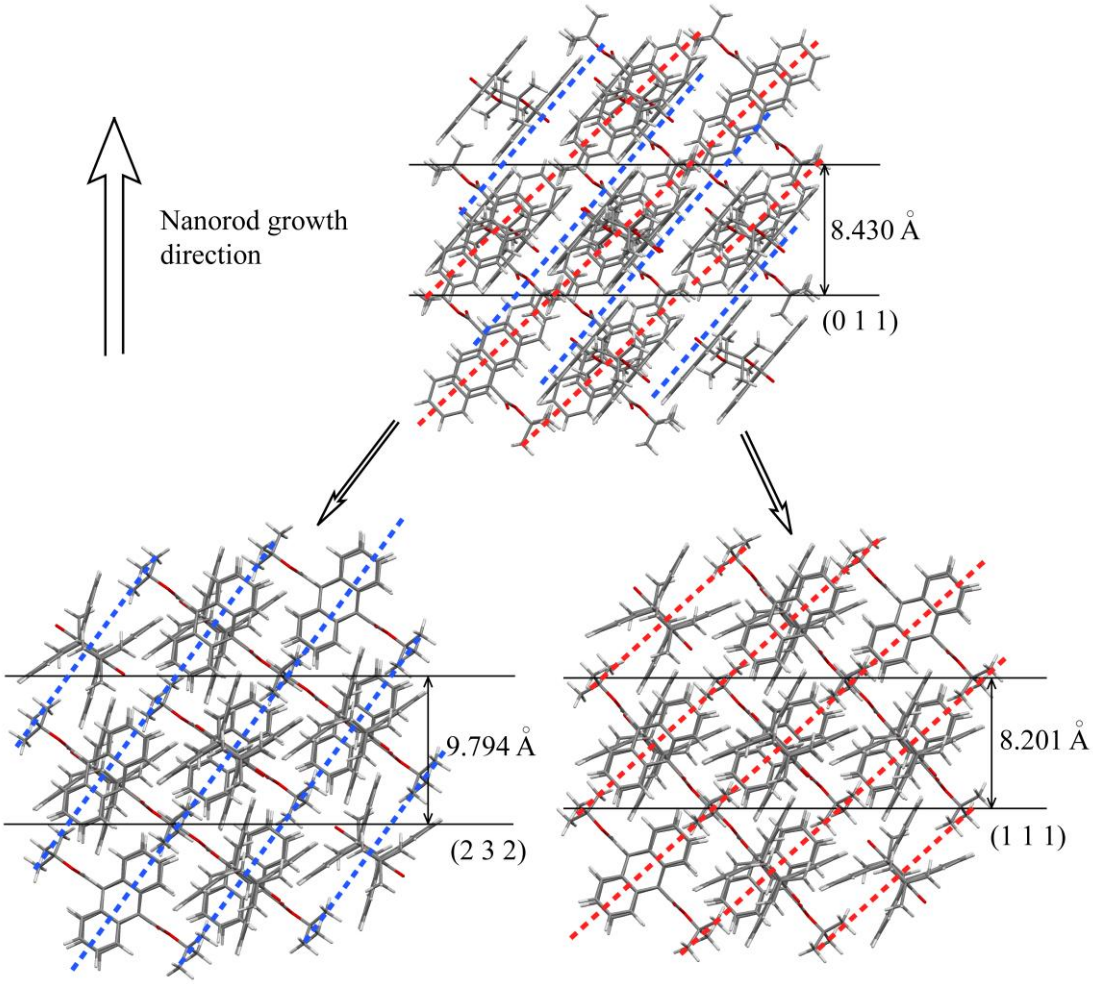

Figure 5.15. Photodimerization of 9TBAE. The monomer is shown at the top, and the two different orientations of the dimer crystal are shown at the bottom. If the dimer nanorod axis is perpendicular to the (232) plane, there will be a 16% expansion relative to the monomer, while if the dimer (111) plane ends up perpendicular to the nanorod axis, there will be a 2% contraction.

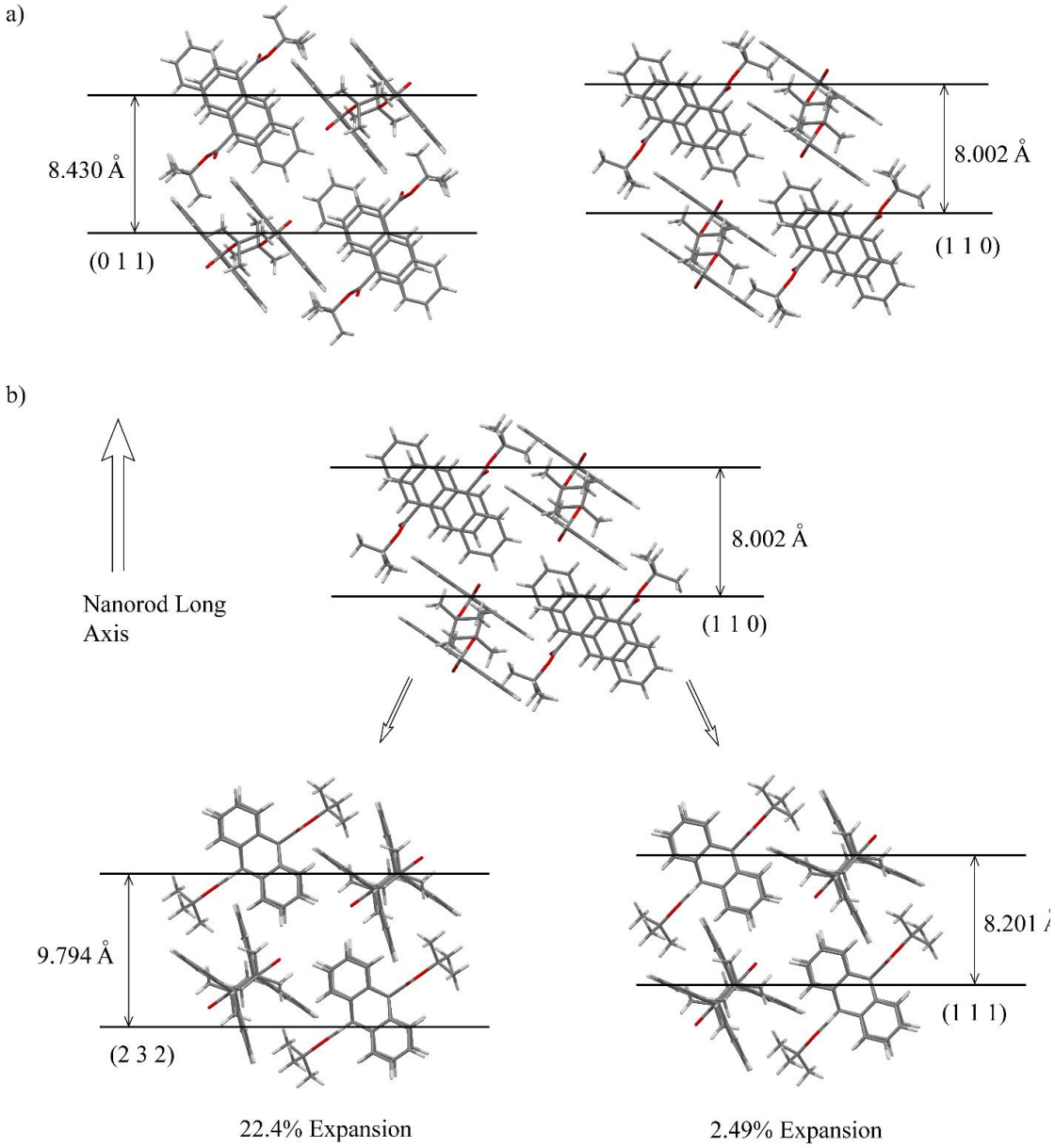

Figure 5.16. a) Crystal orientations corresponding to the (011) and (110) Miller planes of the monomer **9TBAE** crystal perpendicular to the nanorod axis. b) Expansions of the SSRD crystal starting from the minority population with (110) plane oriented perpendicular to the rod axis. There is a 2.5% expansion if the dimer nanorods end up with their (111) plane oriented perpendicular to the rod axis, and a 22.4% expansion if the dimer nanorods end up with their (232) plane oriented perpendicular to the rod axis.

the (011) orientation, this orientation has the anthracene rings tilted with respect to the rod axis, but at a slightly different angle (Fig. 5.16). The transition from the monomer (110) orientation to the dimer (111) and (232) orientations leads to calculated length changes of +2.5% and +22.4%, respectively. These changes are comparable to what is calculated for the (011) starting orientation. Thus the presence of a small (110) monomer orientation does not change the conclusion that the nanorod expansion is driven by two competing final orientations. A second issue is the assignment of the peak at 27.4° to the (232) Miller plane. The width of the peak makes its center position somewhat uncertain. Analysis of multiple data sets fixed the center of the peak at 27.4+/-0.1°, and we consider the possible influence of nearby peaks corresponding to the (124) plane at 27.6° and the (421) plane at 27.5°. It turns out that transformation of the (110) monomer orientation into the (124) or (421) orientations produces similar expansions of about 15%. However, these two orientations do not correspond to a simple tilt, unlike the (232) orientation shown in Fig. 5.15. To reach these orientations, the dimer molecules would have to rotate by a large amount in two different directions. From a principle of least motion, the (232) orientation seems most reasonable. Finally, we need to consider why the peak at 27.4° is so broad compared to the peak at 10.5°. If we assume that the broadening is due to the formation of small domains, the Scherrer equation leads to an estimation of 10 nm for the average domain size. An alternate explanation for the peak broadening is that the large tilt of the (232) orientation induces local strain that produces slight changes in lattice spacing within these domains.[73] This is consistent with the idea that the (232) orientation requires greater motion and induces more local strain than the (111) orientation, whose diffraction peak remains narrow.

The fact that the expanding rods remain intact after photoreaction also suggests that the peak broadening is likely due to strain-induced broadening rather than to fragmentation into nanodomains.

5.4 Discussion

The first important result of this chapter is the successful determination of the SSRD crystal structure using a combined PXRD/computation/SSNMR approach. To our knowledge, this is the first time that NMR crystallography has been applied to solve a product structure in solid-state organic photochemistry. Both the PXRD and NMR data

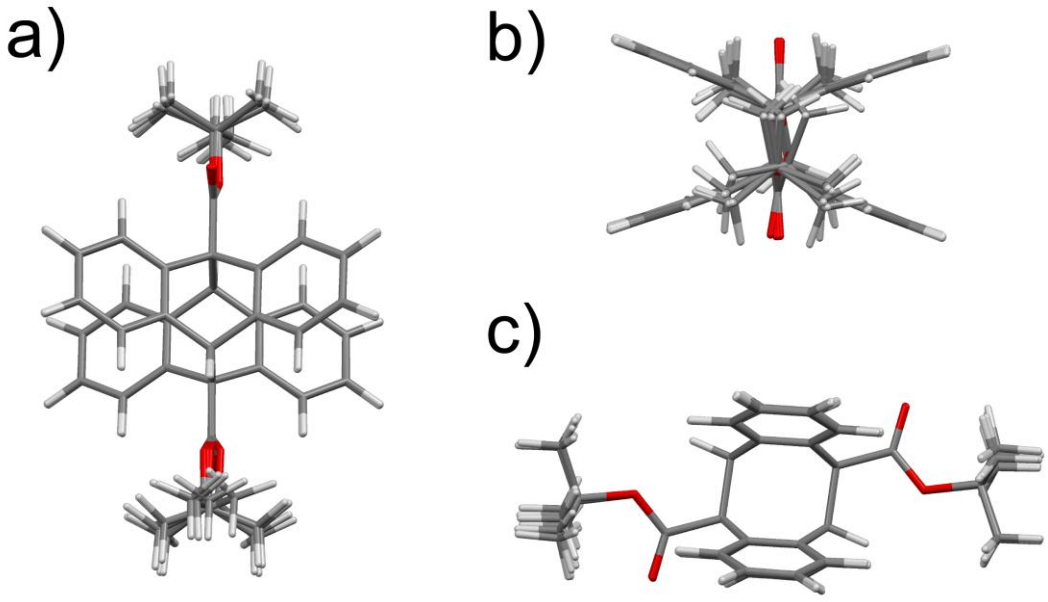

Figure 5.17. Overlaid candidates of space groups *Pccn*, $P2_12_12_1$, $P2_1cn$, and *Pbca*. a), b) and c) provide three views of the overlaid candidate structures. The RMSD's calculated against the *Pccn* space group are 0.0422 for $P2_12_12_1$, 0.0685 for $P2_1cn$, and 0.0254 for *Pbca*. The methyl carbons and their associated protons were not included in the RMSD calculations, since they underwent frequent rotation at room temperature. The structures have small differences (quantified as <0.1 RMSD values).

were necessary to converge on a structure consistent with all the experimental observables. PXRD is important for estimating long range order. In the case of the SSRD, it predicted structures with characteristic herringbone stacking arrangements and detailed cell dimensions. However, the limited number of peaks and broad linewidths of the organic microcrystals prevented an accurate prediction of local arrangements. DFT calculations helped refine the structures predicted by PXRD analysis and calculate spectroscopic observables that could be compared with NMR experiments. The SSNMR experiments served as a final validation step, allowing us to rule out several structure candidates and converge on a single structural motif for the SSRD.

The SSRD structure shown in Figures 5.13 and 5.17 is consistent with previous work.[28] Several structural aspects deserve special mention. First, the overall herringbone pair packing of the anthracene units is maintained in the SSRD, despite the fact that the anthracenes are now connected via the new bonds formed by the [4+4] dimerization. This metastable packing can be contrasted with that of the lower energy SGD structure in Fig. 5.14, where the anthracenes are arranged in parallel layers. Second, the tert-butyl ester groups of the SSRD are rotated inward, similar to their orientation in the monomer crystal. In the SGD crystal, these sidegroups rotate by ~180° to face outward, in order to associate with each other in the layered packing structure.

Unfortunately, the crystal structure parameters in Table 5.3 provide no obvious reason for the nanorod expansion. From Table 5.3, the overall volume per anthracene unit actually decreases for the SSRD, and the structure shows no evidence for large molecular rearrangements. However, the presence of two different crystal orientations in the nanorod

PXRD data indicates that some type of crystal reorientation occurs during the photochemical reaction. The monomer crystal is a herringbone pair (also known as a sandwich herringbone) lattice composed of two distinct sublattices of paired monomers, denoted **A** and **B** as shown schematically in Fig. 5.18. Molecular pairs from these two sublattices have different orientations. If we let the long axis of the anthracene define a vector (from midpoint of the first aromatic ring to the midpoint of the third aromatic ring), there is a fixed angle between the vectors of neighboring herringbone pair molecules. This angular mismatch is shown in top part of Fig. 5.18 for the monomer crystal. When the

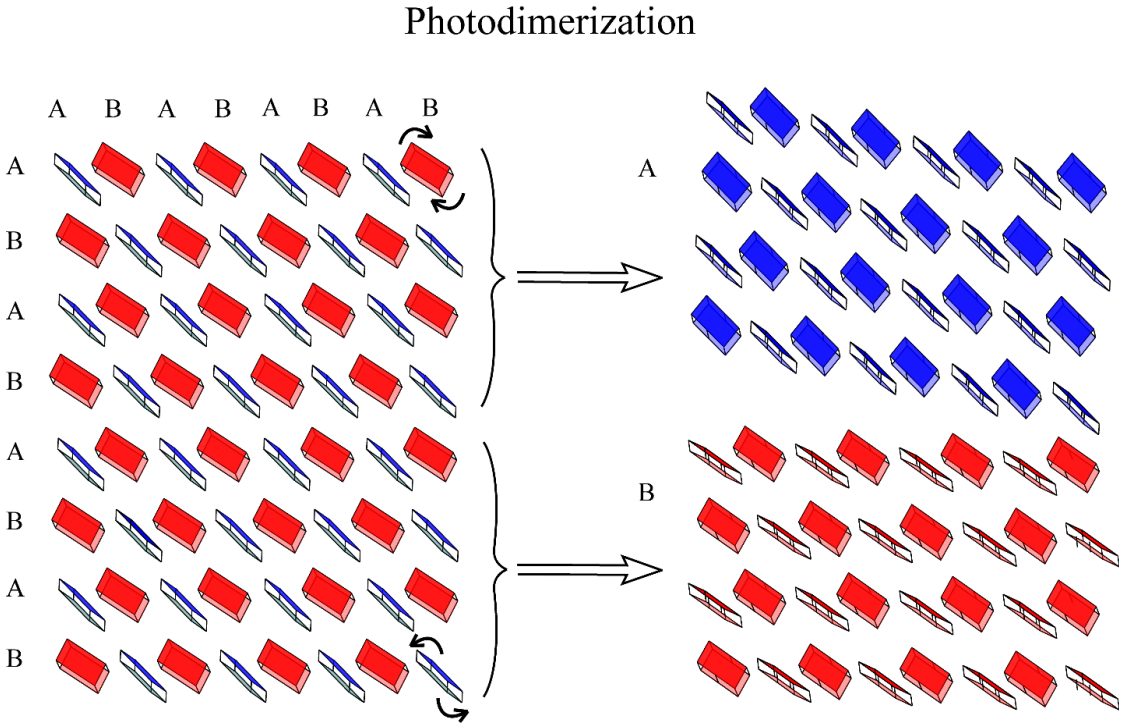

Figure 5.18. Schematic illustration of the symmetry breaking mechanism induced by **9TBAE** photodimerization. Each box represents a **9TBAE** monomer (sandwich) pair. Monomer pairs corresponding to the different sublattices are colored blue (sublattice **A**) and red (sublattice **B**). If the dimers in sublattice **A** rotate while the **B** dimers remain stationary, the dimer crystal will orient along the normal of (111) plane, leading to a 2% contraction as indicated in the bottom right illustration. If the dimers in sublattice **B** rotate while the **A** dimers remain stationary, the dimer crystal will orient along the normal of (232) plane, leading to a 16% expansion as shown in the top right.

SSRD is formed, the herringbone pair motif is retained, but the angular relation between the pairs changes. The vectors pointing along the long axes of neighboring dimerized pairs are now parallel, as shown in the lower panels of Fig. 5.17.

How can the dimers achieve the new pair-pair orientation? In the simplest case, the crystal has two choices: the pairs in sublattice **A** can rotate while sublattice **B** remains stationary, or sublattice **B** can rotate with respect to **A**. The **A** and **B** sublattices are equivalent (except for their orientation with respect to the rod axis) and thus the rotation necessitates a choice between symmetric options, i.e. it can be thought of as a symmetry breaking event. The two choices are shown in cartoon form in Fig. 5.18. Rotation of sublattice **A** means that the (111) plane of the SSRD crystal will be perpendicular to the rod axis and will be the dominant peak in the PXRD pattern. But this rotation leads to a 2% decrease in the crystal projection along the rod axis. If all the molecules behaved in this manner, we would expect to see a 2% shrinkage of the rod. If, on the other hand, sublattice **A** rotates to follow sublattice **B**, we find that the (232) Miller plane ends up perpendicular to the rod axis and the crystal projection along the rod increases by 16%. Thus the overall length change depends on which sublattice "wins" and forces the other to rotate to accommodate the new photodimer crystal packing. The induced tilt mechanism for crystal elongation resembles that recently proposed for a mechanically induced phase transition in an organic cocrystal that led to an elongation by a factor of 2.[74] The origin of that expansion was also a change in the tilt angles of the molecular π systems. Note that the tilting of sublattice **A** to accommodate sublattice **B** involves more molecular movement and this can lead to greater disorder and broadening of the (232) diffraction peak.

We define the bifurcation into **A→B** or **B→A** sublattice rotations as "symmetry breaking" in analogy with photoinduced chemical reactions where the system must choose between two equivalent outcomes.[75–77] We can deduce something about how frequently these symmetry breaking events occur within a single rod by considering two limiting cases. If the symmetry breaking was purely stochastic and occurred many times within a single rod, we would expect a 50:50 mixture of **A** and **B** rotations. This would lead to a uniform expansion of 7% for every nanorod, due to averaging over equal numbers of **A** and **B** rotations. In the other limit, if the symmetry breaking only occurs once per nanorod, we would expect to see a bimodal distribution in which each rod either expands by 16% or contracts by 2%. Experimentally, we see a distribution of expansions (never contractions), but the ensemble average is close to the 7% value expected for a random mixture of A and B rotations.[28] The fact that some rods favor **B** rotation to **A** (small expansion) while others favor **A** rotation to **B** (large expansion) may be a result of local environmental factors, or even slight differences in illumination conditions.

Given this mechanism, general observations about the design of molecular crystal materials that give rise to large photomechanical response becomes possible. The ability to induce molecular rotation or tilt relative to the crystal axis is an effective strategy for inducing large expansions, since it does not require large molecular translations. In **9TBAE**, this tilt arises from symmetry breaking during the photodimerization that favors one sublattice of the herringbone pair crystal. It is an open challenge for the crystal engineering community to design other classes of molecular crystals that can undergo such tilting transformations in response to an external perturbation. A separate challenge would be to

orient the crystal within a larger structure in a way such that the photoinduced tilt leads to the desired motion along a chosen coordinate. For example, one could envision cutting a **9TBAE** crystal so that a different Miller plane is perpendicular to the rod axis, perhaps leading to contraction rather than expansion.

5.5 Conclusion

This work demonstrates the successful application of NMR crystallography to determine the crystal structure of a metastable crystal intermediate. This achievement in turn allowed us to determine the physical origin of the large (up to 15%) photomechanical expansion seen in anthracene ester nanorods. We found that an induced tilt of the photoproduct drives the expansion, rather than changes in the volume or unit cell parameters of the product crystal. This tilt originates from a symmetry breaking during the reaction that causes one crystal sublattice to reorient relative to the other. The results in this paper provide a starting point for the design of photoactive molecular crystals whose mechanical response arises from a reconfiguration of the molecular packing, as opposed to the creation of a mixed bimorph structure.

5.6 References

(1) Kim, T.; Zhu, L.; Al-Kaysi, R. O.; Bardeen, C. J. Organic photomechanical materials. *ChemPhysChem*, 2014, *15*, 400–414.

(2) Barrett, C. J.; Mamiya, J.; Yager, K. G.; Ikeda, T. Photo-mechanical effects in azobenzene-containing soft materials. *Soft Matter*, 2007, *3*, 1249.

(3) Finkelmann, H.; Nishikawa, E.; Pereira, G. G.; Warner, M. *Phys. Rev. Lett.* **2001**, *87*, 015501.

(4) Garcia-Garibay, M. A. Molecular crystals on the move: From single-crystal-to-single-crystal photoreactions to molecular machinery. *Angewandte Chemie - International Edition*, 2007, *46*, 8945–8947.

(5) Nath, N. K.; Panda, M. K.; Sahoo, S. C.; Naumov, P. *CrystEngComm* **2014**, *16*, 1850.

(6) Lange, C. W.; Foldeaki, M.; Nevodchikov, V. I.; Cherkasov, V. K.; Abakumov, G. A.; Pierpont, C. G. *J. Am. Chem. Soc.* **1992**, *114*, 4220.

(7) Al-Kaysi, R. O.; Bardeen, C. J. *Adv. Mater.* **2007**, *19*, 1276.

(8) Kobatake, S.; Takami, S.; Muto, H.; Ishikawa, T.; Irie, M. *Nature* **2007**, *446*, 778.

(9) Morimoto, M.; Irie, M. *J. Am. Chem. Soc.* **2010**, *132*, 14172.

(10) Terao, F.; Morimoto, M.; Irie, M. *Angew. Chem. Int. Ed. Engl.* **2012**, *124*, 925.

(11) Naumov, P.; Kowalik, J.; Solntsev, K. M.; Baldridge, A.; Moon, J. S.; Kranz, C.; Tolbert, L. M. *J. Am. Chem. Soc.* **2010**, *132*, 5845.

(12) Koshima, H.; Takechi, K.; Uchimoto, H.; Shiro, M.; Hashizume, D. Photomechanical bending of salicylideneaniline crystals. *Chemical Communications*, 2011, *47*, 11423.

(13) Koshima, H.; Nakaya, H.; Uchimoto, H.; Ojima, N. Photomechanical Motion of Furylfulgide Crystals. *Chemistry Letters*, 2012, *41*, 107–109.

(14) Bushuyev, O. S.; Tomberg, A.; Friščić, T.; Barrett, C. J. *J. Am. Chem. Soc.* **2013**, *135*, 12556.

(15) Kim, T.; Al-Muhanna, M. K.; Al-Suwaidan, S. D.; Al-Kaysi, R. O.; Bardeen, C. J. *Angew. Chem. Int. Ed.* **2013**, *125*, 7027.

(16) Zhu, L.; Al-Kaysi, R. O.; Bardeen, C. J. *J. Am. Chem. Soc.* **2011**, *133*, 12569.

(17) Kitagawa, D.; Nishi, H.; Kobatake, S. *Angew. Chemie - Int. Ed.* **2013**, *52*, 9320.

(18) Naumov, P.; Sahoo, S. C.; Zakharov, B. Z.; Boldyreva, E. V. *Angew. Chemie - Int. Ed.* **2013**, *125*, 10174.

(19) Warner, M.; Mahadevan, L. *Phys. Rev. Lett.* **2004**, *92*, 134302.

(20) Kuroki, L.; Takami, S.; Yoza, K.; Morimoto, M.; Irie, M. *Photochem. Photobiol. Sci.* **2010**, *9*, 221.

(21) Nath, N. K.; Pejov, L.; Nichols, S. M.; Hu, C.; Saleh, N.; Kahr, B.; Naumov, P. *J. Am. Chem. Soc.* **2014**, *136*, 2757.

(22) Kim, T.; Zhu, L.; Mueller, L. J.; Bardeen, C. J. *J. Am. Chem. Soc.* **2014**, *136*, 6617.

(23) Jena, A. K.; Chaturvedi, M. C. *Pnase Transformation in Materials*; Prentice-Hall: New Jersey, 1992.

(24) Keating, A. E.; Garcia-Garibay, M. A. In *Organic and Inorganic Photochemistry*; Ramamurthy, V.; Schanze, K. S., Eds.; Dekker: New York, 1998; Vol. 2, pp. 195–248.

(25) Takahashi, S.; Miura, H.; Kasai, H.; Okada, S.; Oikawa, H.; Nakanishi, H. *J. Am. Chem. Soc.* **2002**, *124*, 10944.

(26) Al-Kaysi, R. O.; Müller, A. M.; Bardeen, C. J. *J. Am. Chem. Soc.* **2006**, *128*, 15938.

(27) Bučar, D. K.; MacGillivray, L. R. *J. Am. Chem. Soc.* **2007**, *129*, 32.

(28) Zhu, L.; Agarwal, A.; Lai, J.; Al-Kaysi, R. O.; Tham, F. S.; Ghaddar, T.; Mueller, L.; Bardeen, C. J. *J. Mater. Chem.* **2011**, *21*, 6258.

(29) Facelli, J. C.; Grant, D. M. *Nature* **1993**, *365*, 325.

(30) Lai, J.; Niks, D.; Wang, Y.; Domratcheva, T.; Barends, T. R. M.; Schwarz, F.; Olsen, R. a; Elliott, D. W.; Fatmi, M. Q.; Chang, C. a; Schlichting, I.; Dunn, M. F.; Mueller, L. J. *J. Am. Chem. Soc.* **2011**, *133*, 4.

(31) Olsen, R. a; Struppe, J.; Elliott, D. W.; Thomas, R. J.; Mueller, L. J. *J. Am. Chem. Soc.* **2003**, *125*, 11784.

(32) Brouwer, D. H.; Darton, R. J.; Morris, R. E.; Levitt, M. H. *J. Am. Chem. Soc.* **2005**, *127*, 10365.

(33) Harper, J. K.; Grant, D. M.; Zhang, Y.; Lee, P. L.; Von Dreele, R. *J. Am. Chem. Soc.* **2006**, *128*, 1547.

(34) Harris, R. K.; Joyce, S. a; Pickard, C. J.; Cadars, S.; Emsley, L. *Phys. Chem. Chem. Phys.* **2006**, *8*, 137.

(35) Rajeswaran, M.; Blanton, T. N.; Zumbulyadis, N.; Giesen, D. J.; Conesa-Moratilla, C.; Misture, S. T.; Stephens, P. W.; Huq, A. *J. Am. Chem. Soc.* **2002**, *124*, 14450.

(36) Salager, E.; Day, G. M.; Stein, R. S.; Pickard, C. J.; Elena, B.; Emsley, L. *J. Am. Chem. Soc.* **2010**, *132*, 2564.

(37) Webber, A. L.; Emsley, L.; Claramunt, R. M.; Brown, S. P. *J. Phys. Chem. A* **2010**, *114*, 10435.

(38) Luchinat, C.; Parigi, G.; Ravera, E.; Rinaldelli, M. *J. Am. Chem. Soc.* **2012**, *134*, 5006.

(39) Baias, M.; Dumez, J.-N.; Svensson, P. H.; Schantz, S.; Day, G. M.; Emsley, L. *J. Am. Chem. Soc.* **2013**, *135*, 17501.

(40) Detken, A.; Hardy, E. H.; Ernst, M.; Meier, B. H. *Chem. Phys. Lett.* **2002**, *356*, 298.

(41) Kolbert, A. C.; Griffin, R. G. Two-dimensional resolution of isotropic and anisotropic chemical shifts in magic angle spinning NMR. *Chemical Physics Letters*, 1990, *166*, 87–91.

(42) Liu, S.-F.; Mao, J.-D.; Schmidt-Rohr, K. *J. Magn. Reson.* **2002**, *155*, 15.

(43) Dixon, W. .; Schaefer, J.; Sefcik, M. .; Stejskal, E. .; McKay, R. . Total suppression of sidebands in CPMAS C-13 NMR. *Journal of Magnetic Resonance (1969)*, 1982, *49*, 341–345.

(44) Antzutkin, O. N.; Shekar, S. C.; Levitt, M. H. Two-Dimensional Sideband Separation in Magic-Angle-Spinning NMR. *Journal of Magnetic Resonance, Series A*, 1995, *115*, 7–19.

(45) Ivchenko, N.; Hughes, C. E.; Levitt, M. H. *J. Magn. Reson.* **2003**, *164*, 286.

(46) Subramanian, S.; Bax, A. Generation of pure phase NMR subspectra for measurement of homonuclear coupling constants. *Journal of Magnetic Resonance (1969)*, 1987, *71*, 325–330.

(47) Morcombe, C. R.; Zilm, K. W. *J. Magn. Reson.* **2003**, *162*, 479.

(48) Accelrys Materials Studio, release 7.0, 2013.

(49) Harper, J. K.; Doebbler, J. a; Jacques, E.; Grant, D. M.; Von Dreele, R. B. *J. Am. Chem. Soc.* **2010**, *132*, 2928.

(50) Martineau, C. NMR crystallography: Applications to inorganic materials. *Solid State Nuclear Magnetic Resonance*, 2014, *63-64C*, 1–12.

(51) Day, G. M.; S Motherwell, W. D.; Jones, W. *Phys. Chem. Chem. Phys.* **2007**, *9*, 1693.

(52) Neumann, M. a. *J. Appl. Crystallogr.* **2003**, *36*, 356.

(53) Pawley, G. S. Unit-cell refinement from powder diffraction scans. *Journal of Applied Crystallography*, 1981, *14*, 357–361.

(54) Engel, G. E.; Wilke, S.; König, O.; Harris, K. D. M.; Leusen, F. J. J. *J. Appl. Crystallogr.* **1999**, *32*, 1169.

(55) Stephenson, G. A. *J. Pharm. Sci.* **2000**, *89*, 958.

(56) Rietveld, H. M. A profile refinement method for nuclear and magnetic structures. *Journal of Applied Crystallography*, 1969, *2*, 65–71.

(57) Toby, B. H. *Powder Diffr.* **2012**, *21*, 67.

(58) Clark, S. J.; Segall, M. D.; Pickard, C. J.; Hasnip, P. J.; Probert, M. I. J.; Refson, K.; Payne, M. C. *Zeitschrift fur Krist.* **2005**, *220*, 567.

(59) Pickard, C.; Mauri, F. *Phys. Rev. B* **2001**, *63*, 245101.

(60) Yates, J.; Pickard, C.; Mauri, F. *Phys. Rev. B* **2007**, *76*, 024401.

(61) Kalakewich, K.; Iuliucci, R.; Harper, J. K. *Cryst. Growth Des.* **2013**, *13*, 5391.

(62) Payne, M. C.; Teter, M. P.; Allan, D. C.; Arias, T. A.; Joannopoulos, J. D. *Rev. Mod. Phys.* **1992**, *64*, 1045.

(63) Hohenberg, P. *Phys. Rev.* **1964**, *136*, B864.

(64) Kohn, W.; Sham, L. J. *Phys. Rev.* **1965**, *140*, A1133.

(65) Perdew, J. P.; Burke, K.; Ernzerhof, M. Generalized Gradient Approximation Made Simple. *Physical Review Letters*, 1996, *77*, 3865–3868.

(66) Vanderbilt, D. *Phys. Rev. B* **1990**, *41*, 7892.

(67) Pfrommer, B. G.; Cote, M.; Louie, S. G.; Cohen, M. L. *J. Comput. Phys.* **1997**, *131*, 233.

(68) Johnston, J. C.; Iuliucci, R. J.; Facelli, J. C.; Fitzgerald, G.; Mueller, K. T. *J. Chem. Phys.* **2009**, *131*, 144503.

(69) Zhu, L.; Agarwal, A.; Lai, J.; Al-Kaysi, R. O.; Tham, F. S.; Ghaddar, T.; Mueller, L.; Bardeen, C. J. Solid-state photochemical and photomechanical properties of molecular crystal nanorods composed of anthracene ester derivatives. *Journal of Materials Chemistry*, 2011, *21*, 6258.

(70) Herzfeld, J.; Berger, A. E. *J. Chem. Phys.* **1980**, *73*, 6021.

(71) Antzutkin, O. N.; Lee, Y. K.; Levitt, M. H. *J. Magn. Reson.* **1998**, *135*, 144.

(72) Haeberlen, U. *High Resolution NMR in Solids: Selective Averaging, 1976*; p. 9.

(73) Leonardi, A.; Leoni, M.; Scardi, P. In *Thin Solid Films*; 2013; Vol. 530, pp. 40–43.

(74) Liu, G.; Liu, J.; Liu, Y.; Tao, X. *J. Am. Chem. Soc.* **2014**, *136*, 590.

(75) Giaimo, J. M.; Gusev, A. V.; Wasielewski, M. R. *J. Am. Chem. Soc.* **2002**, *124*, 8530.

(76) Piet, J. J.; Schuddeboom, W.; Wegewijs, B. R.; Grozema, F. C.; Warman, J. M. *J. Am. Chem. Soc.* **2001**, *123*, 5337.

(77) Meinert, C.; Hoffmann, S. V; Cassam-Chenaï, P.; Evans, A. C.; Giri, C.; Nahon, L.; Meierhenrich, U. J. *Angew. Chem. Int. Ed. Engl.* **2014**, *53*, 210.

(78) Miles, E. W.; Moriguchi, M. *J. Biol. Chem.* **1977**, *252*, 6594.

(79) Bartholmes, P.; Teuscher, B. *Eur. J. Biochem.* **1979**, *95*, 323.

(80) Remeta, D. P.; Miles, E. W.; Ginsburg, A. *Pure Appl. Chem.* **1995**, *67*, 1859.

(81) Creighton, T. E.; Yanofsky, C. *J. Biol. Chem.* **1965**, *241*, 980.

(82) Ahmed, S. A.; Ruvinov, S. B.; Kayasthas, A. M.; Miless, E. W. **1991**, *266*, 21548.

(83) DeMoss, J. *Biochim. Biophys. Acta* **1962**.

(84) Hartmann, S.; Hahn, E. *Phys. Rev.* **1962**, *128*, 2042.

(85) Baldus, M.; Petkova, A. T.; Herzfeld, J.; Griffin, R. G. *Mol. Phys.* **1998**, *95*, 1197.

(86) Barbet-Massin, E.; Pell, A. J.; Retel, J. S.; Andreas, L. B.; Jaudzems, K.; Franks, W. T.; Nieuwkoop, A. J.; Hiller, M.; Higman, V.; Guerry, P.; Bertarello, A.; Knight, M. J.; Felletti, M.; Le Marchand, T.; Kotelovica, S.; Akopjana, I.; Tars, K.; Stoppini, M.; Bellotti, V.; Bolognesi, M.; Ricagno, S.; Chou, J. J.; Griffin, R. G.; Oschkinat, H.; Lesage, A.; Emsley, L.; Herrmann, T.; Pintacuda, G. *J. Am. Chem. Soc.* **2014**.

(87) Sroka-Bartnicka, a; Olejniczak, S.; Ciesielski, W.; Nosal, a; Szymanowski, H.; Gazicki-Lipman, M.; Potrzebowski, M. J. *J. Phys. Chem. B* **2009**, *113*, 5464.

(88) Petkova, A. T.; Baldus, M.; Belenky, M.; Hong, M.; Griffin, R. G.; Herzfeld, J. *J. Magn. Reson.* **2003**, *160*, 1.

(89) Day, G. M.; Motherwell, W. D. S.; Jones, W. *Cryst. Growth Des.* **2005**, *5*, 1023.

(90) Salager, E.; Stein, R. S.; Pickard, C. J.; Elena, B.; Emsley, L. *Phys. Chem. Chem. Phys.* **2009**, *11*, 2610.

Chapter 6

Concluding Remarks

In this dissertation, the application of SSNMR techniques to biological systems has been explored. The crystal structure for the solid-to-solid photoreaction intermediate[1,2] of 9TBAE has also been determined using the combined PXRD, computational calculations and SSNMR data.

In the biological part, first a homonuclear decoupling scheme, LOW BASHD, during acquisition of C' has been introduced for uniformly-^{13}C-labeled samples. The method is generally applicable to correlation method with detection on the carbonyl, with sensitivity gain up to 1.7 and resolution improvement up to a factor of 3. Then the method has been used for confirmation of labeled cofactor PLP within the natural abundance tryptophan synthase enzyme.[3–8] The labeled sites so introduced has helped indicating potential protonation states of the tryptophan synthase at various stages of the catalytic cycle. To further progress towards the assignment tasks for the tryptophan synthase enzyme complex, correlation methods has been studied. The exploration of correlation method started with monitoring T_2' in response to varied MAS rates and decoupling power. Then at very fast MAS, a VC-CP experiment has been setup on Pf1 bacteriophage for distance measurements. Proton detection based correlation method was later setup on GB1 samples. And CP efficiencies has been monitored at different Hartman-Hahn matching conditions at 50 kHz MAS.[9–11]

SSNMR has also been applied on a 9-anthracene derivative molecule (9TBAE) for crystal structure determination. In this work, cell parameters has been predicted using

PXRD in combination with a PXRD analysis software. Then the potential structures has been optimized using CASTEP. From CASTEP, chemical shieldings have also been calculated. SSNMR HETCOR[12–14] and TOSS-t1-deTOSS[15] techniques have helped measure out experimental chemical shift and chemical shift anisotropy parameters. And these values confirmed the crystal structure for the SSRD crystal structure, which pointed to a symmetry breaking mechanism[16–18] for the 9TBAE nanorod expansion.

SSNMR has been experiencing rapid development these years. Accurate measurements at the atomic scale achievable by SSNMR have been more and more applicable and useful in many areas. Although further advances in sensitivity and resolution are still needed, SSNMR provides the versatility and capability for precise measurements in organic or biological solids. The technique has great potential for even broader applications.

References

(1) Al-Kaysi, R. O.; Müller, A. M.; Bardeen, C. J. *J. Am. Chem. Soc.* **2006**, *128*, 15938.

(2) Zhu, L.; Agarwal, A.; Lai, J.; Al-Kaysi, R. O.; Tham, F. S.; Ghaddar, T.; Mueller, L.; Bardeen, C. J. *J. Mater. Chem.* **2011**, *21*, 6258.

(3) Miles, E. W.; Moriguchi, M. *J. Biol. Chem.* **1977**, *252*, 6594.

(4) Bartholmes, P.; Teuscher, B. *Eur. J. Biochem.* **1979**, *95*, 323.

(5) Remeta, D. P.; Miles, E. W.; Ginsburg, A. *Pure Appl. Chem.* **1995**, *67*, 1859.

(6) Creighton, T. E.; Yanofsky, C. *J. Biol. Chem.* **1965**, *241*, 980.

(7) Ahmed, S. A.; Ruvinov, S. B.; Kayasthas, A. M.; Miless, E. W. **1991**, *266*, 21548.

(8) DeMoss, J. *Biochim. Biophys. Acta* **1962**.

(9) Hartmann, S.; Hahn, E. *Phys. Rev.* **1962**, *128*, 2042.

(10) Baldus, M.; Petkova, A. T.; Herzfeld, J.; Griffin, R. G. *Mol. Phys.* **1998**, *95*, 1197.

(11) Barbet-Massin, E.; Pell, A. J.; Retel, J. S.; Andreas, L. B.; Jaudzems, K.; Franks, W. T.; Nieuwkoop, A. J.; Hiller, M.; Higman, V.; Guerry, P.; Bertarello, A.; Knight, M. J.; Felletti, M.; Le Marchand, T.; Kotelovica, S.; Akopjana, I.; Tars, K.; Stoppini, M.; Bellotti, V.; Bolognesi, M.; Ricagno, S.; Chou, J. J.; Griffin, R. G.; Oschkinat, H.; Lesage, A.; Emsley, L.; Herrmann, T.; Pintacuda, G. *J. Am. Chem. Soc.* **2014**.

(12) Sroka-Bartnicka, a; Olejniczak, S.; Ciesielski, W.; Nosal, a; Szymanowski, H.; Gazicki-Lipman, M.; Potrzebowski, M. J. *J. Phys. Chem. B* **2009**, *113*, 5464.

(13) Petkova, A. T.; Baldus, M.; Belenky, M.; Hong, M.; Griffin, R. G.; Herzfeld, J. *J. Magn. Reson.* **2003**, *160*, 1.

(14) Baias, M.; Dumez, J.-N.; Svensson, P. H.; Schantz, S.; Day, G. M.; Emsley, L. *J. Am. Chem. Soc.* **2013**, *135*, 17501.

(15) Kolbert, A. C.; Griffin, R. G. Two-dimensional resolution of isotropic and anisotropic chemical shifts in magic angle spinning NMR. *Chemical Physics Letters*, 1990, *166*, 87–91.

(16) Giaimo, J. M.; Gusev, A. V.; Wasielewski, M. R. *J. Am. Chem. Soc.* **2002**, *124*, 8530.

(17) Piet, J. J.; Schuddeboom, W.; Wegewijs, B. R.; Grozema, F. C.; Warman, J. M. *J. Am. Chem. Soc.* **2001**, *123*, 5337.

(18) Meinert, C.; Hoffmann, S. V; Cassam-Chenaï, P.; Evans, A. C.; Giri, C.; Nahon, L.; Meierhenrich, U. J. *Angew. Chem. Int. Ed. Engl.* **2014**, *53*, 210.